DISSERTATION

STATE-BASED ENGINE MODELS FOR TRANSIENT APPLICATIONS WITH A SCALABLE APPROACH TO TURBOCHARGING

Submitted by

Clay S. Bell

Department of Mechanical Engineering

In partial fulfillment of the requirements

For the Degree of Doctor of Philosophy

Colorado State University

Fort Collins, Colorado

Summer 2015

Doctoral Committee:

Advisor: Tom Bradley

Daniel Zimmerle
Daniel Olsen
Peter Young

ABSTRACT

STATE-BASED ENGINE MODELS FOR TRANSIENT APPLICATIONS WITH A SCALABLE APPROACH TO TURBOCHARGING

Microgrids have the potential to improve energy surety, increase the penetration of renewable energy, and provide electrical power in remote areas; however, reduced system inertia contributes to challenges in maintaining power quality during operation. In this dissertation a state-based mean-value turbocharged diesel engine model is developed for applications in microgrid. The model is validated against transient data collected during step load testing at Colorado State University's Engines and Energy Conversion Laboratory. A controller with an air-fuel ratio based smoke limit and load based gain schedule is implemented to improve agreement with experimental data when compared to a simplified model frequently used in microgrid control studies. The state-based model is capable of variable speed operation, extending the utility to transient applications beyond micro-grid.

Due to the uncertainty around transient performance, lean burn gas engines typically are employed in steady load applications such as distributed generation or industrial systems such as natural gas compression in order to take advantage of the low cost of the fuel, improved efficiency, and reduced emissions. There is significant interest in natural gas engines for microgrids due to the low fuel cost and indications that natural gas supplies would be secure during an interruption of the national electric grid. In addition, replacing diesel engines with gas engines has been identified as a method to reduce cost and emissions associated with drilling and well stimulation. However; both of these applications involve transients which may exceed the

capabilities of lean-burn natural gas engines. In this dissertation a state based mean-value turbocharged lean-burn natural gas model is developed to study transient control strategies. Transient data was unavailable; however the model exhibits the expected characteristics during transient loading, namely limited load acceptance capability due to turbocharger lag and narrow air-fuel ratio limits.

Collecting and processing turbocharger performance data to a form appropriate for simulation is one of the more difficult and effort intensive steps when implementing state based engine models. A method is developed to implement non-dimensional performance maps thereby allowing a range of turbochargers to be modeled from the same performance data, reducing the effort required to implement models of different sizes. The non-dimensional maps seek to model the performance of compressor and turbine families in which the geometry of the rotor and housing are similar, and allow the turbocharger to be scaled for simulation in much the same way used to design customized sizes of turbochargers. A method to match the non-dimensional compressor map to engine performance targets by selecting the compressor diameter is presented, as well as a method to match the turbine to the compressor.

ACKNOWLEDGEMENTS

I would like to thank Daniel Zimmerle for providing many opportunities in various research projects during my education at Colorado State University which have expanded my expertise across several disciplines. Without his continued support throughout the past four years this would not be possible.

I would also like to thank Dr. Tom Bradley, Dr. Daniel Olsen, and Dr. Peter Young for serving on my committee. Their guidance and contributions have been instrumental in developing the models presented in this dissertation.

Finally, I would like to thank my family and friends for their never ending support and encouragement.

TABLE OF CONTENTS

LIST OF TABLES

LIST OF FIGURES

1 Introduction

1.1 Content of Dissertation

State based diesel and natural gas engine models are developed in this dissertation motivated by modeling of high horsepower applications in power generation, as well as drilling and stimulation of oil and gas wells. The dissertation is arranged into six chapters and two supporting appendices. Conclusions are drawn separately for each part. A brief description of each part follows:

Introduction: The introduction includes a review of literature and discussion of the motivation for the models presented in this dissertation.

Dynamic Turbocharged Diesel Engine Model with Experimental Validation[1]: Many engine models in micro-grid control applications are over-simplified and provide a simplified transient response. These models can provide a false sense of system integrity during design by accepting loads that a real engine may not be able to handle due to logic in the engine controller intended to protect the engine from wear or reduce emissions. In Part II a turbocharged diesel engine model is implemented that includes system states required to implement these functions. A controller model including an air-fuel ratio based smoke limit and load based gain schedule is implemented to improve agreement with experimental data when compared to a simplified model frequently used in microgrid studies. Additionally, the model is applicable to variable speed applications such as high pressure pumping, extending the utility of the model beyond

[1] The content of Part II is submitted for publication in ASME Journal of Engineering for Gas Turbines and Power, titled *Dynamic Turbocharged Diesel Engine Model with Experimental Validation*.

micro-grid applications. The full engine model is validated against transient data collected during testing at Colorado State University's Engines and Energy Conversion Laboratory.

Dynamic State Based Turbocharged Natural Gas Engine: A natural gas engine model is developed including a throttle and air fuel controller. The model consists of many of the same components utilized in the state based diesel model developed in Part II. This model is also motivated by control applications and transient response of engines employed in power generation systems, as well as drilling and stimulation of oil and gas wells. Transient data for a turbocharged natural gas engine was not available, so experimental validation could not be performed, however the model is subjected to load steps similar to those applied to the diesel engine in Part II and exhibits the expected characteristics during transient loading, namely limited load acceptance capability due to turbocharger lag and narrow air-fuel ratio limits.

Modeling of Hydraulic Fracturing using a Lean Burn Natural Gas Engine: A case study using the diesel and natural gas engine models to power a driveline in well stimulation applications is presented. The driveline component models are discussed, followed by an illustration of the assembled driveline and controls. Shifting events are simulated while pumping at low and high pressures using both the diesel and natural gas models. The results show the natural gas model is not capable of performing the shift when pumping against high pressure due to a limited ability to increase air flow beyond wide open throttle. Several methods to assist the gas engine during transients are suggested for additional studies.

Scalable Turbocharger Performance Maps for State Based Engine Models[2]: Adapting turbocharger performance maps to a form suitable for dynamic simulations is challenging for the

[2] The content of Part IV is submitted for publication in the International Journal of Engine Research, titled "Scalable Turbocharger Performance Maps for Dynamic State-Based Engine Models".

following reasons: (1) the amount of available data is typically limited, (2) data is typically not provided for the entire operating range of the compressor and turbine, (3) the performance data is non-linear. To overcome these challenges, curve fits are typically generated using the performance data individually for each device. The process however can take un-economical amounts of effort to implement for a range of compressors and turbines. Part IV introduces a method to implement non-dimensional performance maps thereby allowing a range of turbochargers to be modeled from the same performance data, reducing the effort required to implement models of different sizes. The non-dimensional maps seek to model the performance of compressor and turbine families in which the geometry of the rotor and housing are similar, and allow the turbocharger to be scaled for simulation in much the same way used to design customized sizes of turbochargers. A method to match the non-dimensional compressor map to engine performance targets by selecting the compressor diameter is presented, as well as a method to match the turbine to the selected compressor.

Summary: Conclusions from each section are collected, the major contributions of this work are summarized, and additional work is suggested.

Appendix I – Custom Simscape Component Models: The models developed in this dissertation were implemented in MATLAB Simscape. This appendix includes the description and equations for the custom component models implemented as a Simscape library.

Appendix II – Simscape Subsystems and Engine Models: Subsystems composed of several Simscape components are illustrated and discussed. The diesel and natural gas engine models including single stage and multi stage turbocharger permutations for both are assembled from the subsystems.

1.2 Literature Review

The review of literature has been divided into 4 sections:

Section 1.2.1 reviews challenges in maintaining power quality in micro-grids where the combination of high penetrations of renewable energy sources and reduced system inertia exacerbate frequency excursions encountered on the system. Several studies are reviewed which illustrate the challenges, and a simplified engine model often used in these studies is briefly reviewed.

Section 1.2.2 reviews motivation for and technical challenges associated with utilizing natural gas engines to power drilling and stimulation of oil and gas wells.

Section 1.2.3 reviews control oriented state-based diesel and spark-ignited engine models discussed in literature.

Section 1.2.4 reviews methods to implement characteristic compressor and turbine performance data in dynamic simulations. Dimensional analysis often used in compressor and turbine design is reviewed and sets the stage for a scaling approach illustrated in Part IV of this dissertation.

1.2.1 Voltage and Frequency Control in Microgrids

A microgrid is defined as "a group of interconnected loads and distributed energy resources within clearly defined electrical boundaries that act as a single controllable entity with respect to the grid. A microgrid can connect and disconnect from the grid to enable it to operate in both grid-connected and island-mode [1]." Recent research in microgrids has been motivated by energy security and surety [1] [2] [3] [4], increased efficiency [1] [2] [5] [6], sustainability through increased penetration of renewable energy [2] [5] [6] [7] [8], and remote energy systems [3] [7] [9].

The reduced system inertia of microgrids, due to the increased penetration of renewable energy and distributed generation, makes control of voltage and frequency more challenging by contributing to power disturbances such as voltage sags and swells, and harmonics [8], and can lead to cascading outages [10]. In conventional power generation strong coupling between the rotational speed and the electrical frequency allow synchronous machines to contribute to the inertia of the power system. In many renewable sources such as wind turbines and photovoltaic units the motion of the generator is electrically decoupled from the grid frequency by a converter, and therefore these systems do not contribute to the system inertia [2] [11].

Several papers investigate frequency control in grids with reduced inertia. Wall et al [10] present a method for determining the generator inertia available during a frequency event, useful as additional input in automatic protection systems. Tielens [12] investigated the rate of change of frequency and the amplitude of frequency excursions in an electrical system with increasing renewable penetrations. They report a higher rate of change of frequency during a disruption due to the reduced system inertia, and amplified maximum and minimum frequency excursions since the synchronous generators in the system have even less time to react due to the low system inertia. Four frequency support methods from literature are also summarized in the paper. They are: 1) a coordinated control of an energy storage system, 2) deloading or curtailing the renewable source so a reserve is created, 3) the use of kinetic energy of a wind turbine to provide frequency support, and 4) demand side management.

Maintaining power quality during separation from the utility grid and operation in islanding mode has also been the focus of several studies. Serban et al [7] discussed balance of power supplied and consumed on an isolated low-power micro-grid with renewable energy sources utilizing a 3-phase dump load for frequency control and unbalanced currents. Green et al [4]

demonstrated island mode operation of an inverter based micro-grid in a control scheme designed to accommodate parallel operation. Katiraei et al [13] investigated the control to ensure stability of a micro-grid even during islanding events utilizing two distributed generation units, one of which is interfaced through a power electronic converter with independent real and reactive power control. Del Carpio-Huayllas et al [14] discussed intentional and unintentional islanding of a micro-grid. In a presentation by Dilliott [15] a timeline of events from the September 8th, 2011 San Diego black out illustrates the UCSD campus micro-grid took nearly seven hours to recover and bring the campus back online after an unplanned separation from the utility grid, mainly due to frequency issues. The presentation illustrated it is critical to understand the likely frequency and voltage transients that will occur during exceptional operating conditions such as an unplanned islanding.

Liu et al [16] identify "Most of the remote and isolated communities or technical installations (communication relays, meteorological systems, tourist facilities, farms, etc.) which are not connected to national electric distribution grids rely on diesel engines to generate electricity". Wind diesel hybrid systems are discussed by Ibrahim et al [17] and Sebastian [6] [5].

In the paper by Ibrahim [17] electricity supply in remote areas serviced by diesel generators are discussed. The exploration of wind diesel hybrid systems is presented as a method to reduce diesel fuel consumption. The paper explores incorporating compressed air energy storage into high-penetration wind-diesel systems to improve the use of renewables and reduce the cost of electricity through reduced diesel consumption. Numerical models of each component, including a mean-value diesel model which enables evaluation of the fuel economy, are proposed and used to model a case study based in northern Quebec. The operation and fuel consumption of the diesel generators during standby operation (times when the engine is idling so that it can

respond to a wind speed reduction) is identified as a gross detriment to the economic and environmental benefits of a wind diesel hybrid system since the engines may consume as much a s 50% of the fuel consumed at nominal power. As this study was focused on optimization for reduced fuel consumption, dynamic response of the engine is not illustrated.

Sebastian [6] presents component models and a combined wind-diesel hybrid isolated power system with a battery energy storage system. Sebastian also presents a wind-diesel hybrid system in wind only mode [5]. Frequency and voltage control is presented during wind only operation and during transition from wind only to wind-diesel mode. The engine can be engaged or dis-engaged from the synchronous machine via a clutch. The diesel engine model used by [6] is simplified as a series of transfer functions and is employed in other studies [18]. This simplified engine model is adapted from the governor model presented in a paper by Hannet [19]. This type of model simplifies system dynamics and does not model advanced control functions common in modern engines which may affect the system response, such as gain schedules and air fuel ratio limits.

Additionally, a private report for the Marine Corps Air Station Miramar Micro-grid prepared by the National Renewable Energy Laboratory [20] determined that Natural Gas engines were of interest to military micro-grid applications, and that there is a need for better simulation models to represent the transient performance of engines in the size range of 100s-1000s kW. A public report of this effort [21] identifies the base's reliance on natural gas as a major energy source and the interest in 3MW of landfill gas generation. MIT Lincoln Laboratory's report [2] also stated the NG system is largely independent of the electrical system, so μGrids operating on NG engines could still be considered "secure," in the event the electrical system failed. Prior work has not considered natural gas engines for micro-grid applications.

1.2.2 Dedicated Natural Gas Engines in Drilling Operations and Well Stimulation

Historically diesel has been the fuel of choice for equipment used during drilling and stimulation of oil and gas wells due to the relatively low cost and high accessibility of the fuel, and the proven capability of diesel engines during transient loading conditions [22]. Rising prices in diesel fuel have contributed to significant increases in costs for drilling and well service companies [23]. Aside from cost reduction, additional reasons motivating the use of natural gas in well services include the availability of gas from nearby wells in production, reduction of traffic to the well pad, maintenance benefits, efficiency gains and emissions reductions [22] [23].

Natural gas has been increasing in popularity as a fuel for commercial heating, industrial processes, and power generation due to its low cost, low emissions levels, and highly reliable supply system. Supplementing diesel with natural gas in dual-fuel engines has been demonstrated as a means to reduce the costs of oil and gas operations [22] [23]. The use of dedicated natural gas engines to power drilling and stimulation has also recently been demonstrated however is not widely implemented due in part to the uncertainty in the performance of natural gas engines during transient loading [22].

The air fuel ratio of lean-burn natural gas engines is controlled within a narrow range. Excess air is used to reduce the peak cylinder temperature as a method to reduce emissions of oxides of nitrogen [24] [25]. Reduced peak cylinder temperature also contributes to efficiency improvement by reducing thermal losses [25] [26]. If the air-fuel mixture is too lean misfire or flame quenching can occur leading to increased emissions of unburned hydrocarbons [27]. In order to avoid a significant reduction in power density resulting from operating on a lean air-fuel mixture the engines are typically turbocharged. The narrow range of air-fuel ratio limits the ability of the gas engine to rapidly change power output since the air flow must be increased in

order to increase fueling. Quickly adjusting the throttle allows the engine to accept relatively small changes in load; however, the lag in the acceleration of the turbocharger limits the engines ability to accept larger changes in load. For this reason, lean-burn natural gas engines are typically employed in applications with a relatively steady load level such as support of power generation during peak loads and industrial processes.

1.2.3 State-Based Mean Value Engine Modeling

Engine models are frequently developed to balance the tradeoff between model fidelity and computational expense [28]. Depending on the utility of the model a different approach may be employed. State-based mean value engine models are frequently employed in control applications where knowledge of engine subsystems plays an important role in the control design, but sub-crank angle resolution is not required [29] [30] [31]. State-based models utilize numerical solutions of first order differential equations to model thermodynamic states throughout the intake and exhaust systems, while algebraic relationships are used to model the flow of mass and heat between neighboring states [30]. Combustion in individual cylinders and valve effects typically are not included in the models. Instead, mean value models average flowrates over several engine cycles [28] [30]. Rather than include detailed combustion models, many mean-value models rely on large amounts of empirical data such as exhaust temperature and thermal efficiency maps [29] [30] [31]. The strengths of the mean value model are simplicity and lean computation, while the weaknesses are its reliance upon large amounts of engine empirical test data, low bandwidth, and being engine-specific to some degree [30].

Components of mean value models developed for turbocharged diesel engines are presented in [17] [28] [30] [31]. Many of these models are developed to aid in the design of engine controllers and equipment including hardware-in-the-loop and on-board diagnostic applications

which generally require more detail than necessary to simulate the first order inertial dynamics. The main components in these models are (1) the air filter, (2) turbocharger compressor, (3) intercooler, (4) intake manifold, (5) combustion, (6) exhaust manifold, (7) turbocharger turbine, (8) turbocharger rotor, and (9) crankshaft dynamics. Additional components for spark ignited engines are presented in [28]. Several approaches to each component are illustrated in the literature depending on the data available and/or the utility of the model.

1.2.4 Dynamic Turbocharger Modeling

Since fueling is restricted by air-fuel ratio limits, the power an engine can produce is generally limited by the amount of air flow into the cylinders. Since the volumetric flow rate into the cylinders is limited by the engine geometry, mass flow can be increased by increasing the density in the intake manifold. Turbochargers use a rotary compressor installed in the intake system and driven by a turbine installed in the exhaust stream to increase the density of air in the intake manifold.

Accurately modeling turbocharging is a key part of implementing a state-based engine model. Compressor and turbine performance is typically implemented as curve fits [17] [31] [32] or lookup tables [29] [33] developed from steady state performance data provided by the manufacturer. Although lookup tables are computationally efficient and readily implemented in simulations, curve fits are generally used because provided data (1) typically does not cover the entire operating region of the compressor or turbine but rather illustrates only the high efficiency region at high pressure ratios and rotor speeds, and (2) is limited to a few points which are characteristically non-linear, incurring additional error when used with interpolation techniques in a data table [32]. Using curve fits, the data can be extrapolated into the low pressure ratio and low rotor speed regions while avoiding error induced by interpolation techniques. Curve fitting

the performance data, however requires significant amount of effort and judgement to determine a suitable fit. Several methods to fit compressor and turbine data are summarized and illustrated by [32]. In order to model a series of engines equipped with different size turbochargers, the process must be repeated for each compressor and turbine.

A dimensional analysis performed by [34] illustrates the performance characteristics of compressor and turbines are typically provided by manufacturers in terms of corrected mass flow, M_{Corr}, and corrected rotor speed, N_{Corr}, which are defines as:

$$M_{Corr} = \frac{\dot{m}\sqrt{T_u}}{P_u} \tag{1}$$

$$N_{Corr} = \frac{N}{\sqrt{T_u}} \tag{2}$$

These parameters, however, are related to a dimensionless mass-flow parameter, φ, and a rotor tip Mach number based on the speed of sound at the entry, c_0, defined as:

$$\varphi = \frac{\sqrt{R}}{D^2}\left(\frac{\dot{m}\sqrt{T_u}}{P_u}\right) \tag{3}$$

$$c_0 = \frac{D}{\sqrt{\gamma R}}\left(\frac{N}{\sqrt{T_u}}\right) \tag{4}$$

Manufacturers illustrate maps using corrected mass flow, M_{Corr}, and corrected rotor speed, N_{Corr},since they are produced for a device with a selected diameter, D, and the device will always handle the same gas, $R = R_{air}, \gamma = \gamma_{air}$.

$$M_{Corr} = f(\frac{P_u}{P_d}, N_{Corr}) \tag{5}$$

$$\eta = f(\frac{P_u}{P_d}, N_{Corr}) \tag{6}$$

Instead, if the diameter of the device is known, these maps can be implemented in terms of the dimensionless mass-flow parameter, φ, and a rotor tip Mach number based on the speed of sound at the entry, c_0, to represent a family of geometrically similar compressors or turbines where the pitch-chord ratio, s/l, and the aspect ratio, h/l, remain constant within the family.

$$\varphi = f(\frac{P_u}{P_d}, C_0) \tag{7}$$

$$\eta = f(\frac{P_u}{P_d}, C_0) \tag{8}$$

1.3 Summary of Motivation and Modeling Goals

Due to the reduced system inertia associated with a microgrid, maintaining power quality is more challenging than in traditional power systems and has been the focus of many recent studies. Diesel engine models utilized in many microgrid control studies simplify system dynamics and do not model advanced control functions common in modern engines. The goals of the first study, Part II of this dissertation, are (1) to illustrate the limitations of the simplified diesel model, and (2) to develop and validate an improved diesel engine model which includes engine subsystems that may affect the transient response in order to enable the inclusion of modern engine controls in these studies. State-based mean value engine models are frequently employed in control applications where performance of engine subsystems plays an important role in the control design, and are well suited to this application.

Due to the limited ability of lean-burn natural gas engines to handle variable loads, the engines are typically only employed in steady applications. Many prior microgrid studies have not considered natural gas engines for this reason, although there is interest driven by the low cost,

low emissions levels, and high efficiency of lean-burn gas engines, as well as national security interests. Additionally, recent interest in employing natural gas engines for drilling and stimulation of oil and gas wells requires a transient engine model for control design studies. A state-based mean-value natural gas engine model would consist of many of the same subsystems as the state-based diesel engine model, and could be implemented with relatively little additional effort. The goal of Part III of this dissertation is to implement a lean-burn natural gas engine model for simulation in transient applications.

Turbocharging plays an important role in both diesel and natural gas engines, and must be included in state-based models to accurately simulate the overall system dynamics. To acquire data specific to a particular turbocharger, and process that data into lookup tables or curve fits well suited to simulation models requires significant effort and judgement, and is perhaps one of the more difficult tasks when implementing a state-based engine model. The goal of Part IV of this dissertation is to improve the workflow by using a scalable approach, similar to that used in compressor and turbine design, in order to allow a family of equipment to be modeled from data for a single device. The non-dimensional performance data can then easily be scaled to match a particular engine displacement and power.

2 Dynamic Turbocharged Diesel Engine Model with Experimental Validation

Voltage and frequency control for micro-grid and distributed energy systems has received recent attention in research, where reduced inertia of the electrical system results in challenges maintaining power quality during transient events induced by rapid change in renewable energy production or load [5] [6] [7] [10] [13]. Steady state engine models validated for fuel economy prediction exist and are utilized for simulations targeting minimized fuel consumption or maximized islanding time of wind diesel hybrid systems [9] [17]. An engine model validated against experimental data collected during a transient event such as a significant load step is difficult to find in the literature. In dynamic auxiliary power supply models, the engine is frequently modeled as a torque source driven by transfer functions representing the control system, actuator response and an ignition delay [18] [19]. This type of model simplifies system dynamics and does not model advanced control functions common in modern engines such as gain schedules and air fuel ratio limits. This chapter illustrates the limitations of simplified dynamic engine models, describes a state-based diesel engine model with multistage turbocharging and advanced control functions, and compares performance of the state-based model with the simplified model and experimental data during transient loading.

This study compares two engine models, the simplified model shown in Figure 2-1, and a state based engine model shown in Figure 2-5. The simplified model consists of transfer functions which model the response of a droop governor controller and actuator, and a fixed time delay to model the combustion and torque production of the engine. This model is commonly used in power system studies [6] [18] [19] and other transient studies. The state based model was developed at CSU to investigate dynamics during load acceptance of diesel generators in power

systems, and shifting events in high horsepower drivelines such as those used in hydraulic fracturing.

To ground the modeling work, transient response experiments were performed using equipment at CSU's Powerhouse engine test facility on a Cummins QSK50 diesel engine descried in Table 2-1. The engine was instrumented to measure engine speed, brake torque, gas temperatures and pressures throughout the intake and exhaust systems, air mass flow rate, fuel mass flow rate, and turbocharger rotor speeds. To perform the tests additional torque was applied at a selected ramp rate from a base load to a final load while the commanded engine speed was fixed as described in Table 2-2. The ramp rates were selected using caution to avoid engine shutdowns and potential damage.

The remainder of this Part is structured in 3 sections. Section 2.1 - Limitations of Ideal Torque Response Models describes a simplified engine model commonly utilized for simulation studies in power systems and industrial applications, and compares that engine model to the experimental data. Section 2.2 - State Based Diesel Model describes the advanced state based model and controller. Section 2.3 - State Based Model Validation and Results compares the state based model against the experimental data and response of the simplified model.

Table 2-1: Test engine description

Make	Cummins
Model	QSK50 Diesel
Emissions Certification	Tier 2
Displacement	50 L
Number of Cylinders	16
Turbocharging	Two-Stage Aftercooled
Rated Power	2500 hp @ 1900 rpm
Peak Torque	7081 lb-ft @ 1500 rpm

Table 2-2: Description of transient experimental test points

Point #	Ramp Rate (lb-ft/sec)	Initial – Final Torque (lb-ft)
1	294	700 - 3700
2	500	700 – 3700
3	833	700 – 3700
4	833	700 - 2200
5	833	2200-3700
6	833	3700-5200
…		

2.1 Limitations of Ideal Torque Response Models

In the simplest form, a dynamic engine model is a torque source acting on a rotating inertial mass. The torque level produced by the engine is controlled by feedback from the rotational speed of the inertia. One such engine model employed frequently in dynamic power system studies is shown in Figure 2-1. Transfer functions are used to model the response of the control system and actuator before providing a torque or power output to the inertia. This model has three significant limitations in transient applications:

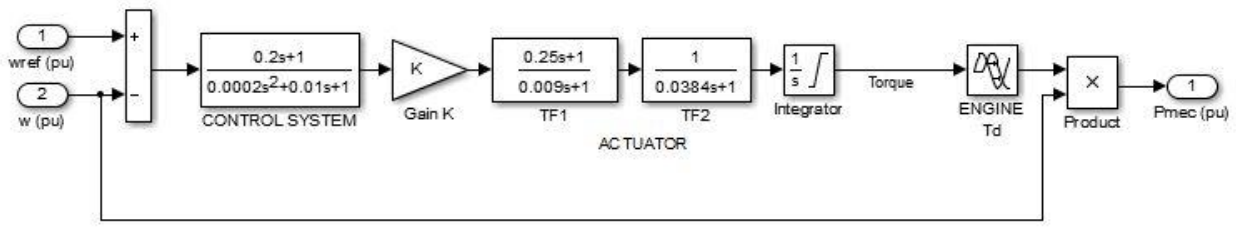

Figure 2-1: Simplified dynamic engine model from SimPower

1) The model is idealized for small steps where the engine can accept the load without encountering controller limits which protect the engine from wear and/or reduce emissions. Internal engine states, which may limit torque production under certain conditions, are not modeled. This limits the model to applications in which the variations in load are small relative to engine power. This point is discussed further including reference to experimental data in subsection 2.1.1.

2) Experimental data shows a different response at low load levels than higher loads. The simplified model does not vary transfer function time constants to account for different response characteristics at low load. This point is discussed further including reference to experimental data in subsection 2.1.2.

3) The maximum torque limit appearing as the upper saturation limit of the integrator in the model is not a function of engine speed. Instead, the model can produce the rated torque at any engine speed. This limits the model to fixed speed applications where deviations from the fixed speed are small. Several scenarios exist where the primary interest is load acceptance during a transient that includes variable speed operation. Shifting gears in a transmission powering a high pressure pump or in a heavy duty vehicle is an example. As the new gear is engaged in these applications the torque production and commanded engine speed are adjusted simultaneously, requiring the engine to produce similar brake power at a new combination of speed and torque.

Although variable speed operation is not critical to micro-grid models, implementing a model capable of variable speed operation will extend the utility of the model to include these applications.

2.1.1 Controller Smoke Limit

Modern engines incorporate feedback from engine performance to engage alternate control paths at times. One such example is a smoke limit in which the controller limits fuel addition when the air-fuel mixture exceeds a rich limit. This saturation of fuel rate limits the torque production until the turbocharger rotor accelerates to provide sufficient combustion air. This limit was encountered during transient response testing at Colorado State University when a torque ramp was applied by the dynamometer from 700 ft-lb to 3700 ft-lb (10% - 53% maximum torque) using ramp rates of 294, 500, and 833 ft-lb/sec (4.2%/sec, 7.1%/sec, and 12%/sec).

At the lowest ramp rate the smoke limit was not encountered. Figure 2-2 shows the applied torque and measured engine speed during the transient. The maximum speed excursion measured during the test was 2.7% from the commanded speed. The response of the simplified engine model to the same torque ramp is overlaid in the figure and agrees well with the experimental data experiencing a 1.6% speed excursion.

When the ramp rate was increased to 7.1%/sec the smoke limit was encountered as shown in Figure 2-3. It is important to note this is a rare case in which the turbocharger is able to spool up and the engine is able to recover after encountering the smoke limit without requiring the load to be reduced. The maximum speed excursion measured during the test was 13.1%. The figure shows the simulated response no longer captures the actual engine response when the smoke limit is encountered, experiencing a maximum excursion of only 2.6%.

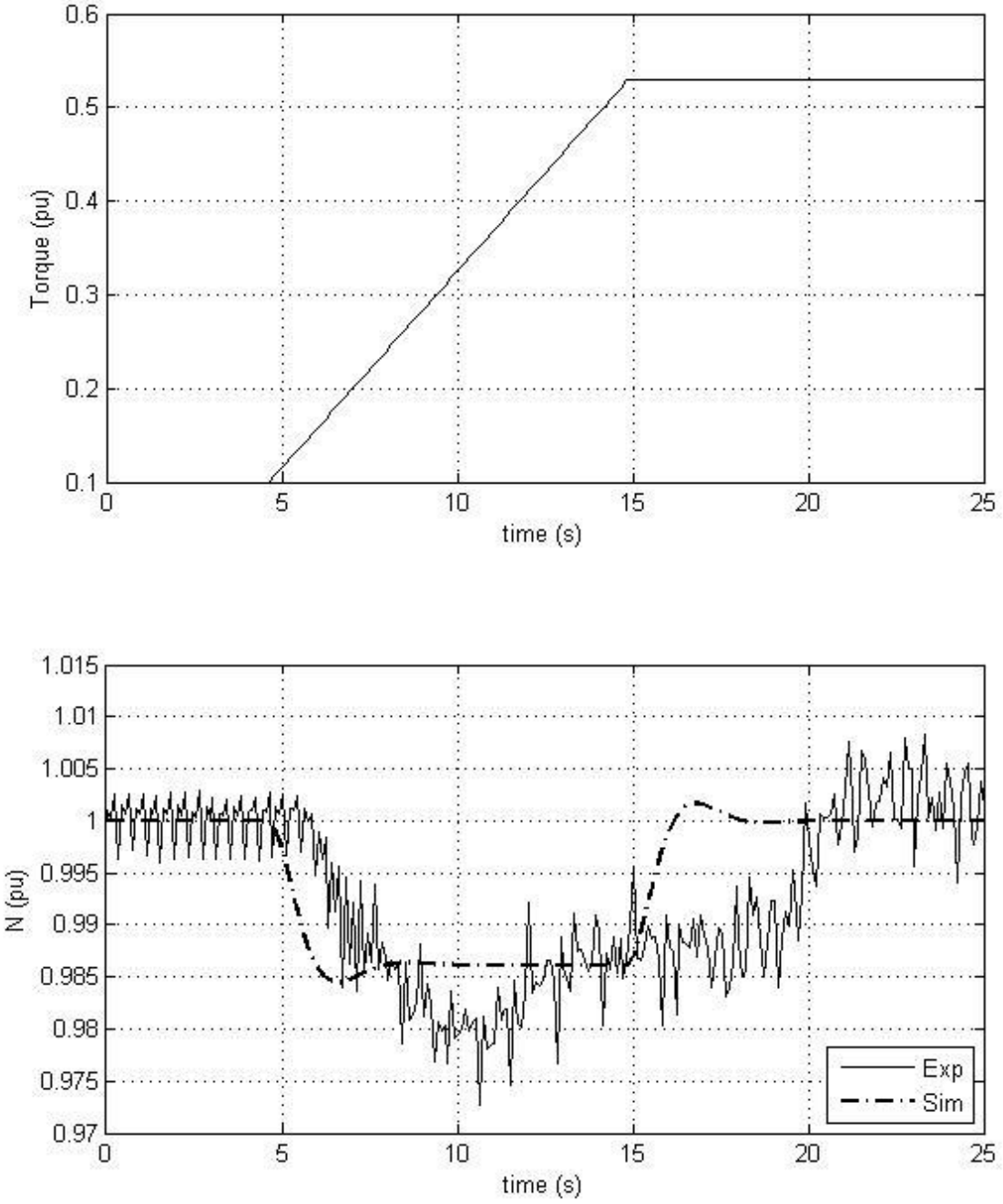

Figure 2-2: Experimental and simulated response to a 43% torque ramp applied from 10% to 53% of maximum torque at a rate of 4.2%/sec.

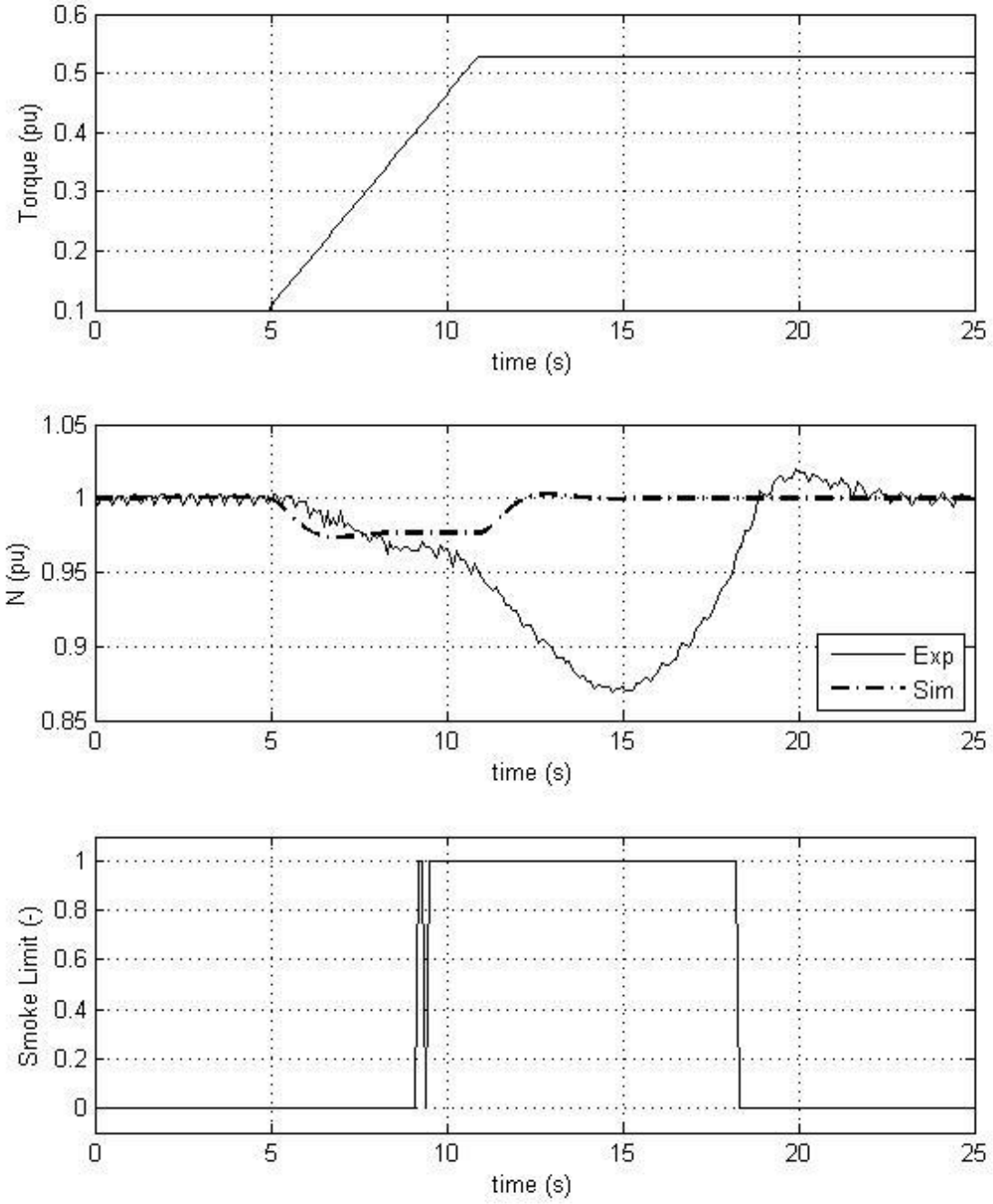

Figure 2-3: Experimental and simulated response to a 43% torque ramp applied from 10% to 53% of maximum torque at a rate of 7.1%/sec; A rare case in which the smoke limit is encountered and the experimental engine is able to recover after a large deviation from the commanded speed.

When the ramp rate was increased to 12%/sec the smoke limit was encountered and resulted in a complete engine shutdown. Unfortunately experimental data during this event is unavailable because it occurred while debugging data acquisition equipment during preliminary testing and was not repeated to avoid potential damage to equipment.

2.1.2 Variation in Response at Different Load Levels

To explore engine response at different load levels a torque ramp was applied starting at different initial loads. Each ramp corresponds to approximately 20% of the available torque at the commanded speed. Since the ramps are smaller in magnitude during this portion of testing, a ramp rate of 833 ft-lb/sec (12%/sec) was used without encountering the smoke limit. Figure 2-4 shows the applied torque ramps, the response of the experimental engine, and the simulation results using the simplified model.

Table 2-3 summarizes the maximum speed deviation and recovery time measured during the experimental testing and simulation. The recovery time was taken as the time after the start of the ramp at which the engine speed recovered to 99% of the commanded speed. The simulation and experimental results are in good agreement during the steps performed at medium and high loads, however the response of the experimental engine is much slower than the simulated response during the step at low load.

Table 2-3: Speed deviation and recovery time of experimental test and simplified model during 20% torque ramp performed at dIfferent load levels

	Experiment		Simplified Model	
Initial - Final Load	Speed Deviation	Recovery Time	Speed Deviation	Recovery Time
10% – 31%	5.5%	6.75 sec	3.3%	3.85 sec
31% – 53%	3.6%	4.58 sec	3.1%	3.62 sec
53% - 74%	2.9%	4.54 sec	3.9%	3.53 sec

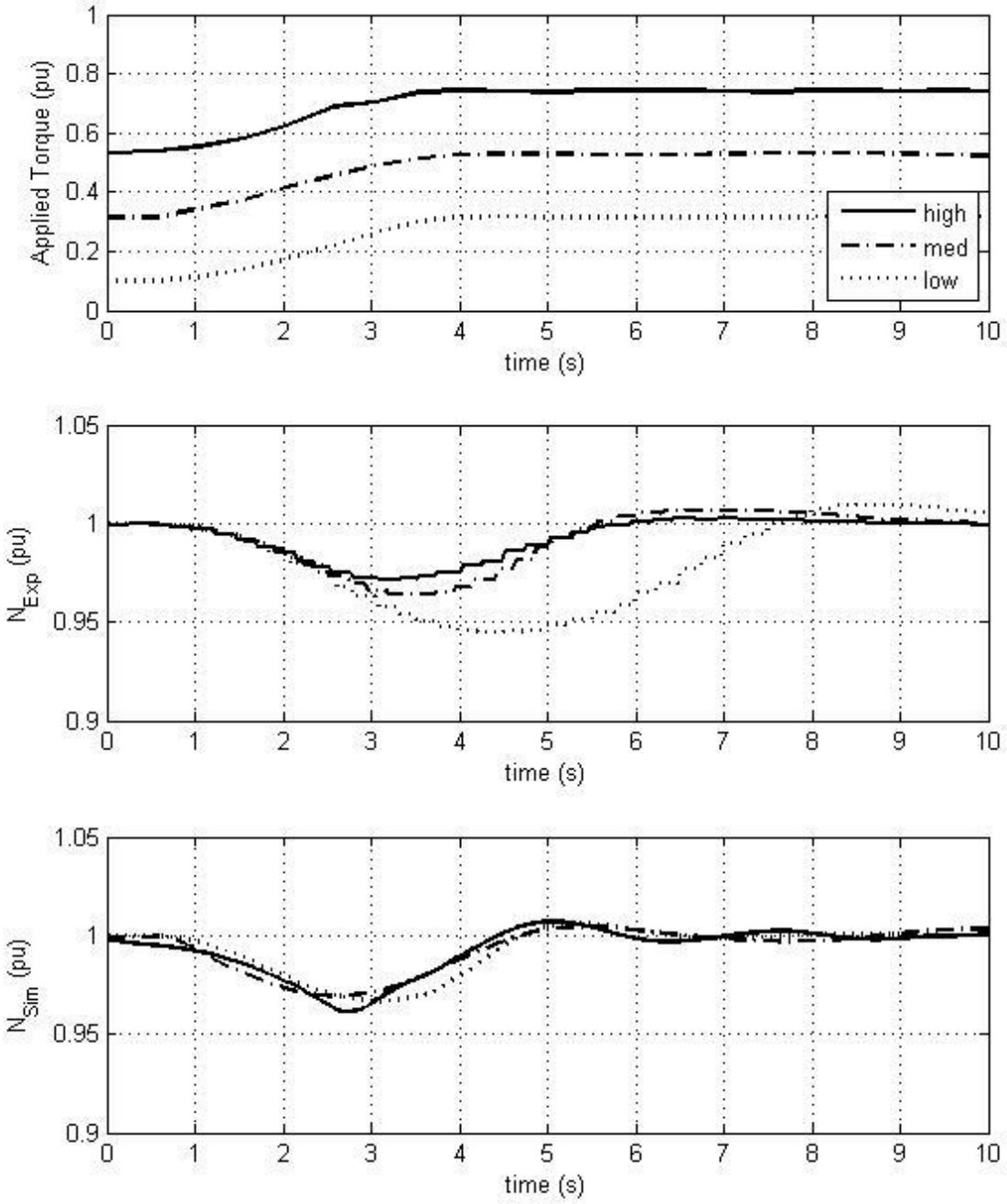

Figure 2-4: Experimental and simulated engine speed during a 20% torque ramp performed at different load levels

2.2 State Based Diesel Model

The state based model follows the mean torque production approach [30] [31] with the addition of multi-stage turbocharging, and simplification of the intercooler, combustion and exhaust manifold models. Pulsation due to combustion in individual cylinders is not resolved by the model; instead it represents pressures, temperatures and flowrates averaged over an entire engine cycle. The completed mean value model consists of several non-linear algebraic relations based on empirical data and first order differential equations representing state equations for manifolds. The main components included in the model are shown in Figure 2-5. The submodels for these components are described in detail in the following sections. Four gas states defined by temperature and pressure are associated with the compressor interstage, intake manifold, exhaust manifold, and turbine interstage. Three rotational states are included in the model associated with the turbocharger rotors and the engine crankshaft. A PID based governor model incorporating a max fueling curve, air-fuel based smoke limit and gain scheduling is included to control the fueling input.

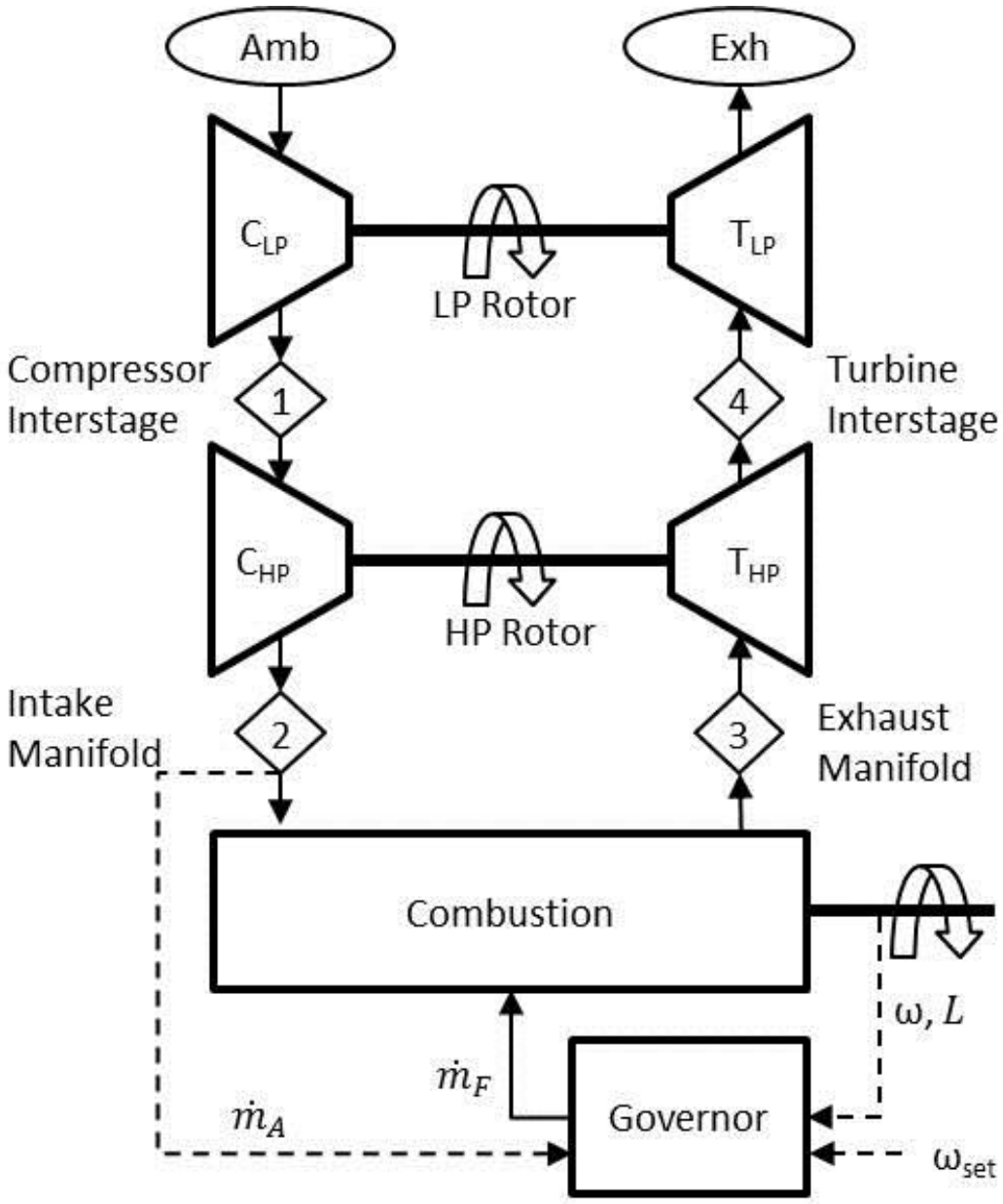

Figure 2-5: Two stage turbocharged diesel engine model schematic

2.2.1 Compressor

A scalable approach to compressor performance is implemented as discussed in detail in Part IV. The rotor speed, ω_{TC}, compressor diameter, D_C, pressure ratio across the compressor, $\left(\frac{P_d}{P_u}\right)_{actual}$, compressor inlet temperature, T_u, and the gas properties, γ & R, are used to calculate the pressure index, P_{idx}, and rotor tip Mach number, $c_{0,C}$.

$$P_{idx} = \frac{\left(\frac{P_d}{P_u}\right)_{actual} - 1}{\left(\frac{P_d}{P_u}\right)_{surge} - 1} \tag{9}$$

$$c_{0,C} = \frac{\omega_{TC} D_c}{\sqrt{\gamma R T_u}} \tag{10}$$

Lookup tables are then used to evaluate the non-dimensional compressor mass flow coefficient $\emptyset_C = f\left(P_{idx}\,, c_{0,C}\right)$ and compressor isentropic efficiency, $\eta_C = f(P_{idx}\,,\, c_{0,C})$. The mass flow rate through the compressor, $\dot{m}_C$, is calculated from the non-dimensional compressor mass flow coefficient.

$$\dot{m}_C = \frac{P_u \emptyset_C D_c^2}{\sqrt{R T_u}} \tag{11}$$

The temperature of the gas leaving the compressor outlet, $T_{C,out}$, and the torque required to drive the compressor, τ_C, are calculated from isentropic efficiency relations as in [30].

$$T_{C,out} = T_u \left\{ 1 + \frac{1}{\eta_C} \left\{ \left(\frac{P_d}{P_u}\right)^{\frac{\gamma-1}{\gamma}} - 1 \right\} \right\} \tag{12}$$

$$\tau_C = \frac{\dot{m}_c C_p T_u}{\eta_c \omega_{TC}} \left(\left(\frac{P_d}{P_u}\right)^{\frac{\gamma-1}{\gamma}} - 1 \right) \tag{13}$$

2.2.2 Turbine

The turbine is modeled similar to the compressor using the scalable non-dimensional approach in Part IV. The rotor tip Mach number, $c_{0,T} = \frac{\omega_{TC} D_T}{\sqrt{\gamma R T_u}}$, is calculated and used with the expansion ratio across the turbine, $\frac{P_u}{P_d}$, to evaluate the non-dimensional turbine mass flow coefficient,

$\emptyset_T = f\left(\frac{P_u}{P_d}, c_{0,T}\right)$, and efficiency, $\eta_T = f(\frac{P_u}{P_d}, c_{0,T})$. Mass flow through the turbine is calculated from the non-dimensional mass flow coefficient.

$$\dot{m}_T = \frac{P_u \emptyset_T D_T^2}{\sqrt{RT_u}} \tag{14}$$

The torque applied to the turbocharger rotor, τ_T, and the temperature of the gas leaving the turbine, $T_{T,out}$, are calculated using isentropic relations.

$$\tau_T = \frac{\eta_T \dot{m}_T C_p T_u}{\omega_{TC}} \left(1 - \left(\frac{P_d}{P_u}\right)^{\frac{\gamma-1}{\gamma}}\right) \tag{15}$$

$$T_{T,out} = T_u \left(1 + \eta_T \left(\left(\frac{P_d}{P_u}\right)^{\frac{\gamma-1}{\gamma}} - 1\right)\right) \tag{16}$$

2.2.3 Turbocharger Rotor

The acceleration of the rotor is computed from a torque balance between the compressor and turbine neglecting bearing friction.

$$\frac{d\omega_{TC}}{dt} = \frac{\tau_T - \tau_C}{J_{TC}} \tag{17}$$

The rotor speed is then computed by numerical integration from the initial condition.

2.2.4 Adiabatic Plenums

The plenums between compressor stages and turbine stages, as well as the exhaust manifold are modeled as adiabatic constant volume chambers. Inlet and outlet energy flows are modeled as $\dot{Q}_{in} = \dot{m}_{in} C_p T_{in}$ and $\dot{Q}_{out} = \dot{m}_{out} C_p T_i$.

Two first order differential equations can be derived from the ideal gas equation.

$$(\dot{m}_{in} - \dot{m}_{out}) = \frac{V_i}{RT_i} * \left[\left(\frac{dP_i}{dt}\right) - \frac{P_i}{T_i}\left(\frac{dT_i}{dt}\right)\right] \quad (18)$$

$$\left(\dot{Q}_{in} - \dot{Q}_{out}\right) = \frac{V_i C_v}{R}\left(\frac{dP_i}{dt}\right) \quad (19)$$

The temperature and pressure of the plenums are then solved for by numerical integration of (18) and (19) from an initial condition. Table 2-4 lists the values which $\dot{m}_{in}$, $\dot{m}_{out}$, T_{in}, T_i, P_i and V_i take for each adiabatic plenum.

Table 2-4: Definition of terms in each adiabatic plenum

Plenum	$\dot{m}_{in}$	$\dot{m}_{out}$	T_{in}	T_i	P_i	V_i
Compressor Interstage	$\dot{m}_{C,LP}$	$\dot{m}_{C,HP}$	$T_{C,out,LP}$	T_1	P_1	V_1
Exhaust Manifold	$\dot{m}_{exh}$	$\dot{m}_{T,HP}$	T_{exh}	T_3	P_3	V_3
Turbine Interstage	$\dot{m}_{T,HP}$	$\dot{m}_{T,LP}$	$T_{T,out,HP}$	T_4	P_4	V_4

2.2.5 Intercooler/Intake Manifold

On many stationary engines the intercooler is oversized and remarkably effective at maintaining a set point temperature with only minor fluctuations even during a transient event. Therefore the intercooler and intake manifold are modeled as a single volume similar to the adiabatic plenum, however heat is removed to maintain a constant temperature. This assumption also neglects pressure drop across the intercooler which was seen to be relatively small in experimental data.

$$\left(\frac{dP_2}{dt}\right) = \frac{\left(\dot{m}_{c,HP} - \dot{m}_a\right)RT_2}{V_2} \quad (20)$$

2.2.6 Combustion and Torque Production

Engine load, *L*, is calculated as the brake torque normalized by the maximum torque available at the current engine speed, and is used as an index for the volumetric efficiency, indicated thermal efficiency and exhaust temperature maps.

$$\tau_{Max} = f(N) \tag{21}$$

$$L = \frac{\tau_B}{\tau_{Max}} \tag{22}$$

Empirical lookup tables indexed by speed and load are generated from steady state data and implemented for volumetric efficiency, $\eta_v = f(N, L)$, indicated thermal efficiency, $\eta_{Th} = f(N, L)$, and exhaust temperature, $T_{exh} = f(N, L)$.

Air mass flow rate into the combustor, $\dot{m}_a$, is calculated using the "speed-density" equation.

$$\dot{m}_a = \frac{\eta_v \rho_2 V_d N}{120} \tag{23}$$

$$\rho_2 = \frac{P_2}{RT_2} \tag{24}$$

The mass flow rate of exhaust gas, $\dot{m}_{exh}$, is calculated by mass conservation of intake air and fuel.

$$\dot{m}_{exh} = \dot{m}_a + \dot{m}_f \tag{25}$$

The thermal efficiency, engine speed, fuel mass flow rate and lower heating value are used to calculate the indicated torque produced.

$$\tau_S = \frac{\eta_{Th} \dot{m}_f LHV}{\omega} \tag{26}$$

A linear approximation of friction torque internal to the engine is included [35]. The brake torque applied to the crankshaft is calculated as the difference of the indicated torque and the friction torque.

$$\tau_B = \tau_S - \tau_F \tag{27}$$

The acceleration of the crankshaft is calculated based on a torque balance between the brake torque generated by the engine and the retarding torque applied by the load.

$$\frac{d\omega}{dt} = \frac{\tau_B - \tau_{load}}{J} \tag{28}$$

The shaft speed is then computed by numerical integration from the initial condition.

2.2.7 Governor with Smoke Limit and Gain Schedule

The governor implemented in the model includes a smoke limit, maximum fueling curve and gain schedule as shown in Figure 2-6. An upper limit on fueling based on the measured air mass flow rate and minimum air-fuel ratio is calculated as $\dot{m}_{f,smoke} = \frac{\dot{m}_a}{R_{min}}$. A maximum fueling table is used to determine the maximum fuel rate as a function of engine speed, $\dot{m}_{f,\tau\,max} = f(\omega)$. The minimum of $\dot{m}_{f,smoke}$ and $\dot{m}_{f,\tau\,max}$ is passed to the PID controller as an upper saturation limit on the controller output, $\dot{m}_{f,max} = \min(\dot{m}_{f,smoke}, \dot{m}_{f,\tau\,max})$. The PID controller includes a clamping anti-windup method. The proportional and integral gains are selected from the gain schedule as a function of load, $[G_P, G_I] = f(L)$, and passed to the PID control. The PID acts on the error in engine speed, $\omega_e = \omega - \omega_{set}$, and outputs fuel mass flow rate.

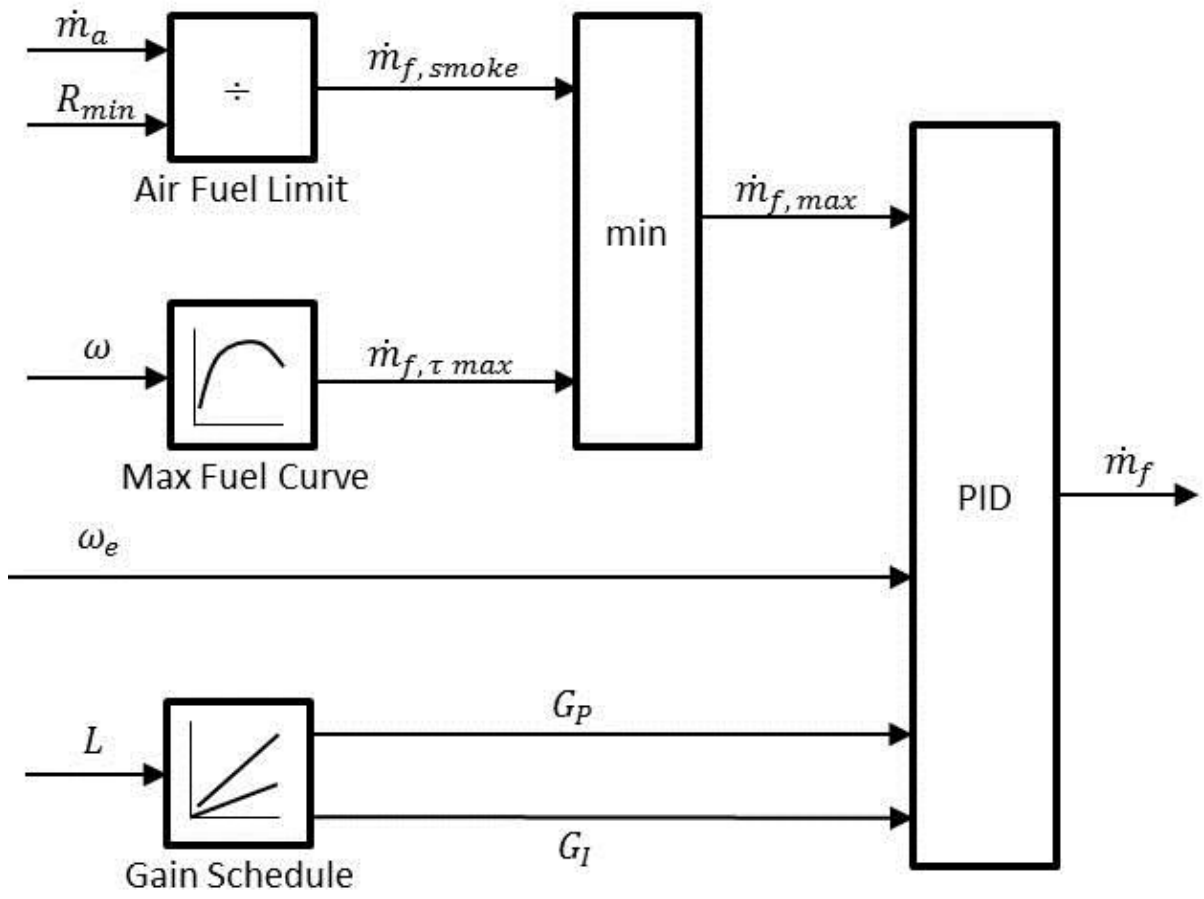

Figure 2-6: Governor schematic including air-fuel ratio limit, max fueling curve and gain schedule

2.3 State Based Model Validation and Results

Performance and geometry parameters for the state based model were generated using steady state data from the test engine. Steady state validation was performed to ensure the model was able to predict gas temperatures and pressures, turbocharger rotor speeds, air mass flow rates and fuel mass flow rates within 15% of experimental data across the majority of the engine operating region. The smoke limit was approximated and governor gains were identified independently for low load operation below 30% max torque and high load operation above 30% max torque using the transient data set.

The remainder of this section is broken into two parts. In section 2.3.1 several torque ramps of increasing ramp rate are applied to the engine model to illustrate the response when the smoke limit is encountered. In section 2.3.2 the model is loaded using the torque ramps from Figure 2-4 to illustrate the improvement over the simplified model by incorporating the gain schedule.

2.3.1 Encountering the Smoke Limit

To illustrate the model encountering the smoke limit a 30% load ramp was applied to the state based model at ramp rates of 4.3 %/sec, 8.6 %/sec, and 12.9 %/sec as shown in Figure 2-7. The simulated engine response is shown as a percent of the commanded engine speed for each torque ramp. The air-fuel ratio is also included in the figure. The maximum speed deviation and recovery time for each ramp are summarized in Table 2-5.

As load is applied at 4.3%/sec the air-fuel ratio gradually decreases. The air-fuel ratio just hits the smoke limit as the torque ramp reaches the final steady value. As the turbocharger accelerates and provides more boost across the compressor the air fuel ratio rises and the engine stabilizes at a new steady state.

At a ramp rate of 8.6%/sec the air-fuel ratio approaches the smoke limit much faster. When the smoke limit is encountered the air-fuel ratio is held constant by the controller, causing the engine speed to drop further than seen during the lower ramp rate. As the turbocharger accelerates and provides more combustion air the controller adds more fuel to maintain the air-fuel ratio and the engine speed begins to recover. As engine speed reaches the commanded speed and the turbocharger continues to accelerate the air fuel ratio is lifted and the engine stabilizes at the new steady state.

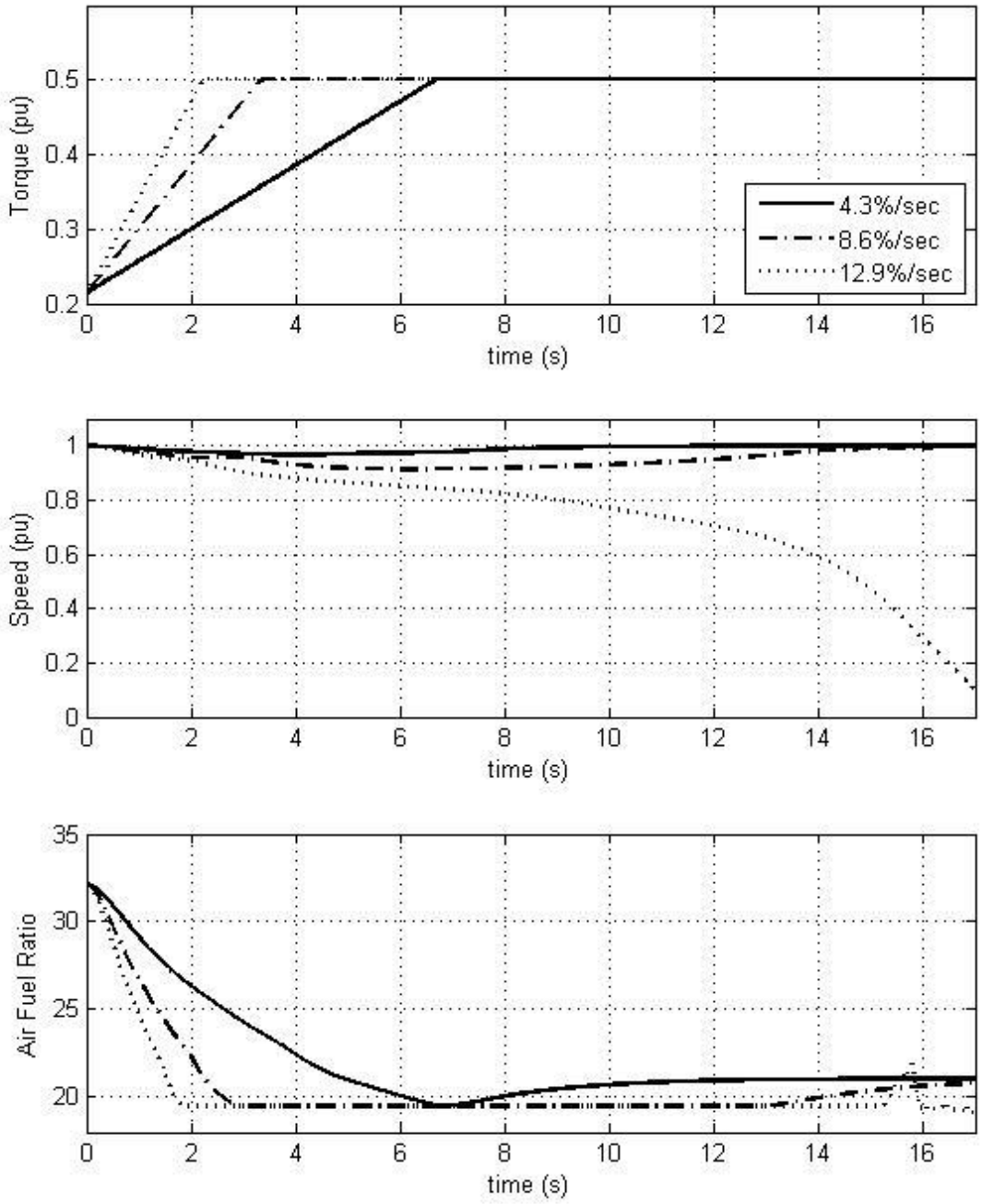

Figure 2-7: State-based model response to 30% torque ramps applied at different ramp rates. At a slow ramp rate of 4.3% maximum torque/sec the smoke limit is not encountered. At a ramp rate of 8.6%/sec the smoke limit is encountered and the engine is able to recover. At a ramp rate of 12.9%/sec the smoke limit is encountered resulting in a complete shutdown of the engine.

At a ramp rate of 12.9%/sec the air-fuel ratio rapidly drops until reaching the smoke limit. As the engine speed drops the turbocharger cannot provide sufficient combustion air to allow the engine to recover. As the engine speed drops, so does the boost provided by the turbocharger. The air fuel ratio is maintained at the rich limit by reducing fueling with the decreasing air flow rate, causing the engine speed to decelerate even more rapidly and finally resulting in a complete shutdown of the engine.

Table 2-5: Simulated speed deviation and recovery time during 30% torque ramp performed at different ramp rates

Ramp Rate	Speed Deviation	Recovery Time
4.3%/sec	3.3%	8.3 sec
8.6%/sec	8.6%	14.9 sec
12.9%/sec	100%	(Full shut down)

2.3.2 Response Improvement at Low Load

To illustrate the improvement over the simplified model at low load, the same torque ramps as in section 2.1.2 were applied to the state based model. The simulated response of the state based model is shown in Figure 2-8, and the speed deviation and recovery time during each load ramp are summarized in Table 2-6. By comparing the values to those of the simplified model in Table 2-3 it is evident the addition of a gain schedule improved the agreement between the simulation and the experimental data.

Table 2-6: Speed deviation and recovery time of experimental test and state based model during 20% torque ramp performed at low, medium and high load

	Experiment		State Based Model	
Initial - Final Load	Speed Deviation	Recovery Time	Speed Deviation	Recovery Time
10% – 31%	5.5%	6.7 sec	5.4%	8.2 sec
31% – 53%	3.6%	4.6 sec	3.1%	4.6 sec
53% - 74%	2.9%	4.5 sec	3.9%	4.3 sec

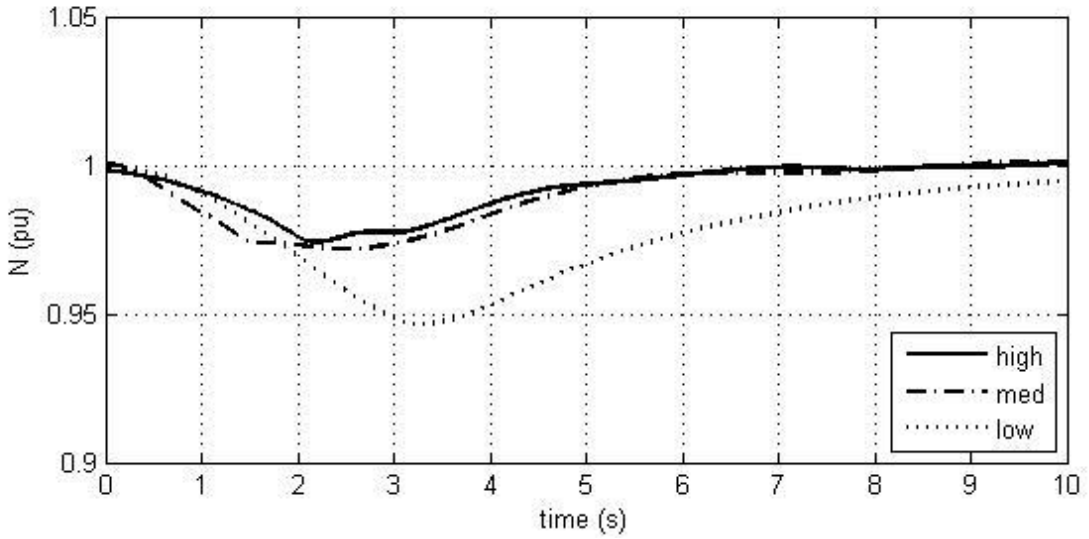

Figure 2-8: Simulated response of state based model with gain schedule to 20% torque ramps performed at low, medium and high load

2.4 Conclusions

The simplified engine model reviewed in Chapter 2.1 can provide an approximation of the dynamic response of a diesel engine employed in microgrid applications, however does not consider controller limits encountered during experimental transient testing. As a result the simplified model no longer accurately predicts the maximum speed excursion or recovery time during a load step in which these limits are encountered.

The experimental data and modeling results in this chapter suggest that a state-based model replace the simplified model in transient applications such as black-start and unplanned islanding of a microgrid in order to consider real limitations of diesel engines. The state-based mean value model discussed in section 2.2 provides system states required to implement engine controllers which include these limitations. A governor model with a smoke limit and gain schedule is presented as an example. The smoke limit is employed to prevent the engine from running too rich, a condition caused by increasing fueling without increasing boost supplied by the

turbocharger sufficiently when accepting load. The gain schedule is incorporated in order to improve the response of the engine at various loading regimes when compared to the experimental data.

Additionally the state-based dynamic model is capable of operating across a range of engine speeds, which extends the utility of the model to variable speed applications such as driveline dynamics in high pressure pumping and heavy duty vehicles.

3 Dynamic Turbocharged Natural Gas Engine

Natural gas engines generally do not perform as well as diesel engines under transient loading. Unlike diesel engines which typically run with excess air available allowing rapid increases in fuel rate without encountering a rich limit, the air-fuel ratio in a lean burn spark ignited natural gas engine is controlled within a much narrower range. Excess air is required to reduce the peak in-cylinder temperature as a method of reducing emissions of oxides of nitrogen [25] [24]. Lower combustion temperatures also improve engine efficiency by reducing heat transfer losses [26]. Fueling can also be too lean, resulting in misfire, flame quenching, and increased emissions of unburnt hydrocarbons [25] [27]. To avoid decreasing the power density of lean burn engines, turbochargers are frequently used to boost intake manifold pressure. Since fueling is controlled within a narrow range of air-fuel ratio an accurate model of the air handling system is required to model the response of the natural gas engine during transients. The model developed in this chapter is motivated by natural gas engines employed in two application areas: (1) Micro-grid power systems, and (2) as the driver in hydraulic fracturing pump drivetrains.

A private report for the Marine Corps Air Station Miramar Micro-grid prepared by the National Renewable Energy Laboratory [20] determined that Natural Gas engines were of interest to military micro-grid applications, and that there is a need for better simulation models to represent the transient performance of engines in the size range of 100s-1000s kW. A public report of this effort [21] identifies the base's reliance on natural gas as a major energy source and the interest in 3MW of landfill gas generation. MIT Lincoln Laboratory's report [2] also stated the NG system is largely independent of the electrical system, so μGrids operating on NG engines could still be considered "secure," in the event the electrical system failed.

The use of dedicated natural gas engines on drilling rigs is motivated by reduced emissions, reduced cost, improved maintenance characteristics, and improved domestic energy security [22]. Historically diesel has been the primary fuel for drilling operations due to the certainty around diesel handling and performance [22]. Dual-fuel solutions which supplement natural gas as a fuel in a retrofitted diesel engine have been utilized to reduce diesel fuel consumption, reducing costs and extending run times on existing diesel tanks [23]. The driveline dynamics when the transmission engages a new gear are very demanding on the engine and uncertainty on natural gas engine performance during variable load operation has been a barrier to adopting dedicated natural gas engines to this application [22]. A model is needed to simulate the response of the engine during these transients to develop control strategies that may enable the natural gas engine to be utilized in this application.

3.1 State-Based Natural Gas Model

A state-based mean valued model of a turbocharged spark-ignited natural gas engine is presented in this chapter. The model includes a single stage turbocharger, throttle, and air-fuel controller as shown in the schematic in Figure 3-1. Much of the model is adapted from the diesel engine model presented in Part II. The key differences are (1) the division of the intercooler and intake manifold into two volumes separated by the throttle, and (2) the replacement of the governor with a constant air-fuel ratio controller.

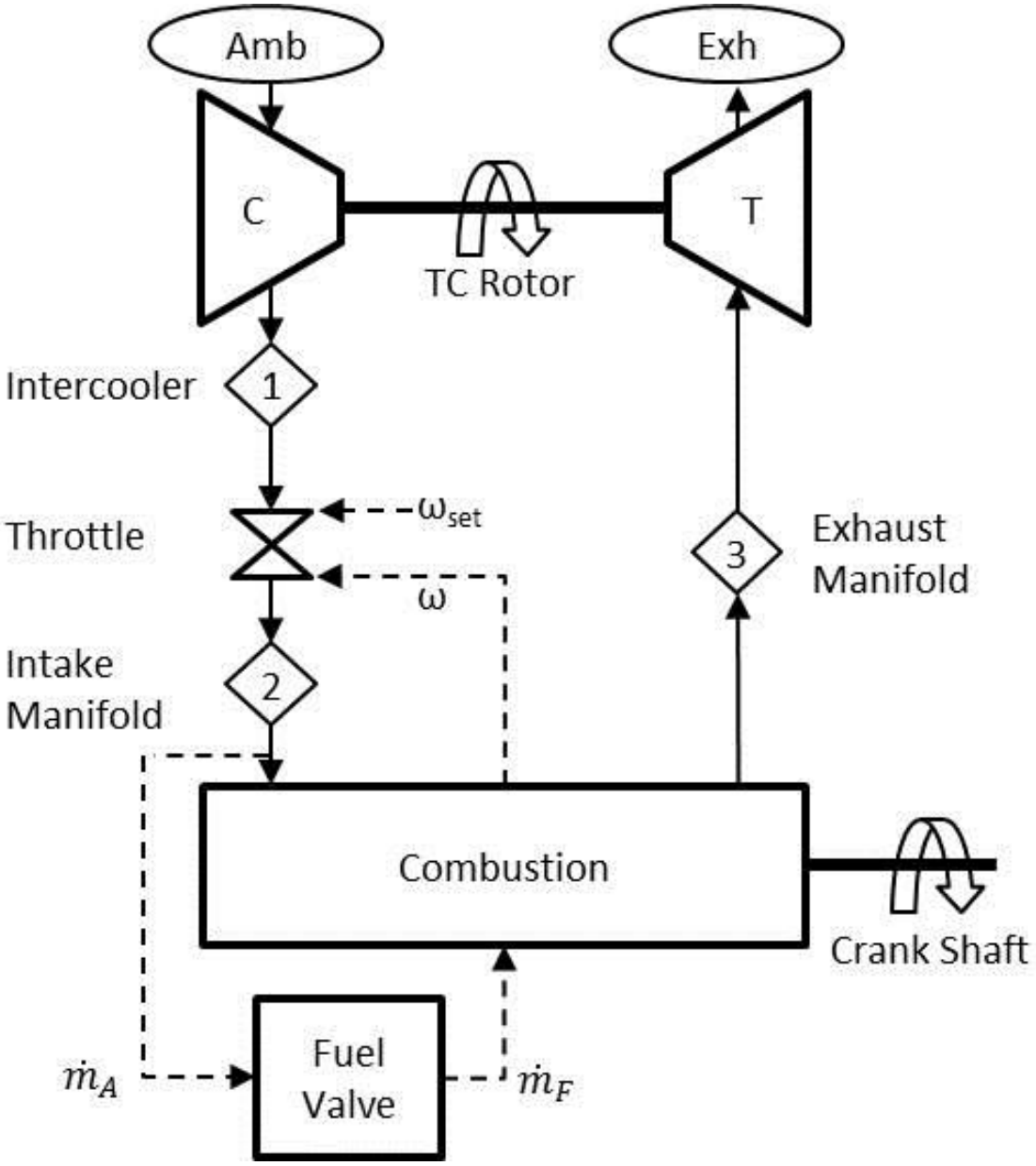

Figure 3-1: Turbocharged lean-burn natural gas model schematic including primary components

3.1.1 Throttle

The engine speed control is performed by the throttle as illustrated in Figure 3-2. The throttle position, x_T, is controlled by a PID controller saturated between 0 (fully closed) and 1 (fully open). The PID responds to the difference between the commanded engine speed and the

measured engine speed by opening and closing the throttle. The model uses a constant discharge coefficient, C_D, and a lookup table relating the throttle position to throttle area, $A = f(x_T)$.

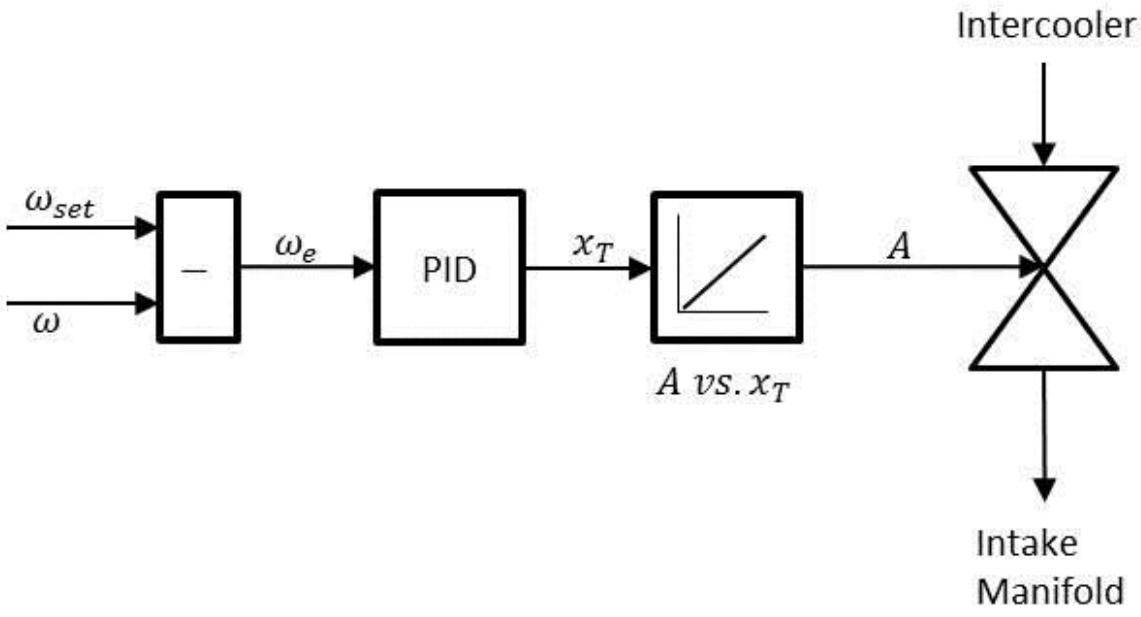

Figure 3-2: Throttle schematic including PID position controller, throttle area lookup table, and variable area orifice.

The flow through the throttle is modeled as a variable area orifice located between the intercooler and the intake manifold. Choked, sub-sonic and laminar flow regimes are included and selected as a function of pressure ratio [36]. A critical pressure ratio at which the flow becomes choked is calculated as:

$$B_{cr} = \left(\frac{2}{\gamma + 1}\right)^{\frac{\gamma}{\gamma - 1}} \tag{29}$$

If the pressure ratio $\frac{P_d}{P_u} < B_{cr}$ the choked mass flow rate is calculated as

$$\dot{m} = C_D A P_u \sqrt{\frac{\gamma}{RT_u} B_{cr}^{\frac{\gamma+1}{\gamma}}} \tag{30}$$

If the pressure ratio $\frac{P_d}{P_u} > B_{cr}$ the mass flow rate is subsonic and calculated as:

$$\dot{m} = C_D A P_u \sqrt{\frac{2\gamma}{RT_u(\gamma-1)}\left(\left(\frac{P_d}{P_u}\right)^{\frac{2}{\gamma}} - \left(\frac{P_d}{P_u}\right)^{\frac{\gamma+1}{\gamma}}\right)} \tag{31}$$

If the pressure ratio is above a laminar limit, $\frac{P_u}{P_d} > B_{lam}$, the laminar mass flow is calculated as:

$$\dot{m} = \frac{C_D A T_u^{-0.5} \sqrt{\frac{2\gamma}{R(\gamma-1)}\left(B_{lam}^{\frac{2}{\gamma}} - B_{lam}^{\frac{\gamma+1}{\gamma}}\right)}}{1 - B_{lam}} \tag{32}$$

The energy transferred from the upstream volume (intercooler) through the orifice to the downstream volume (intake manifold) is calculated as:

$$\dot{Q} = \dot{m} C p T_u \tag{33}$$

3.1.2 Fuel Valve

The air-fuel ratio in a lean-burn natural gas engine is controlled within a narrow range. A rich limit is in place to reduce peak cylinder temperature (a mechanism to reduce NOx emissions and improve efficiency) and a lean limit to avoid engine misfire. The fuel valve model maintains a constant air-fuel ratio provided to the combustor. The air flow rate into the combustor is measured and the fuel rate is calculated using the commanded air-fuel ratio. By adjusting the throttle position the air flow rate through the engine responds, and therefore the fuel addition and torque production of the engine. An air fuel ratio of 27.5 was identified from steady state experimental data and used in simulation.

3.2 Natural Gas Model Validation and Results

Steady state data from a Cummins QSK60G operating at 50%, 75%, 90%, and 100% load is used to validate the natural gas engine model. This engine is typically employed in constant speed applications in power generation, limiting data to a single speed, 1800 rpm. Figure 3-3 shows steady state error in air mass flow rate during simulation. Steady state error in fuel rate, air-fuel ratio, and exhaust temperature are shown in Figure 3-4 through Figure 3-6 respectively.

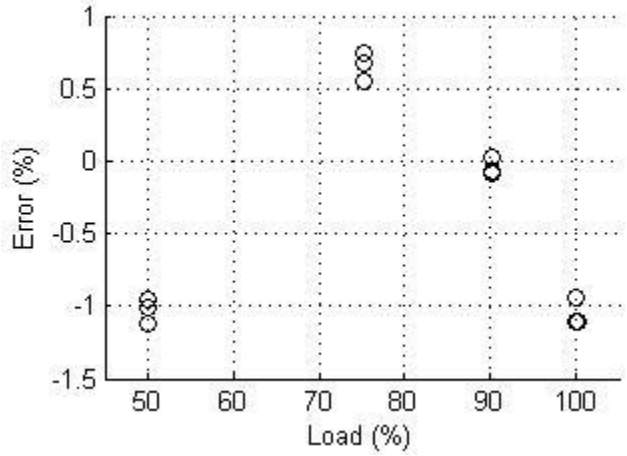

Figure 3-3: Natural gas model validation – Steady state error in air mass flow rate at 50%, 75%, 90% and 100% load

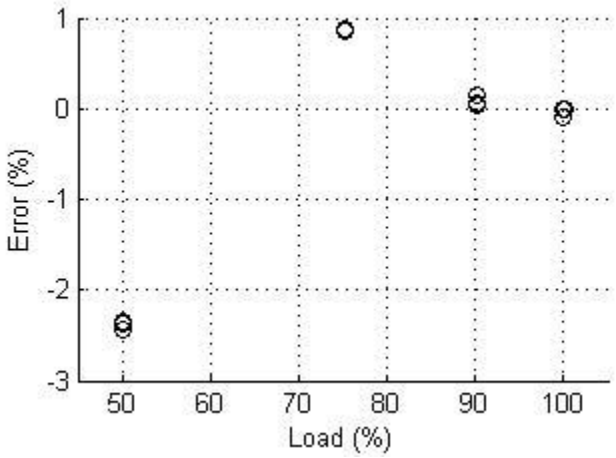

Figure 3-4: Natural gas model validation – Steady state error in fuel mass flow rate at 50%, 75%, 90% and 100% load

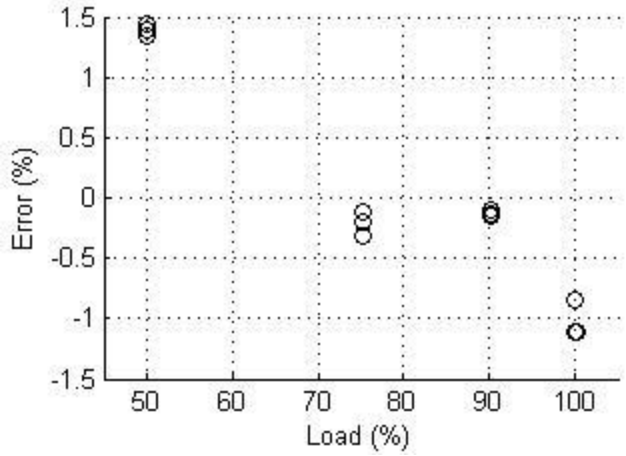

Figure 3-5: Natural gas model validation –Steady state error in air-fuel ratio at 50%, 75%, 90% and 100% load

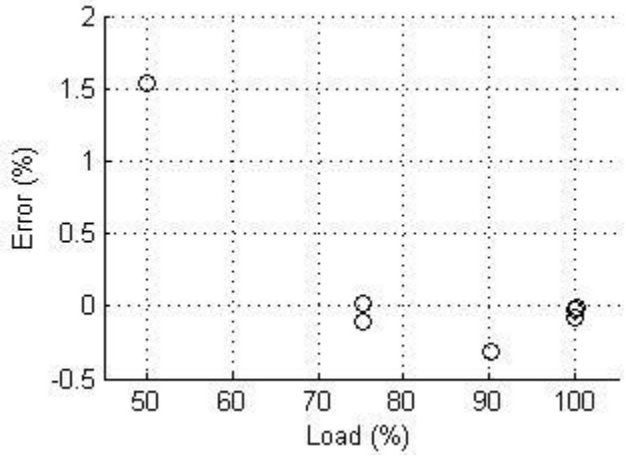

Figure 3-6: Natural gas model validation –Steady state error in exhaust temperature at 50%, 75%, 90% and 100% load

Due to limited availability of data the natural gas model is not validated against experimental data during transients, however, the majority of the model is composed of the same validated subsystems as used by the diesel engine model in Part II. The transient response of the natural gas engine model is illustrated in Figure 3-7 for two load steps applied at a ramp rate of 833 ft-lb/sec and a commanded speed of 1800 rpm. Ramp A is applied from 15% to 40% max torque. Ramp B is applied from 40% to 65% max torque.

During ramp A the throttle is opened allowing the intake manifold pressure, P_{2A}, to increase. As the air flow rate through the engine and therefore to the turbine increases, the compressor outlet pressure, P_{1A}, also increases. As the engine speed recovers and the compressor outlet pressure continues to rise, the throttle begins to close to maintain the intake manifold pressure at the new steady state. The minimum engine speed encountered during the simulation is 1711rpm, corresponding to a 4.9% speed deviation.

During ramp B the engine does not recover. As the engine speed begins to fall, the throttle opens fully, which reduces the pressure drop across the throttle to nearly zero as the intake manifold pressure, P_{2B}, approaches the pressure upstream of the throttle, P_{1B}. However, the engine speed continues to drop when the throttle is fully open, which reduces the airflow to the turbine. As this occurs the turbocharger begins to decelerate and the compressor outlet pressure begins to fall. This causes the engine speed to continue to drop, until the engine shuts down.

Since no transient data is available to compare the response to, the controller gains could not be tuned against experimental data. By increasing the gains, the throttle can be opened faster, possibly allowing the engine to recover from the ramp at higher load. However a faster throttle does not necessarily mean a faster response, since the fueling is proportional to air flow and the air flow is limited by the performance of the turbocharger and its ability to accelerate quickly.

The results shown in Figure 3-7 are attained using a guess at the throttle controller gains, however they illustrate the expected behavior of the natural gas engine, namely its inability to rapidly accept load due to the tight coupling of the air and fuel system.

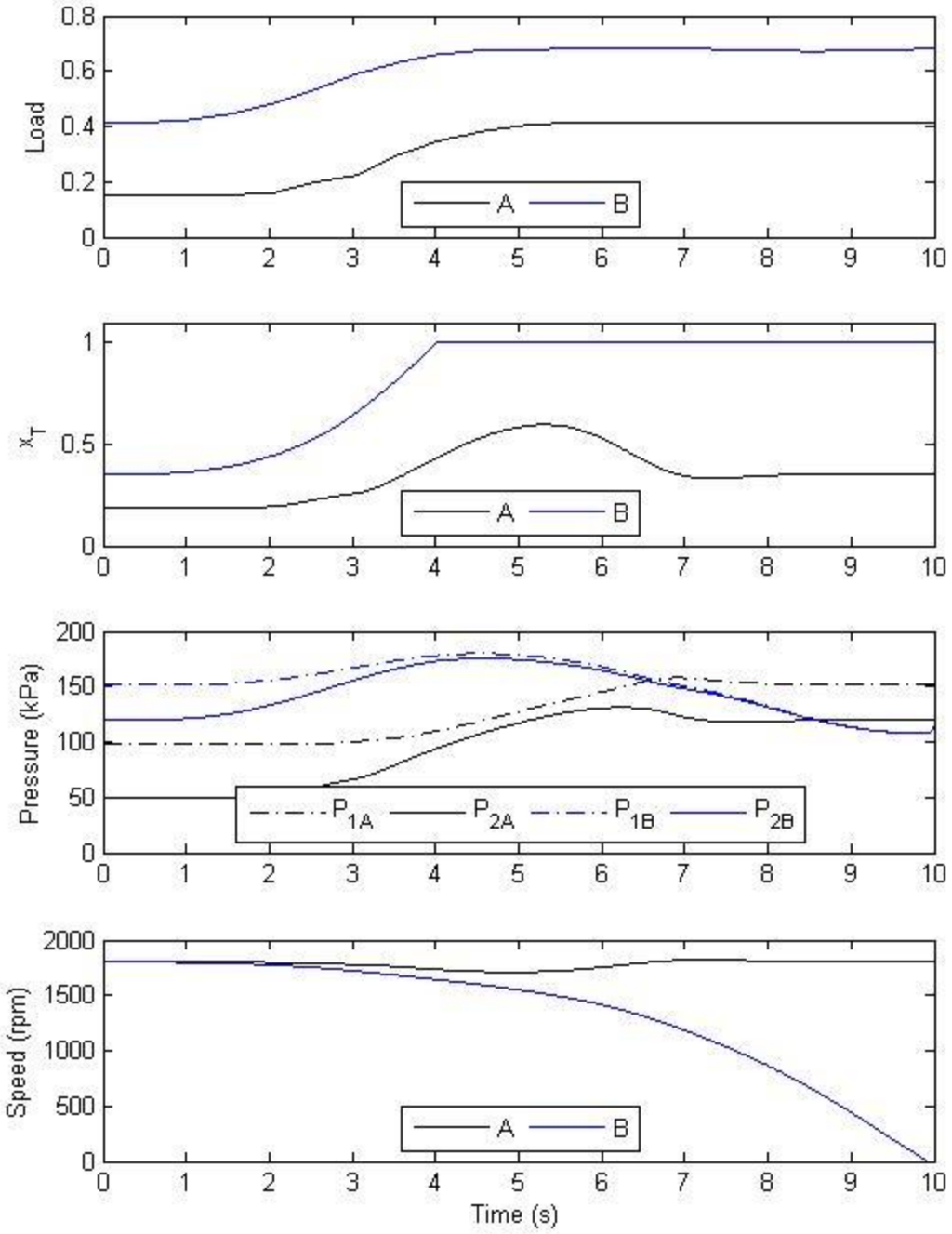

Figure 3-7: Natural gas model validation – Simulated transient response including applied load, throttle position, compressor outlet pressure (P_1) and intake manifold pressure (P_2), and engine speed to two load steps; Load step A from 15% to 40% load, and load step B from 40% to 65% load.

3.3 Conclusions

The natural gas engine model developed in this chapter is adapted from the framework of the state-based diesel engine model discussed in Chapter 2, with the addition of a throttle in the intake air system. The throttle, modeled as a variable area orifice, provides an adjustable flow restriction between the compressor outlet and the intake manifold. The engine power can be controlled effectively by adjusting the throttle position, however, due to the lagging dynamics of the turbocharger the system cannot accept load rapidly.

The model is capable of reproducing air and fuel flow rates within 2% of the experimental data provided during steady state validation. Since transient data was not available, the controller gains could not be tuned to match the dynamic performance of the system, however the results illustrate the expected general behavior during load acceptance simulations.

4 Modeling of Hydraulic Fracturing using a Lean Burn Natural Gas Engine

Historically diesel has been the primary fuel for drilling operations due to the low cost and certainty around diesel handling and performance [22]. With the increasing cost of diesel, drilling companies have seen a significant increase in operating costs. The use of dedicated natural gas engines in other high horsepower applications to benefit from the low cost of fuel and/or emissions reductions is well established, however due to the uncertainty of lean burn natural gas engine transient performance they have not been widely adopted in the drilling industry. This appendix presents a case study in which a validated driveline model is used to simulate a shifting event during a hydraulic fracturing job and investigate the natural gas engine response.

The pump and driveline are modeled in the study, and were validated against confidential experimental data provided by Halliburton. The system consists of the engine, torque converter, eight speed transmission, and pump as illustrated in Figure 4-1.

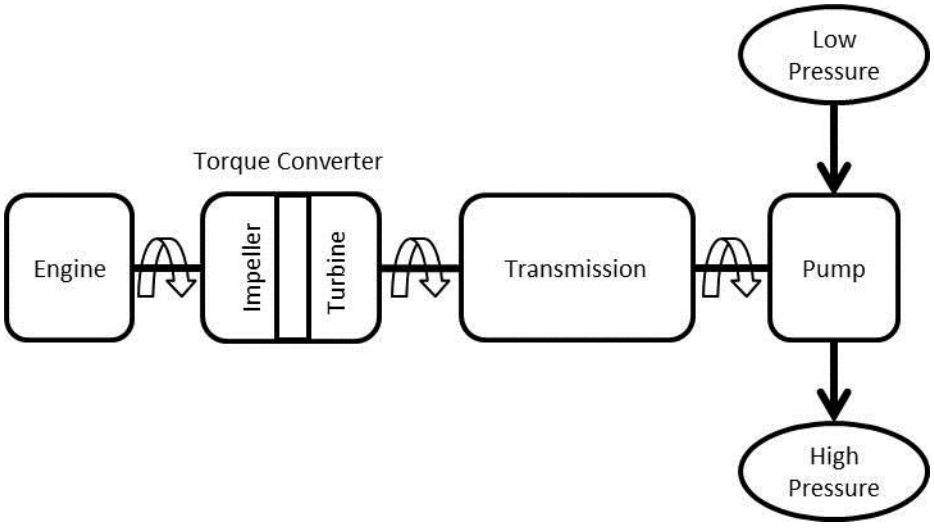

Figure 4-1: Pump and driveline system schematic

The torque converter and transmission are not designed specifically for this application, but adapted from heavy-duty vehicles. As a result, the torque converter and transmission are operated in an unconventional manner. A lockup clutch is included in the torque converter to connect the impeller to the turbine for direct torque transfer. Since there is little inertia associated with the driveline downstream of the torque converter, relative to the large torque applied by high pressures in the pump cylinders, the drive train can come to a complete stop when the torque converter clutch is disengaged in order to shift gears in the transmission. This is in part due to the torque converter being undersized for this application. However, this method of operation reduces wear in the transmission when operating under these extreme conditions.

4.1 Custom Driveline Component Models and Subsystems

The driveline model is implemented in MATLAB Simscape using components from the foundation library and several custom components described in this section.

4.1.1 Locking Torque Converter

A torque converter with a lockup clutch is implemented similar to the torque converter available in SimDriveline with lagged torque transfer [37]. There are two conserving rotational nodes, I and T, representing the impeller and turbine respectively. A rotational inertia must be included upstream, connected to the impeller, while the inertia response of the turbine is included internal to this component. A physical signal is provided to engage the lock up mechanism. The lock is disengaged if the lock signal = 0, and engaged if >0.

Lagged torque transfer is implemented as

$$k_1\left(\frac{dR_t}{dt}\right) = R_t^* - R_t \tag{34}$$

where k_1 is a time constant, R_t is the torque ratio of the converter ($R_t = \frac{\tau_{turbine}}{\tau_{impeller}}$), and R_t^* is the torque ratio target.

If the clutch is unlocked the torque converter is modeled as in the SimDriveline torque converter component. A lookup table is used to determine the torque ratio target and capacity factor as a function of the converter speed ratio, $R_\omega = \frac{\omega_{turbine}}{\omega_{impeller}}$.

$$R_t^* = f(R_\omega) \tag{35}$$

$$K = f(R_\omega) \tag{36}$$

The capacity factor is then used to calculate the torque on the input shaft from the input shaft speed.

$$\tau_{impeller} = \frac{\omega_{impeller}^2}{K^2} \tag{37}$$

The acceleration of the turbine based on the net torque applied by the torque converter fluid and the load is calculated as

$$\frac{d\omega_{turbine}}{dt} = \frac{R_t \tau_{impeller} - \tau_{load}}{J_{turbine}} \tag{38}$$

Numerical integration of equation 68 provides the speed of the torque converter output.

If the clutch is locked the torque ratio target is set to unity for unity torque transfer, and equation 68 is replaced with a new first order differential equation in terms of the turbine speed which uses a time constant, k_2, to represent the slipping of the clutch until the speed ratio is brought to unity ($\omega_{impeller} = \omega_{turbine}$). This model simulates the rate of clutch engagement, albeit in a very simplified and computationally efficient manner.

$$R_t^* = 1 \tag{39}$$

$$k_2 \frac{d\omega_{turbine}}{dt} = (\omega_{impeller} - \omega_{turbine}) \tag{40}$$

The parameters shown in Table 4-1 are used to define the torque converter. Using the capacity factor and engine speed the input torque can be calculated, then the output torque can be determined using the torque ratio. Figure 4-4 illustrates the torque output of the torque converter across a range of engine speeds and slip ratios. The torque ratio and capacity factor are plotted against speed ratio in Figure 4-2 and Figure 4-3 respectively.

Figure 4-5 and Figure 4-6 show the simulation results when the impeller is driven at 1800 rpm with a 6000 ft-lb load applied to the turbine. When the clutch is engaged at 5 seconds the turbine speed rises to match the impeller speed and the torque seen on the impeller rises to that of the load. Figure 4-6 shows the speed ratio and torque ratio roll to unity (direct power transfer) when the clutch is engaged. When the clutch is disengaged at 10 seconds the torque converter begins to slip again and the impeller torque drops. As the slip increases, the impeller torque increases until reaching the steady state. Figure 4-6 shows the torque ratio increases rapidly upon disengaging the lockup clutch. This is because at a speed ratio of unity, the torque converter transfers no torque (no torque is applied to the impeller by the fluid until the turbine begins to slip).

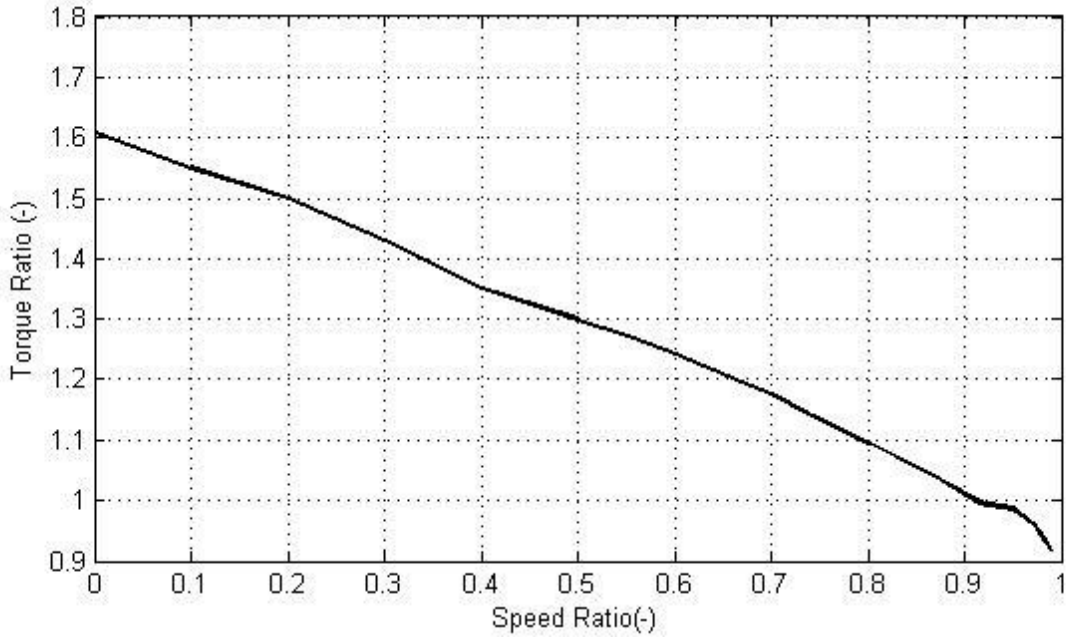

Figure 4-2: Torque converter torque ratio.

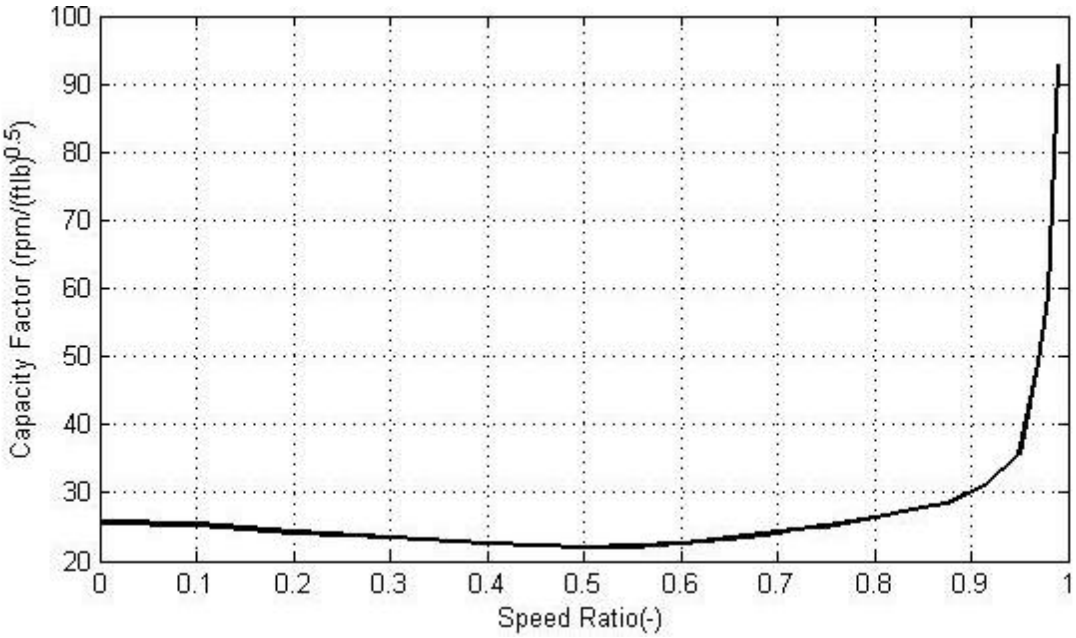

Figure 4-3: Torque converter capacity factor.

Table 4-1: Torque converter model parameters

Speed Ratio	Torque Ratio	Capacity Factor
0	1.61	25.61
0.1	1.55	25.29
…	…	…
0.98	0.941	59.16
0.99	0.917	92.87

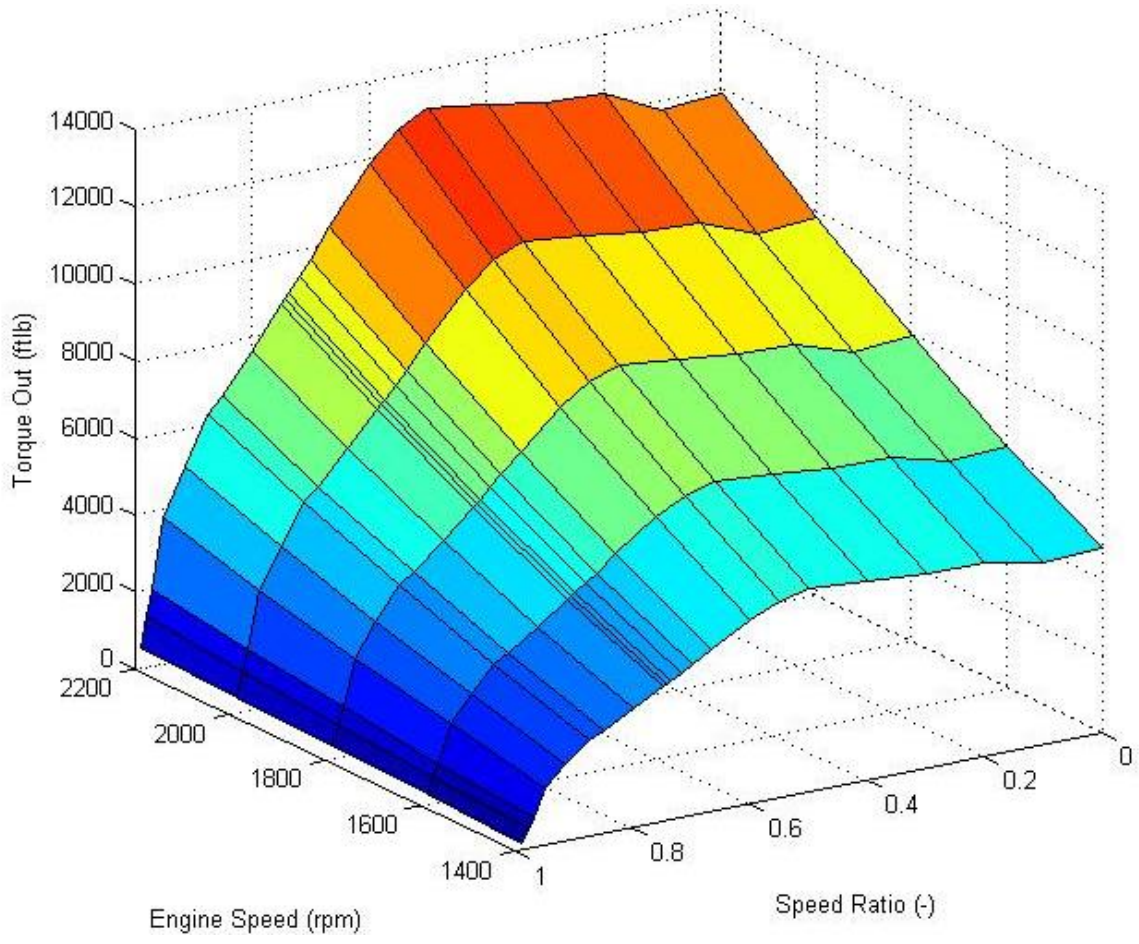

Figure 4-4: Output torque calculated from torque ratio and capacity factor and mapped against engine speed and torque converter speed ratio.

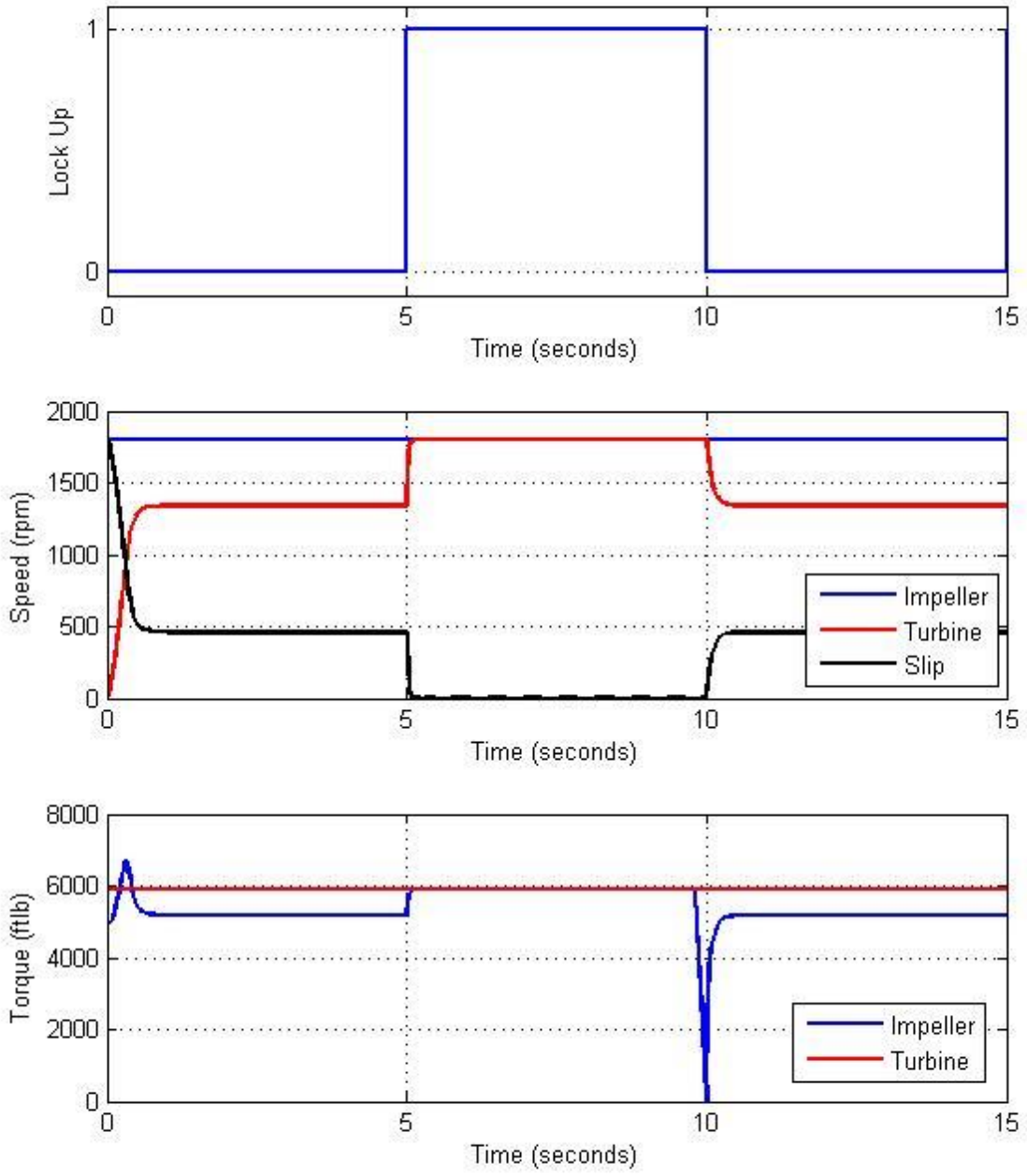

Figure 4-5: Torque converter validation: Impeller driven at 1800 rpm with 6000 ft-lb load applied to turbine. Lock engaged at 5 sec and disengaged at 10 sec.

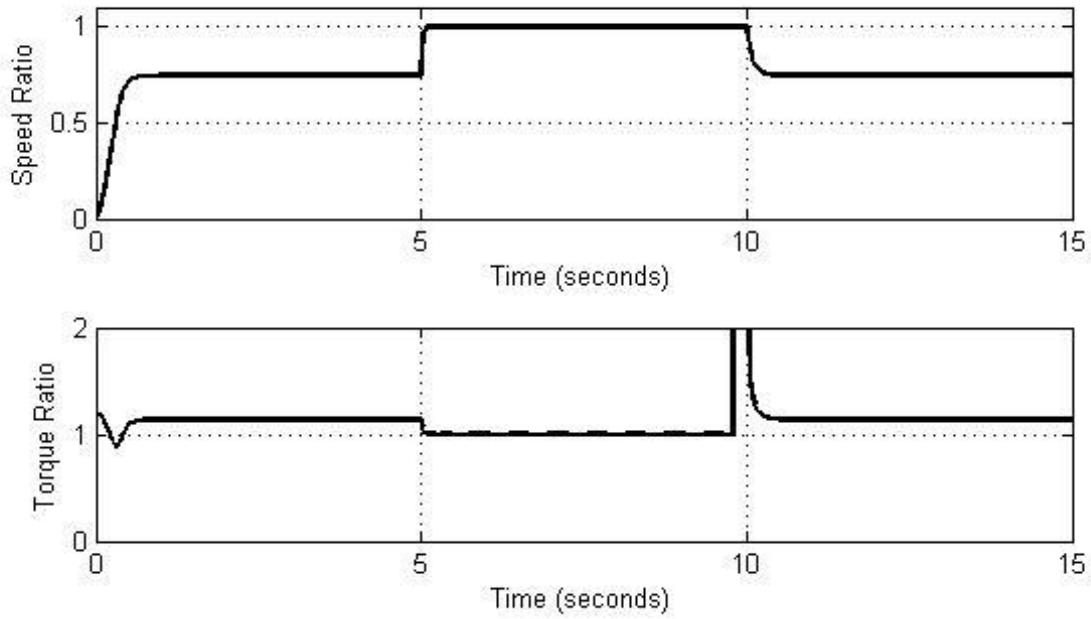

Figure 4-6: Torque converter validation: Speed ratio and torque ratio during simulation

4.1.2 Simplified Transmission

The block represents a simple transmission, modeled after the Simscape ideal, non-planetary, fixed gear ratio gear box. Connections S and O are mechanical rotational conserving ports associated with the box input and output shaft, respectively. An input signal sets the desired gear ratio, $G = \left(\frac{\omega_{in}}{\omega_{out}}\right)_{desired}$. The block generates torque in positive direction if a positive torque is applied to the input shaft and the ratio is assigned a positive value. Parameters for spring and damping coefficients, k and c, smooth the transition during a change in gear ratio.

An arbitrary angle, φ, is used to apply a smooth change between gears.

$$\dot{\varphi} = G\omega_{out} - \omega_{in} \tag{41}$$

The angle $\emptyset$ increases ($\frac{d\emptyset}{dt} > 0$) if $G\omega_{out} > \omega_{in}$, decreases ($\frac{d\emptyset}{dt} < 0$) if $G\omega_{out} < \omega_{in}$, and reaches a constant value ($\frac{d\emptyset}{dt} = 0$) when $G\omega_{out} = \omega_{in}$.

The input torque and output torque are then calculated as

$$\tau_{in} = c\dot{\varphi} + k\varphi \tag{42}$$

$$\tau_{out} = G\tau_{in} \tag{43}$$

When the angle ∅ reaches a constant value (the input and output shaft speeds are related correctly by the gear ratio) the input torque reaches a constant value.

Figure 4-7 shows the validation model results. The input shaft speed was set at 1800 rpm and the output shaft was loaded at 10000 Nm (~7300 ft-lb). The results show the output speed rising and the torque required at the input of the transmission rising as the transmission is shifted from 1st through 8th gear. The speed of the output shaft and the required input torque fall as the transmission is shifted down through the gears again. The constants $k_1$and k_2 were selected to ensure the output shaft speed quickly rolls into steady state without ringing as each gear is engaged. The values selected are shown in Table 4-2.

Table 4-2: Transmission spring and damping constants

Parameter	Value	Units
c	50	$\frac{Nm}{\left(\frac{rad}{s}\right)}$
k	1000	$\frac{Nm}{rad}$

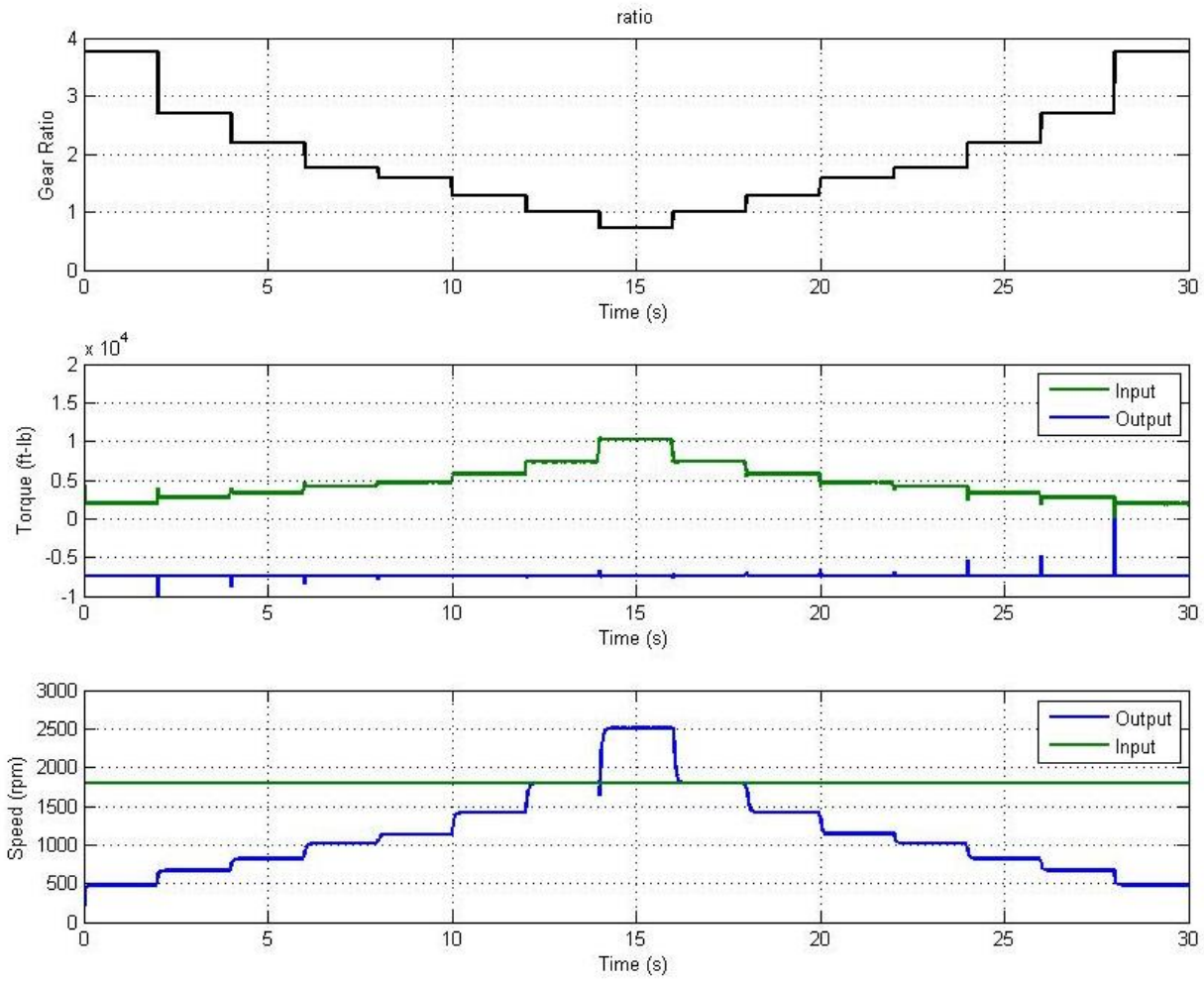

Figure 4-7: Transmission Validation Results

4.1.3 Fluid Pump

The fluid pump models the positive displacement of a cylindrical piston pump and the torque applied on the drive shaft by the cylinder pressure as a function of crank angle. The equations are derived using the geometry in Figure 4-8.

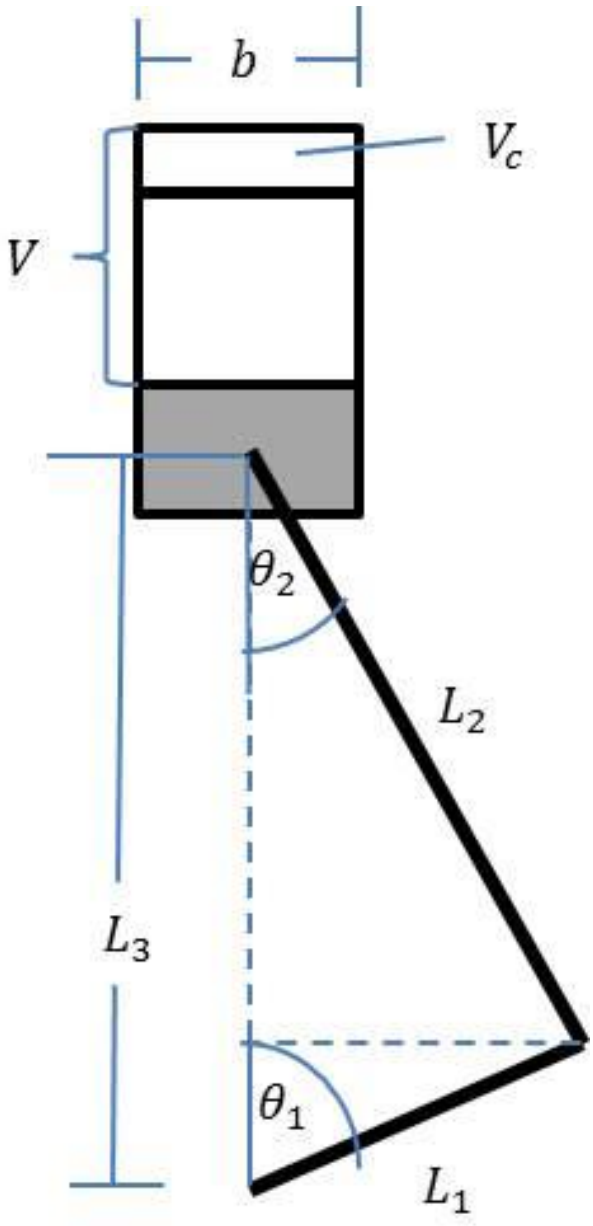

Figure 4-8: Positive displacement fluid pump model geometry

The distance between the wrist pin on the piston and the crank shaft center, L_3, can be calculated from trigonometric relations as a function of the crank arm length, L_1, the connecting rod length, L_2, and the crank arm position, θ_1 as

$$L_3 = L_1 \cos(\theta_1) + \sqrt{L_2^2 - (L_1 \sin(\theta_1))^2} \tag{44}$$

When the piston is at top dead center, $\theta_1 = 0$, the length $L_3 = L_1 + L_2$ and at bottom dead center the length $L_3 = L_2 - L_1$. The cross-sectional area of the cylinder is calculated from the piston bore as $A = \frac{\pi}{4} b^2$, and the chamber volume can be calculated as

$$V = A(L_1 + L_2 - L_3) + V_c \tag{45}$$

where V_c is the clearance volume. By substituting Equation 44 into Equation 45, and taking the derivative, the volumetric flowrate due to pumping can be calculated as

$$\dot{V} = A\left(\frac{d\theta_1}{dt}\right)\left(L_1 \sin(\theta_1) + \frac{L_1^2 \sin(\theta_1)\cos(\theta_1)}{\sqrt{L_2^2 - L_1^2 \sin^2(\theta_1)}}\right) \tag{46}$$

The pressure in the cylinder applies a torque to the crankshaft calculated as

$$\tau = \frac{P_{gage} A L_1}{\cos(\sin^{-1}(L_1 \sin(\theta_1)/L_2))} \cos(\theta_2) \tag{47}$$

where the angle $\theta_2$is calculated as

$$\theta_2 = \frac{\pi}{2} - \theta_1 - \sin^{-1}\left(\frac{L_1 \sin(\theta_1)}{L_2}\right) \tag{48}$$

4.1.4 Pump Cylinder Subsystem

A pump cylinder subsystem model, shown in Figure 4-9, is composed of the fluid pump component, the variable hydraulic chamber [38] Simscape component to model compressibility effects, and two hydraulic check valves [39] oriented to model the inlet and outlet valves. The crankshaft (1) is a Simscape rotational node, and the inlet (2) and outlet (3) are Simscape hydraulic nodes. The check valves allow flow from A to B when the pressure across the check valve exceeds a cracking pressure.

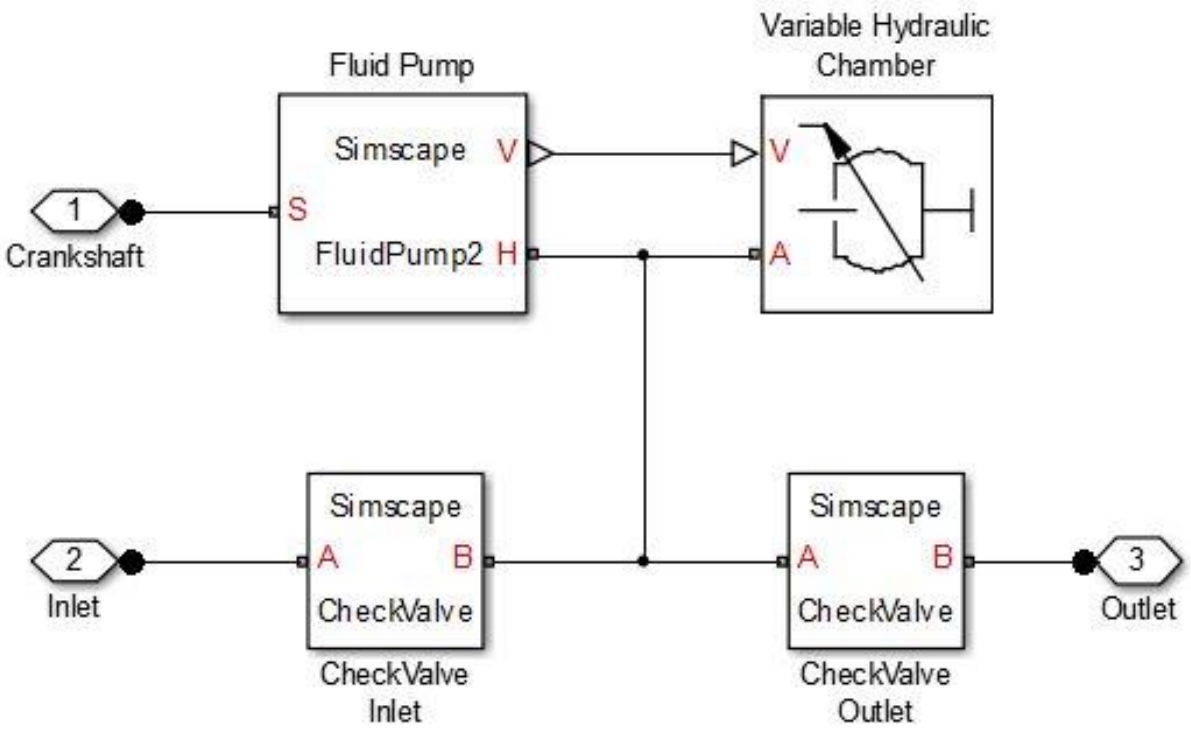

Figure 4-9: Simscape pump cylinder subsystem

The operation if the pump cylinder subsystem is shown in Figure 4-10. Starting at bottom dead center (maximum volume at ~21 seconds), the cylinder pressure rapidly increases as the cylinder volume begins to decrease. This causes the outlet valve to crack open and allow flow out of the cylinder as the volume continues to decrease. When the cylinder reaches top dead center (minimum volume at ~ 21.6 seconds) the outlet valve has closed fully. As the cylinder volume increases during the expansion stroke, the pressure drops rapidly until the inlet check valve cracks open, allowing fluid to flow into the cylinder from the low pressure source.

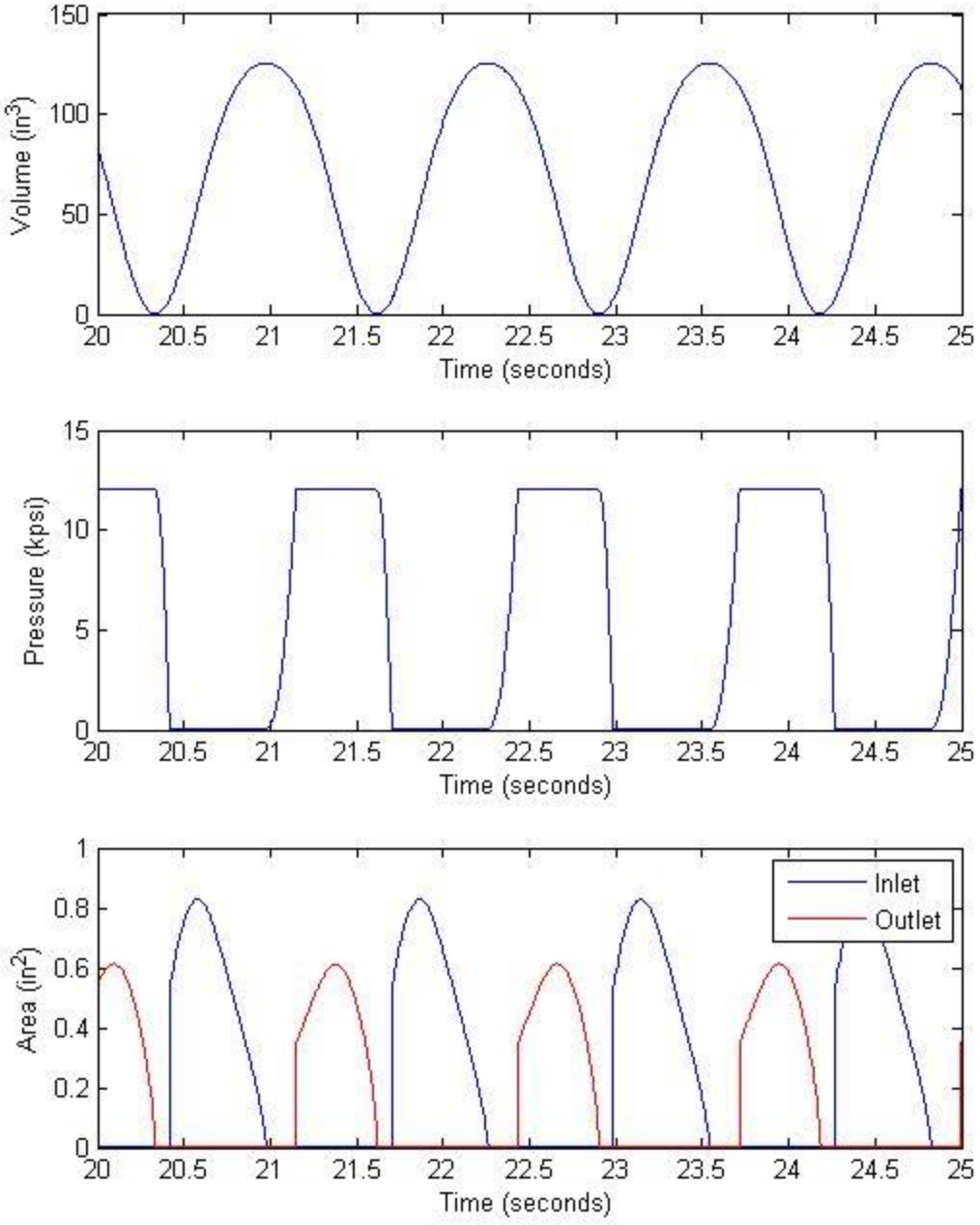

Figure 4-10: Pump cylinder volume, pressure, and inlet/outlet valve area operating at constant speed against 12000 psi

4.1.5 Multi Cylinder Pump Subsystem

A multi cylinder pump can be created by connecting several cylinder subsystems in parallel. The subsystem shown in Figure 4-11 contains five individual cylinder models. A gear box [40] from the SimDriveline library provides a torque reduction on the input shaft. The pump inertia is modeled by a Simscape rotational inertia component from the foundation library. Each cylinder is driven by the crankshaft and displaces fluid from the inlet to the outlet hydraulic nodes. Compressibility effects are captured in each cylinder by the variable hydraulic chamber while the fluid pump component models the volumetric pumping and transmission of torque to the crankshaft.

Figure 4-12 shows the volume of the five pump cylinders during operation at constant speed. Each cylinder is offset by 72 degrees crank angle to orient them symmetrically around the crankshaft. The figure also shows the net flowrate at the pump outlet (connection 2 in Figure 4-11) and the net torque applied by the crankshaft (connection 3 in Figure 4-11) to the gear box input.

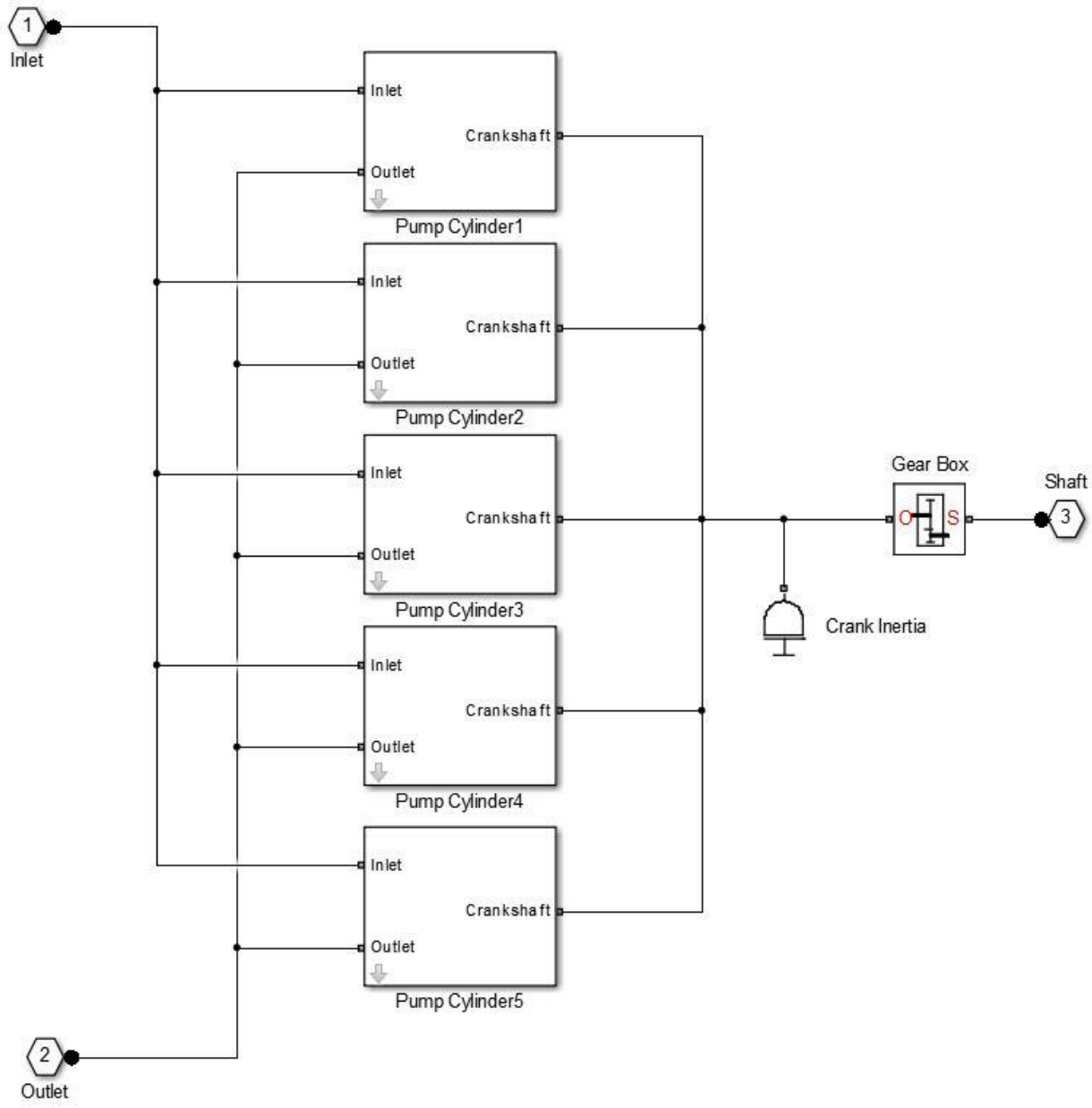

Figure 4-11: Simscape pump model including five individual cylinders, pump inertia, and reduction gear box

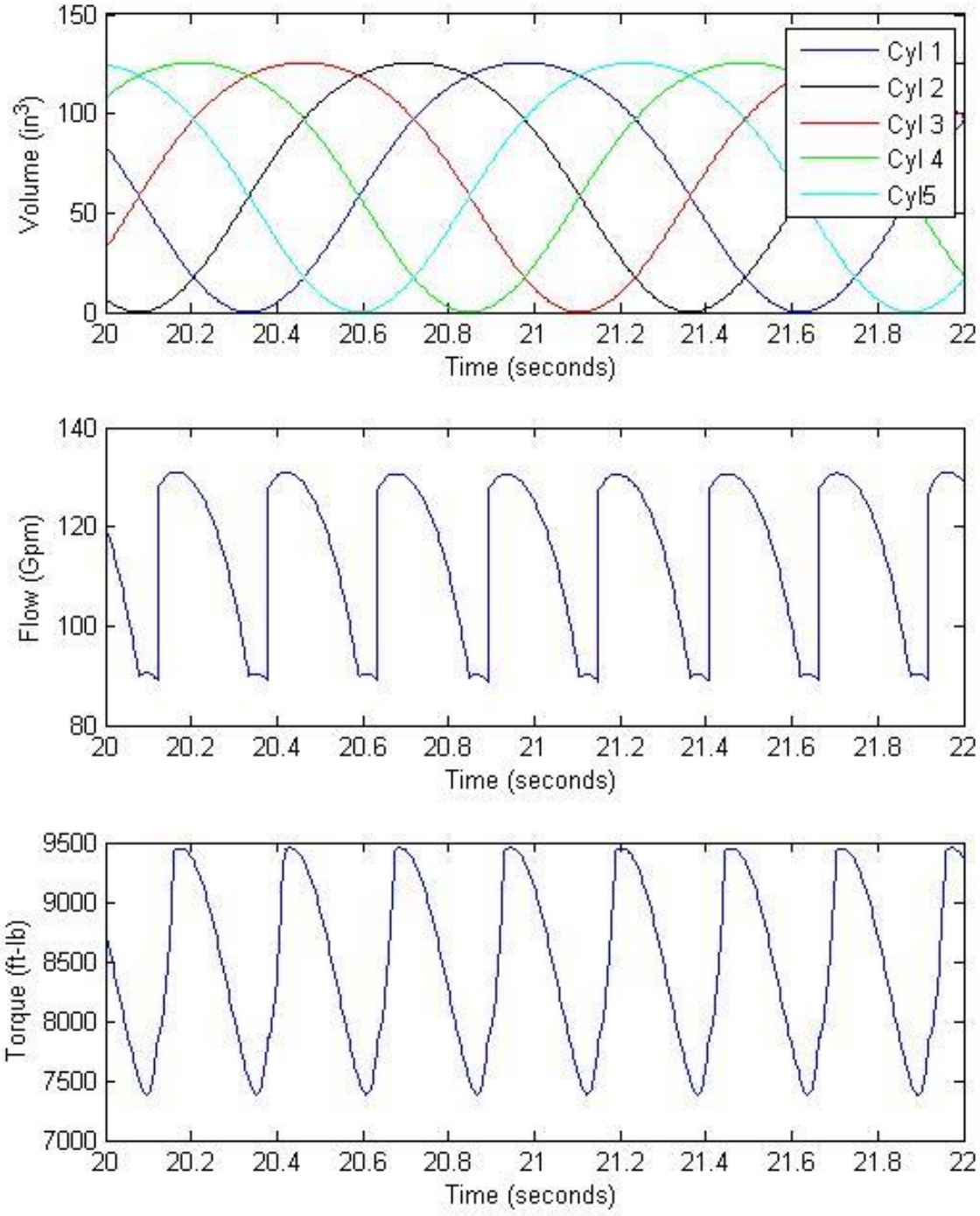

Figure 4-12: Cylinder volume, net outlet flowrate, and input torque of multi cylinder pump operating at constant speed against 12000 psi outlet pressure

4.2 Assembled Driveline

The assembled drive line model is shown in Figure 4-13. The commanded engine speed and gear number are provided as control signals (shown in green in the figure). The driveline components (shown in beige) from left to right are the natural gas engine model discussed in Part III, the locking torque converter, the simplified transmission, an inertia representing the transmission output shaft, and the multi cylinder pump. The pump is acting between a constant pressure source and sink (also shown in beige). Rotational sensors (shown in purple) are used to measure the speed of each of the rotating components and the torque flow between driveline components.

The lock up clutch logic subsystem is shown in Figure 4-14. It receives the commanded gear number as an input. When a change is detected in the input, the torque converter logic unlocks the torque converter to allow slip between the engine and the torque converter turbine. After a fixed amount of time passes, t_1, the clutch locks again. An initial state is included at the right of the subsystem which allows the user to start the simulation with the clutch locked or unlocked.

The gear ratio selector shown in Figure 4-15 also receives the commanded gear number as an input. When a change is detected in the gear number the selector passes the new gear ratio to the simplified transmission model. A Simulink selector block is used to select the gear ratio which corresponds to the commanded gear number.

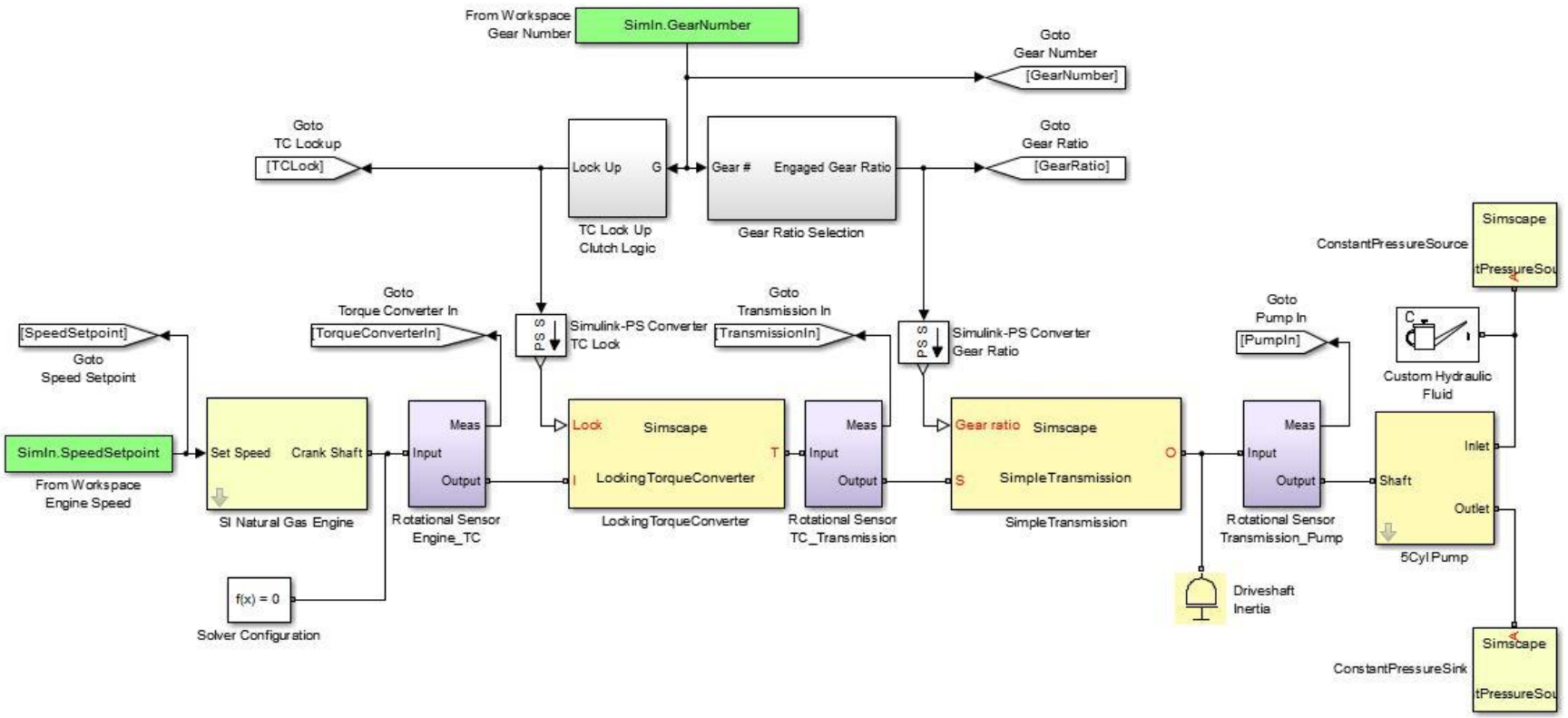

Figure 4-13: Assembled driveline model including (1) spark ignited lean burn mean value natural gas engine, (2) locking torque converter, (3) simplified transmission, (4) multi-cylinder hydraulic pump, (5) torque converter lock up clutch and gear selector logic

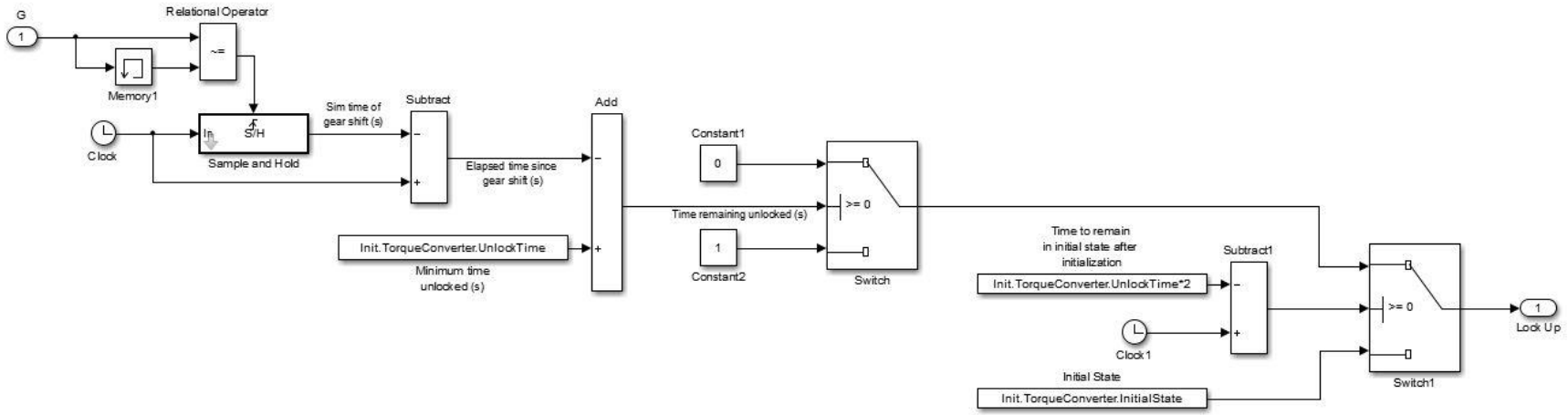

Figure 4-14: Torque converter lockup clutch logic

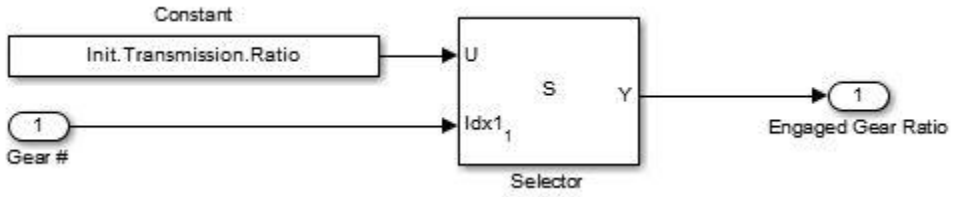

Figure 4-15: Gear ratio selection logic

4.3 Results

Shifting events representative of conditions encountered by diesel powered pumps in drilling operations are simulated using the assembled driveline model. Each event is simulated using both the natural gas engine model and the diesel engine model as a baseline for comparison. It should be noted that the natural gas engine controller gains have not been tuned to match experimental data, and therefore the simulation results shown are intended to only provide a general illustration.

During simulation of an upshift the commanded engine speed is gradually increased in order to increase the pump flow rate. When the engine approaches the maximum speed, 1950 rpm, the transmission is shifted to the next gear. By simultaneously reducing the commanded engine speed when the new gear is engaged, the rotational speed of the pump before and after the shift is maintained equal. To illustrate the challenge associated with the transient response of the natural gas engine, two upshifts are simulated at different pressures.

Figure 4-16 show the simulation results when pumping against a relatively low pressure of 3000 psi. The top subplot shows the commanded engine speed, and the simulated speed of the diesel and natural gas configurations. The bottom subplot shows the commanded gear number and the natural gas engine throttle position. During the shift the natural gas engine response is slightly slower than the diesel, but the engine is able to recover and continue driving the pump. The throttle closes slightly to slow the engine in preparation for the shift, and reopens after the new gear is engaged.

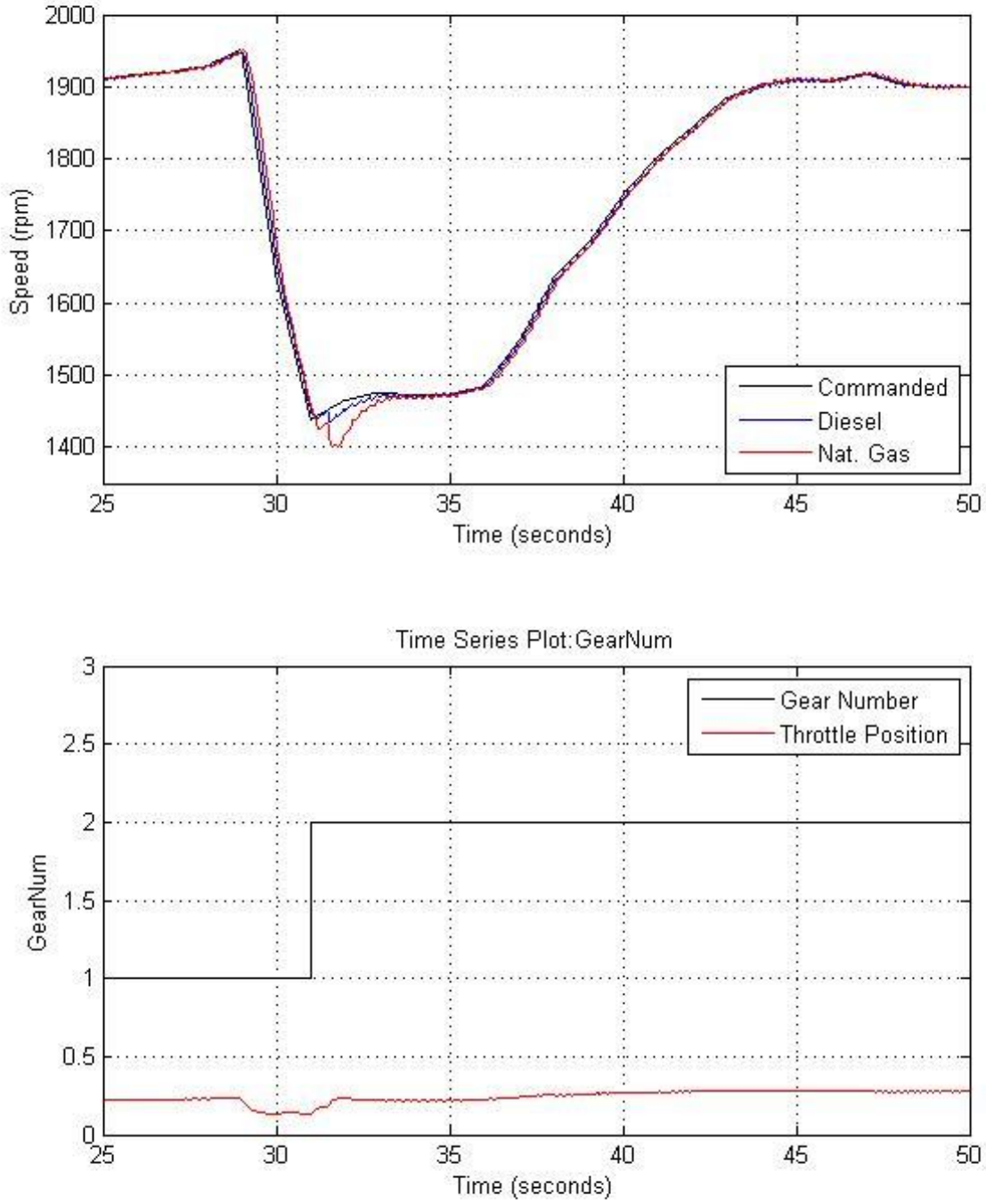

Figure 4-16: Simulation results during an upshift pumping against constant pressure of 3000psi. Commanded and simulated engine speeds, gear number and throttle position.

Figure 4-17 shows the shift in more detail. The commanded gear number increases at 31 seconds at which point the torque converter clutch is disengaged. The transmission engages the new gear at 31.5 seconds causing the engine speed to drop suddenly in both the diesel and natural gas simulations. The torque converter clutch is then closed at 32 seconds. The individual cylinders of the pump model generate torque on the driveline and result in the oscillations in engine speed.

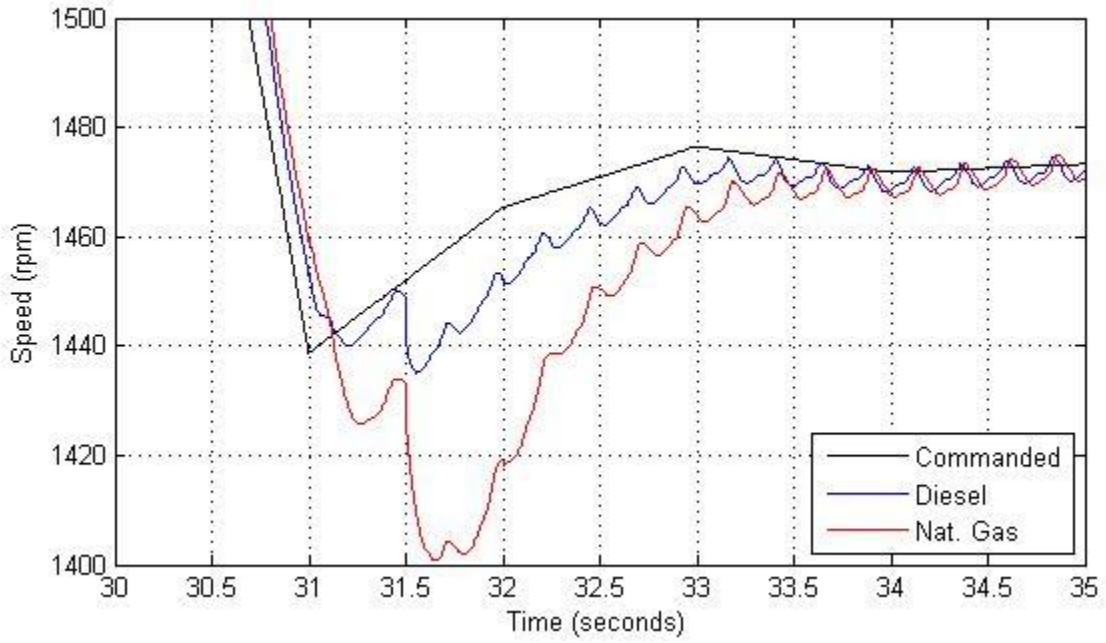

Figure 4-17: Commanded and simulated engine speeds during upshift pumping against constant pressure of 3000psi

Figure 4-18 shows the simulation results when pumping against a higher pressure of 12000 psi. The diesel engine accepts the load during the shift and follows the commanded speed trace well. As the natural gas engine speed decreases when the new gear is engaged, the throttle is opened fully. With the throttle wide open, the engine is unable to meet the torque requirements and the engine speed continues to decrease until coming to a full stop.

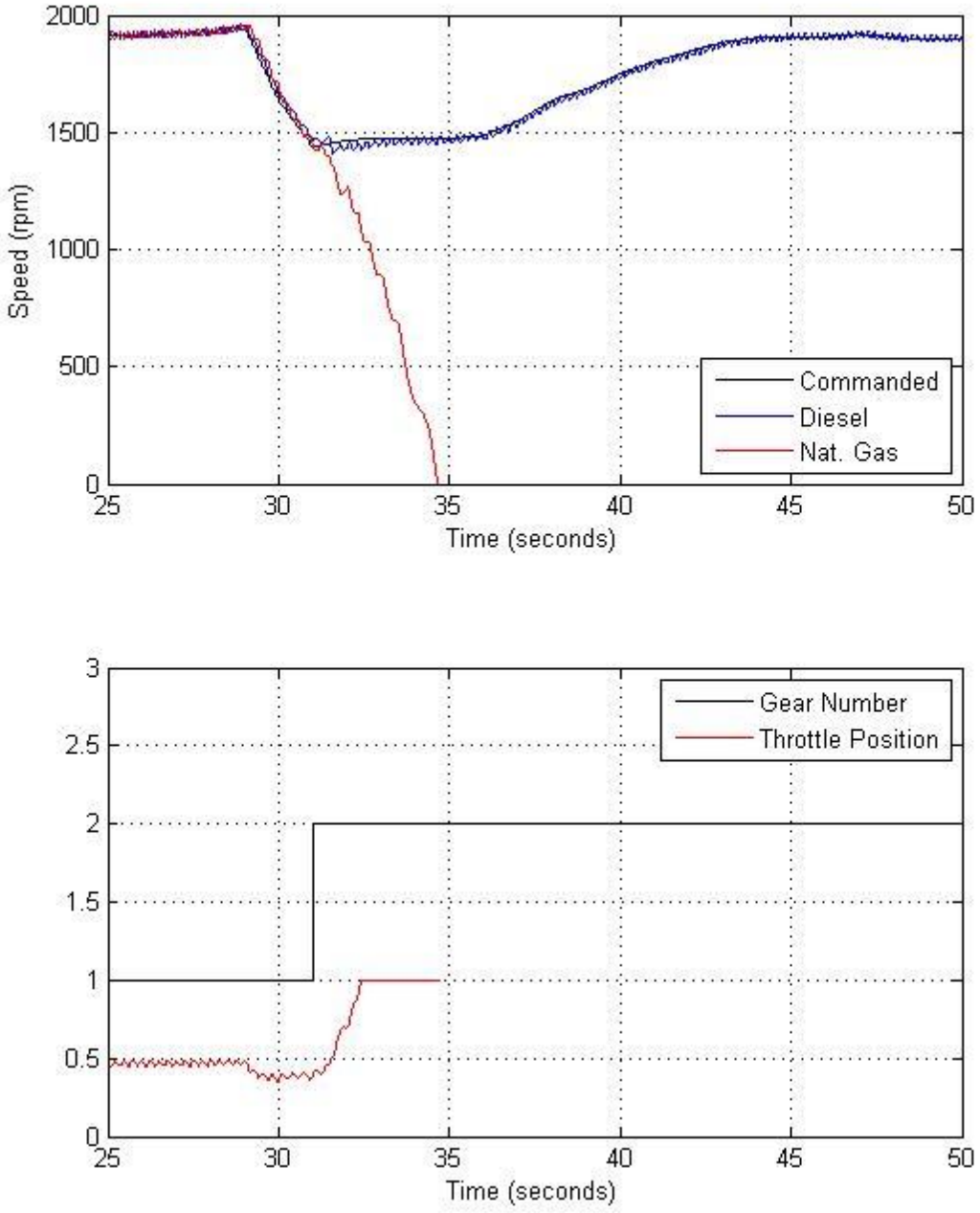

Figure 4-18: Commanded and simulated engine speeds during an upshift pumping against constant pressure of 12000psi.

4.4 Conclusions and Recommendations

This chapter developed component models for a torque converter, transmission, and pump used in hydraulic fracturing. The component models were validated individually against confidential data provided by Halliburton. The full driveline model was used to simulate shifting events encountered in hydraulic fracturing with both the diesel model discussed in Chapter 2, and the natural gas engine model discussed in Chapter 3 as the driver. The results suggest the direct substitution of a diesel engine with a natural gas engine of similar power is not a viable solution due to the poor capability of gas engines under transient loads. Although it is possible for the natural gas engine to recover after a shift under certain conditions, namely pumping against a low pressure, it is likely the engine will not recover when operating against pressures typical in this application. The model suggests this is largely a result of the sudden increase in torque applied to the engine when the torque converter clutch is engaged.

In order to use the natural gas engine in this application, without modification to the drivetrain system, a transient support system needs to be developed. Using the drivetrain and engine models presented in this dissertation, potential methods to improve the transient response of the natural gas engine can be investigated, including:

1) Incorporating an electric motor or other means to accelerate the turbocharger rotor in preparation for an anticipated transient event, as illustrated in Figure 4-19 and Figure 4-20, in order to increase the pressure at the compressor outlet and to sustain the air flow rate when the throttle is opened. This method would require little additional hardware, making it potentially cost-effective. The drawback of this solution is it relies on forecasted knowledge of an upcoming transient.

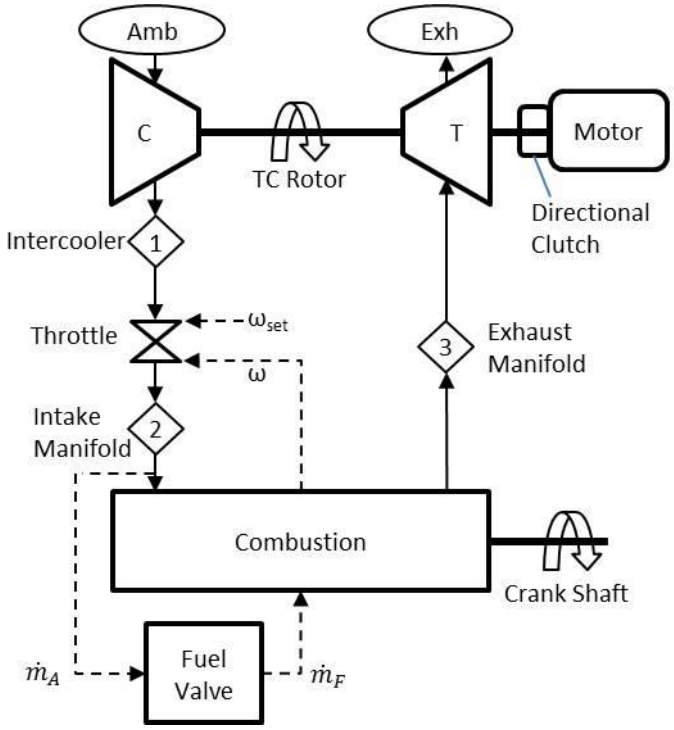

Figure 4-19: Schematic of turbocharger assist utilizing an electric motor and one way clutch to accelerate the turbocharger rotor in preparation for a transient

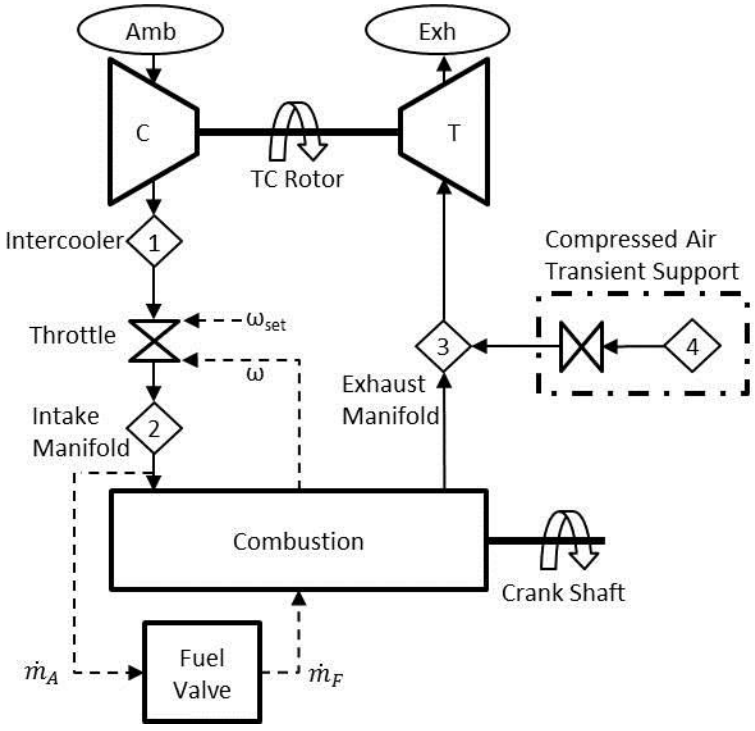

Figure 4-20: Schematic of turbocharger assist utilizing compressed air to accelerate the turbocharger rotor in preparation for a transient

2) Using compressed air from a high pressure storage tank to boost the intake manifold pressure during a transient event, assisting the turbocharger by providing a parallel pressurized air source. As in (1), this method also would require little additional hardware, making it cost effective. It also has the potential to operate rapidly and reactively, without the requiring a forecast of the transient. If the air storage tank is large enough, this method has the potential to sustain the engine operation for a significant duration, allowing the turbocharger time to accelerate and provide the required air.

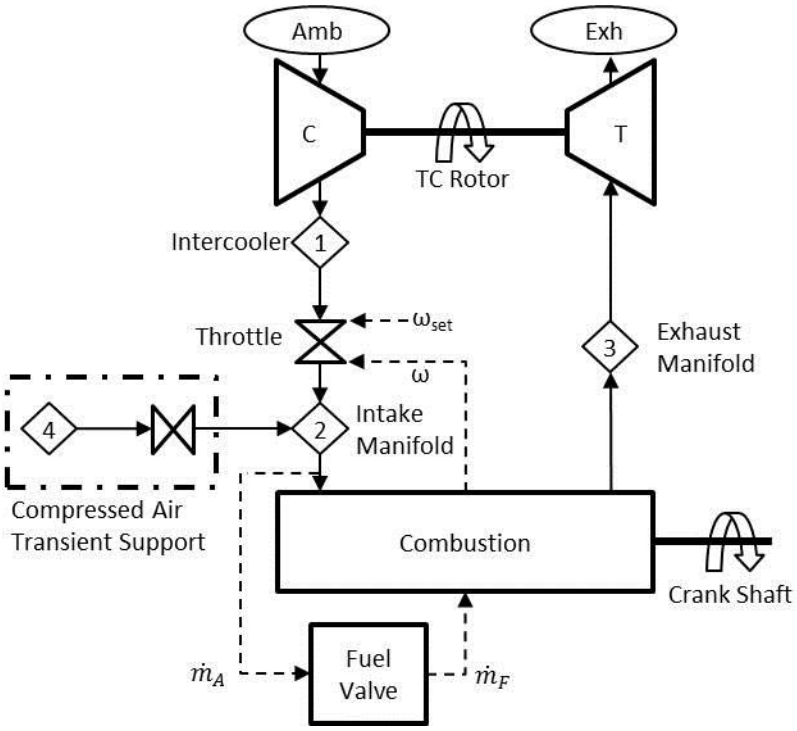

Figure 4-21: Schematic of transient support utilizing compressed air to boost and maintain intake manifold pressure during transient event

Other methods to enable the use of a natural gas engine in this application involve substantial re-design of the drivetrain system. Potential methods include:

1) Complete redesign of the transmission and torque converter to better match the torque requirements in this application. The purpose of torque converters in many applications is to

provide a torque multiplication, while also decoupling the rotational speed of the input and output. The sudden torque applied to the engine by closing the lock up clutch when the driveline is nearly stopped could be reduced by designing a torque converter sized for this application, rather than adapting an existing design from another system.

2) Using an electric storage system and motor in parallel with the engine to power the drivetrain as illustrated in Figure 4-22, primarily to absorb transient loads and allow the engine to operate in a steadier manner. This method however would require a significant amount of hardware including a high power motor and high capacity storage system. Due to the nature of the industry the engine-drivetrain-pump system is typically skid mounted and subject to size and weight restrictions of over the road tractor trailers. Limited space at drilling sites also restricts the number of trailers that can be on location, making multi-trailer solutions unrealistic. Together, these constraints make this solution impractical.

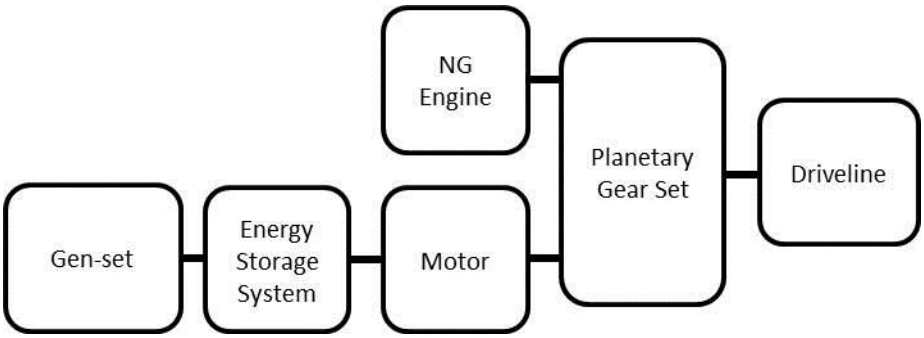

Figure 4-22: Transient support using on-site generator, electric energy storage system and planetary transmission

3) Using the engine to drive an electric generator which provides power to a load bank and an electric motor which powers the drivetrain as illustrated in Figure 4-23. The load bank is used to allow the engine to operate more steadily by providing a buffer during the transients. Operating the engine at higher power than required and dissipating a portion of the generated

power through the load bank in order to allow transients to be smoothed acts to counter the efficiency and fuel savings benefits of using a dedicated natural gas engines. As in the previous solution, the significant amount of added hardware required makes meeting the size and weight restrictions difficult. In addition the cost associated with electric machines and equipment is a drawback of this solution.

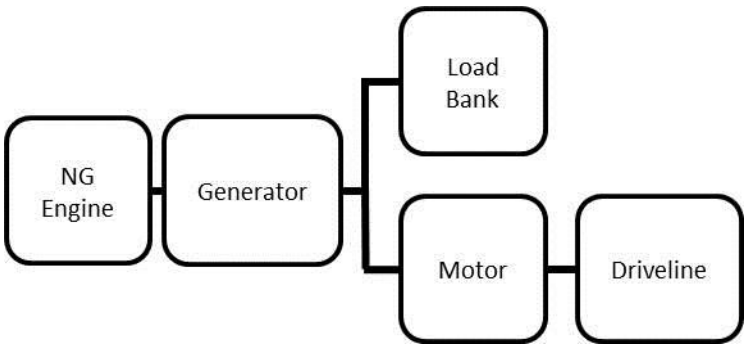

Figure 4-23: Transient support using electric generator, motor and load bank

Lastly, a pressure relief mechanism downstream of the pump could be incorporated to remove the load during a shift. This could allow the drivetrain to operate in a more conventional manner, and potentially eliminate the transient resulting from closing the torque converter clutch after the new gear is engaged.

5 Scalable Turbocharger Performance Maps for State-Based Engine Models

Compressor and turbine performance is typically implemented in dynamic state-based engine models such as those developed in [30] [31] [29] and used for power system studies as in [41] [17] as look-up tables or curve fits developed from performance maps, however a significant amount of effort is required to convert the data to a form suitable for simulation. Manufacturers frequently only provide data on the maps around the region of high efficiency where the turbocharger is operating at high speeds and pressure ratios near the surge margin. The performance at low rotor speeds and low pressure ratios, a region frequently encountered during simulation at low engine load, must be extrapolated from the available data as illustrated by [32] and discussed in [42]. Additionally, at compressor surge the mass flow rate through the compressor drops suddenly and can even experience a flow reversal, creating stiff state equations. This region of the map is difficult to capture using a lookup table which is indexed by pressure ratio and corrected rotor speed; the output is undefined for inputs above the surge line and it is difficult to capture the compressor surge well in the fits produced by the methods discussed in [32].

Collecting performance data specific to a particular compressor and turbine, and generating curve fits which accurately capture the characteristics of the data often requires a significant amount of time and effort. In order to model several engines ranging in displacement and power the process must be repeated for each engine. A scalable approach to modeling the turbocharger would streamline this process, but has not been presented in literature. The approach introduced in this paper utilizes dimensional analysis techniques, often used in the design of compressors and turbines, to generate a suitable map once, and then adapt that map for use in simulation

across a range of engine sizes. The process reduces the amount of data and effort required to model a series of engines.

The remainder of this paper is divided into 3 sections. Section 2 briefly reviews methods to fit performance data and extrapolate into the low rotor speed, low pressure ratio regions of a compressor map. An approach to scaling a compressor map using the dimensional analysis similar to that presented in [34] to produce maps for geometrically similar compressors is then illustrated. The compressor data is normalized by the surge line to produce a rectangular lookup table which (a) is readily implemented in simulation, and (b) captures rapid change in mass flow near the surge line. A similar scaling approach is applied to normalize the turbine map. Section 3 introduces a method to select a compressor diameter to match the non-dimensional map to a given engine and to select a turbine diameter which will match the compressor torque requirements. Finally a set of compressor and turbine maps are scaled to match several engine sizes in section 4 in order to illustrate the utility of the method.

5.1 Scalable Modeling Approach

5.1.1 Review of Fitting Methods

Steady state compressor mass flow and isentropic efficiency data collected at selected rotor speeds and pressure ratios is typically available from the manufacturer as a table or map similar to that shown in Figure 5-1. Given the pressure ratio across the compressor and the corrected rotor speed, the data can be used to determine the corrected mass flow rate, $\dot{m}_{corr,C} = f\left(N_{corr}, \frac{P_d}{P_u}\right)$, and the isentropic compressor efficiency, $\eta_c = f\left(N_{corr}, \frac{P_d}{P_u}\right)$. The corrected rotor speed, N_{corr}, and corrected mass flow are used to account for temperature and pressure effects of the upstream air [43] [35] using equations (49) and (50).

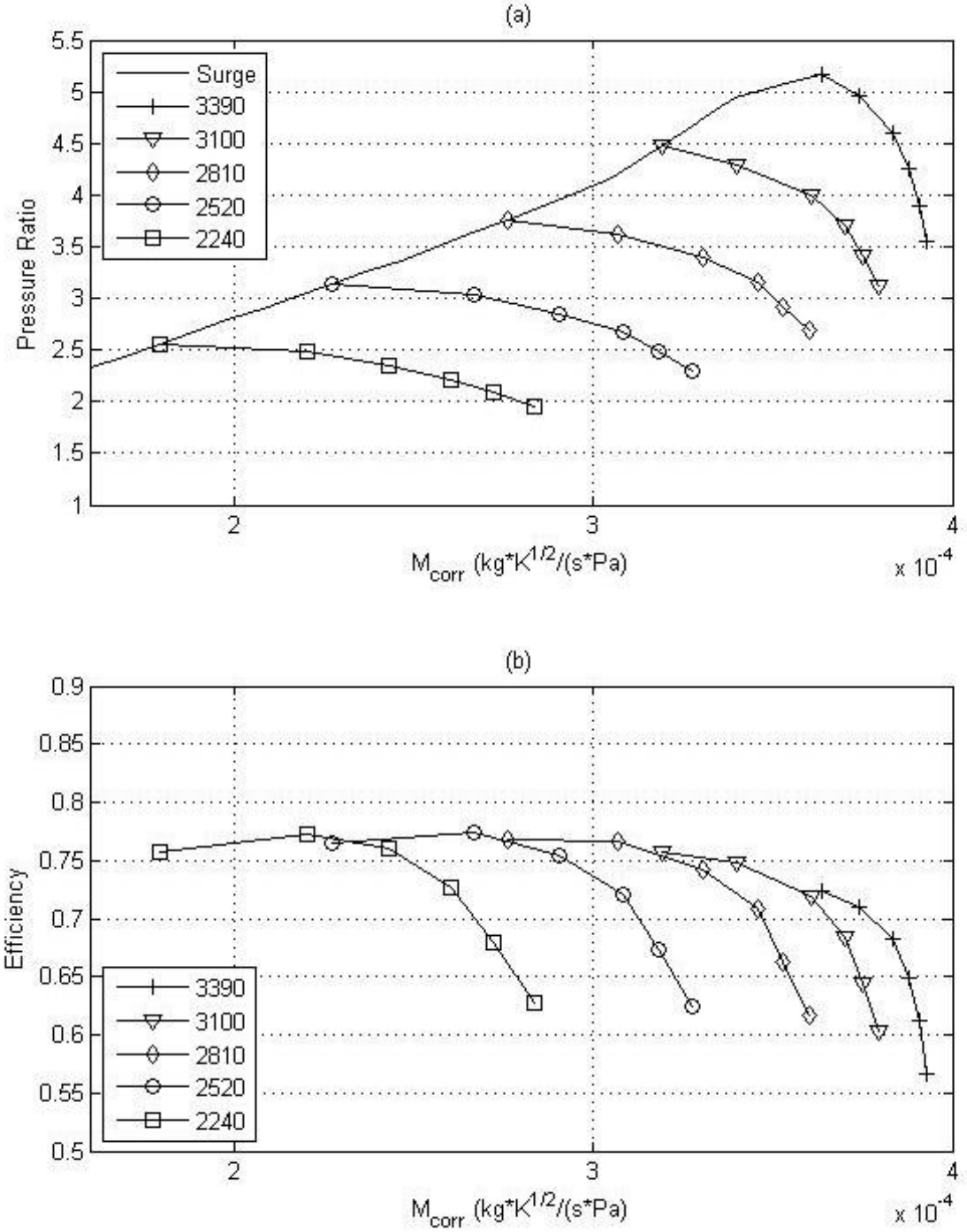

Figure 5-1: Compressor data typically available by request from manufacturer illustrated as (a) corrected mass flow as a function of pressure ratio and corrected rotor speed, and (b) isentropic compressor efficiency as a function of corrected rotor speed and corrected mass flow rate. The compressor shown has a rotor diameter of 189mm.

$$\dot{m}_{corr,C} = \frac{\dot{m}_C \sqrt{T_u}}{P_u} \tag{49}$$

$$\mathrm{N_{corr}} = \frac{N_{TC}}{\sqrt{T_u}} \tag{50}$$

The tabular data is not well-suited for simulation since it (a) is limited to few data points representing non-linear performance characteristics of the compressor and turbine which would introduce significant error when used with linear interpolation and extrapolation techniques, (b) does not illustrate the performance at low rotor speed and low pressure ratios, a region frequently encountered in simulations during initialization or where the engine is operating across a range of speed and load, and (c) includes an region above compressor surge where the outputs ($\dot{m}_{corr,C}, \eta_c$) are undefined for inputs ($N_{corr}, \frac{P_d}{P_u}$) . For these reasons curve fits are often used in simulation models. Four methods of curve fitting compressor and data are reviewed and illustrated by [32] in order to extrapolate performance to low pressure ratios and low rotor speeds. The four methods illustrated are:

1) The Jensen & Kristensen method [44] which expresses the dimensionless head parameter and the compressor efficiency as functions of normalized flow rate and inlet Mach number. Coefficients for the expressions are determined using a least-squares fit to experimental data.

2) The Mueller method [45] which models the dimensionless head parameter as a quadratic function of normalized compressor flow rate.

3) The zero slope line method [32] which describes the compressor flow parameter as a function of pressure ratio and the corrected rotor speed. The fit is divided into a linear region and an exponential region by the zero-slope line which connects the maximum mass flow of each speed line.

4) A neural network as used by [46], and determined to be ill-suited to compressor modeling due to the large number of required coefficients and the limited number of data points available to train the neural network.

Steady state turbine mass flow and isentropic efficiency data collected at selected rotor speeds and pressure ratios are also typically available from the manufacturer as a table or map similar to that shown in Figure 5-2. Given the expansion ratio across the turbine and the corrected rotor speed, the data can be used to determine the corrected mass flow rate, $\dot{m}_{corr,T} = f\left(N_{corr}, \frac{P_u}{P_d}\right)$, and the isentropic compressor efficiency, $\eta_T = f\left(N_{corr}, \frac{P_u}{P_d}\right)$. Methods to curve fit turbine mass flow and efficiency data are also presented by [32]. All of these methods require a significant amount of experimental data, as well as effort and judgement to process each map. In order to reduce the amount of time and effort required to implement a turbocharger model into simulations of various engine scales and applications, a scalable approach using a "generic" map is desirable.

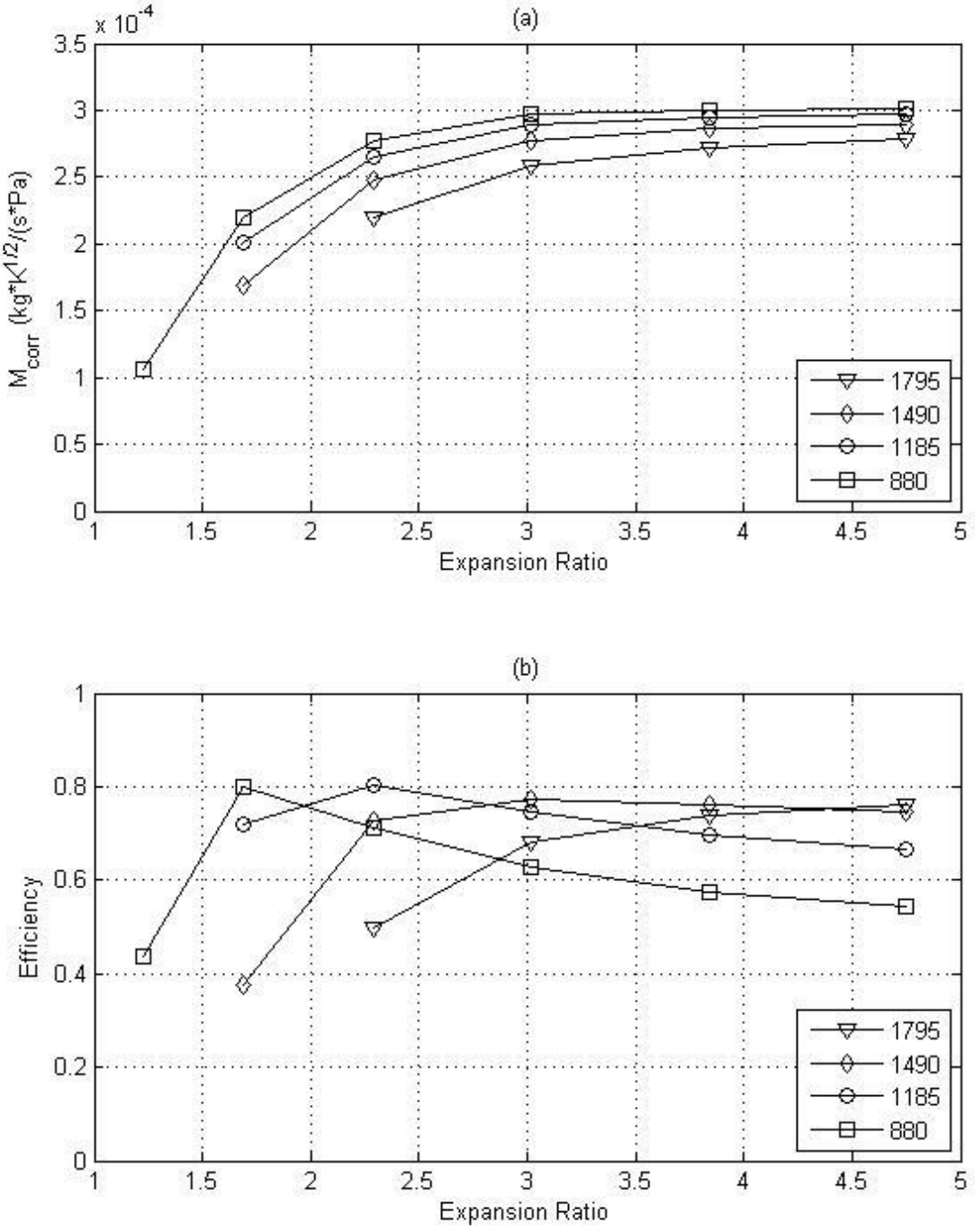

Figure 5-2: Turbine data typically available by request from manufacturer. (a) Corrected mass flow as a function of expansion ratio and corrected rotor speed. (b) Isentropic compressor efficiency as a function of expansion ratio and corrected rotor speed. The turbine shown has a rotor diameter of 177 mm.

5.1.2 Proposed Scaling Method – Compressor

Turbocharger designers use maps in terms of non-dimensional terms to approximate the performance of new compressor sizes from similar compressors before producing a prototype [34]. If the diameter of the compressor wheel, D_c, is known the corrected mass flow rate and efficiency data can easily be converted to non-dimensional compressor mass flow coefficient, $\emptyset_C$, and Mach number based on the rotor tip speed, $c_{0,C}$.

$$\emptyset_C = \dot{m}_{corr,C} \frac{\sqrt{R}}{D_c^2} \tag{51}$$

$$c_{0,C} = \left(\frac{2\pi}{60}\right) N_{corr} \frac{D_c}{\sqrt{\gamma R}} \tag{52}$$

Manufacturers typically present data in terms of corrected rotor speed and corrected mass flow rate rather than these non-dimensional parameters because the map is presented for a particular selection of rotor ($D_c = constant$) and it is assumed the compressor will always handle air near standard temperature and pressure ($R = R_{air}$, $\gamma = \gamma_{air}|_{STP}$).

Maps implemented in terms of the compressor mass flow coefficient and the rotor tip Mach number represent a family of similar compressors rather than a single design. Figure 5-3 shows a compressor map in terms of the non-dimensional parameters developed from data presented in Figure 5-1. The data was first fit using the zero-slope line method and extrapolated into the low rotor speed, low pressure ratio region. The map in Figure 5-4 is generated from the non-dimensional map by selecting a new diameter, $D_c = 100$mm (smaller than the original rotor). By selecting a diameter, $D_c = 200$mm (larger than the original diameter) the map in Figure 5-5 is produced. The dimensional analysis presented by [34] suggests these maps represent

geometrically similar compressors where the pitch-chord ratio, s/l, and the aspect ratio, h/l, remain constant within the family.

From equations (51) and (52) it is easy to see the mass flow rate is proportional to the square of the rotor diameter, and the rotor speed is inversely proportional to the rotor diameter. By selecting a smaller diameter the rotational speed of the rotor is increased and the corrected mass flow rate is reduced as illustrated in Figure 5-4. By selecting a larger diameter the rotor speeds are reduced and the mass flow rate is increased as shown in Figure 5-5.

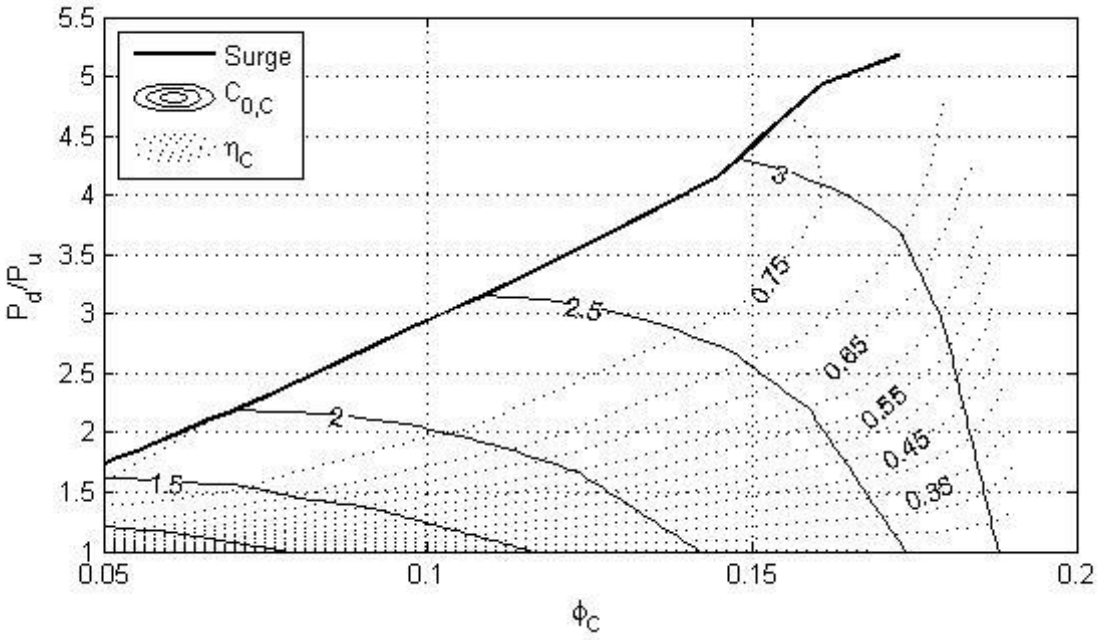

Figure 5-3: Compressor map developed from data in Figure 5-1 converted to non-dimensional mass flow coefficient and rotor tip Mach number, and extrapolated to low rotor speed and pressure ratio regions.

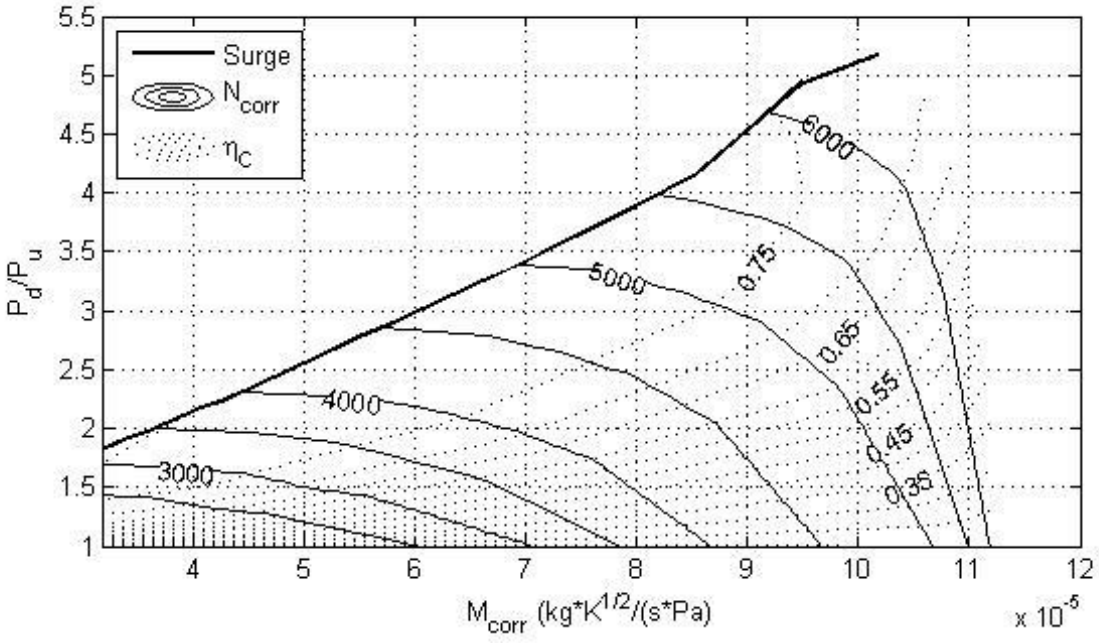

Figure 5-4: Compressor map in terms of corrected rotor speed and corrected mass flow rate developed from non-dimensional map scaled down to a rotor diameter = 100mm.

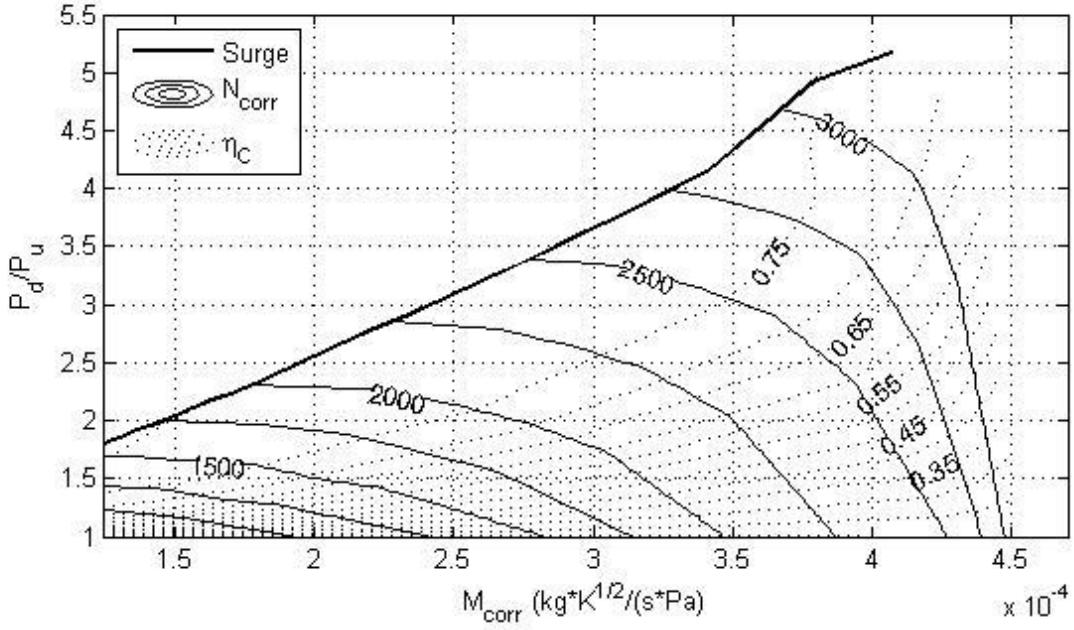

Figure 5-5: Compressor map in terms of corrected rotor speed and corrected mass flow rate developed from non-dimensional map scaled up to a rotor diameter = 200mm.

5.1.3 Compressor Performance as Lookup Tables

Lookup tables generally are not used for turbocharger data because linear interpolation methods results in significant error, particularly in regions with low resolution data or significant non-linearity [32] [44] [45]. Lookup tables however are readily implemented in simulations and are computationally efficient. By first fitting the data using one of the methods from section 5.1.1, the curve fit can be evaluated to create a lookup table at a higher resolution (using smaller steps in pressure ratio and rotor speed) than the data provided by manufacturer. This method reduces the error associated with interpolation within the table data.

At the surge line the compressor stalls and mass flow stops or may reverse flow. The region of the map above the surge line is typically not communicated by the manufacture, which makes it difficult to implement the data as lookup tables indexed by pressure ratio and rotor speed (either corrected rotor speed or rotor tip Mach number). The challenge is twofold: First, in the surge region a lookup table would have combinations of inputs $(\frac{P_d}{P_u}, c_{0,C})$ where the outputs $(\emptyset_C, \eta_c)$ are undefined. This region cannot be avoided during dynamic simulation due to events such as a sudden change in speed and/or load, and results in undefined behavior, where there is no counteracting "force" to push the simulation back onto the map. Second, for a lookup table of practical size (or a curve fit of practical order) it is difficult to represent the sudden change in output parameters near the surge line. Therefore, the simulation can easily jump over this boundary and get stuck in the undefined area above the surge line.

The pressure ratio at compressor surge is found for a given rotor speed $\left(\frac{P_d}{P_u}\right)_{surge} = f(N_{corr})$, or rotor tip Mach number $\left(\frac{P_d}{P_u}\right)_{surge} = f(c_{0,C})$. The pressure ratios corresponding to efficiency and mass flow data at that rotor speed are then normalized by the pressure ratio at surge as:

$$P_{idx} = \frac{\left(\frac{P_d}{P_u}\right) - 1}{\left(\frac{P_d}{P_u}\right)_{surge} - 1} \tag{53}$$

By normalizing the pressure ratio by the surge line, a rectangular lookup table is produced, indexed by a surge normalized pressure ratio index, P_{idx}, instead of the pressure ratio, $\left(\frac{P_d}{P_u}\right)$. This process effectively maps the region below the surge line onto rectilinear axes as illustrated in Figure 5-6. Using this index, there is no longer a region above compressor surge in the data where the outputs are undefined. The new pressure index ranges from $P_{idx} = 0$ where there is no boost across the compressor, $\left(\frac{P_d}{P_u}\right) = 1$, to $P_{idx} = 1$ at compressor surge, $\left(\frac{P_d}{P_u}\right) = \left(\frac{P_d}{P_u}\right)_{surge}$, where the flow quickly rolls off to zero. The high resolution lookup table created by this process can be used for a range of engine sizes.

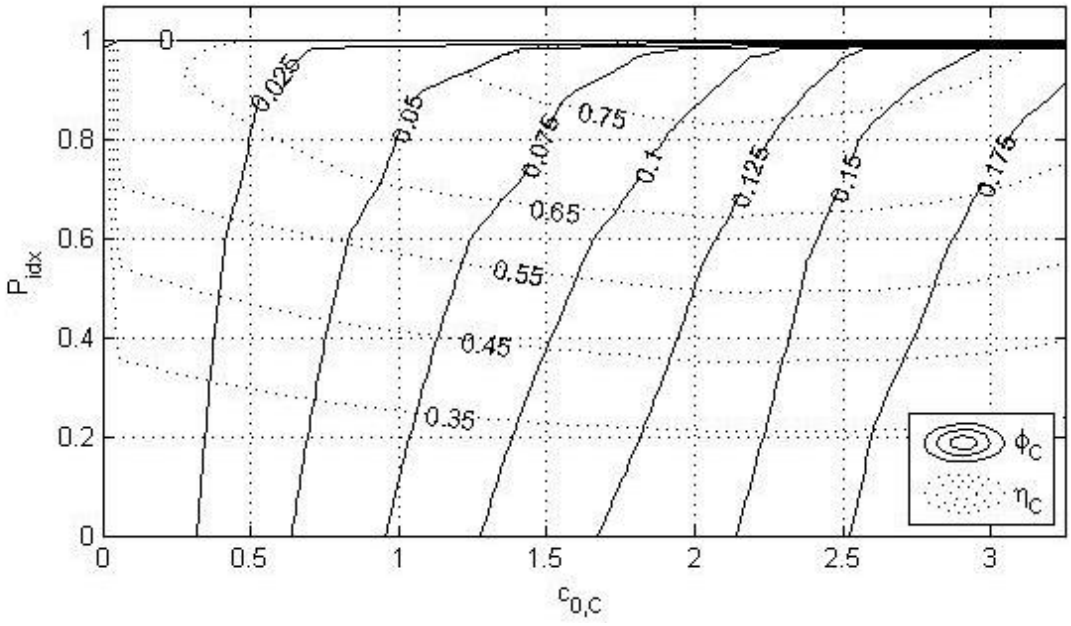

Figure 5-6: Compressor map normalized by pressure ratio at compressor surge, resulting in a rectangular lookup table easily implemented in a simulation. While rectangular, near the surge line ($P_{idx} = 1$) the map changes rapidly, and needs to be implemented using a sufficient number of data points, interpolated from the original data as described in the text.

5.1.4 Proposed Scaling Method – Turbine

An approach similar to that used for the compressor data in section 5.1.2 can be applied to the turbine data. If the diameter of the turbine wheel, D_T, is known the data can easily be converted to the non-dimensional parameters. The turbine mass flow coefficient, $\emptyset_T$, and Mach number based on the rotor tip speed, $c_{0,T}$, are calculated as:

$$\emptyset_T = \dot{m}_{corr,T} \frac{\sqrt{R}}{D_T^2} \tag{54}$$

$$c_{0,T} = \left(\frac{2\pi}{60}\right) N_{corr} \frac{D_T}{\sqrt{\gamma R}} \tag{55}$$

Again, manufacturers typically present the data as in Figure 5-2 in terms of corrected rotor speed, $\mathrm{N_{corr}} = \frac{N_{TC}}{\sqrt{T_u}}$, and corrected mass flow rate, $\dot{m}_{corr,T} = \frac{\dot{m}_T \sqrt{T_u}}{P_u}$, rather than these non-dimensional parameters, for similar reasons. Figure 5-7 shows the turbine efficiency and non-dimensional mass flow coefficient presented in terms of the expansion ratio, P_u/P_d, and rotor tip Mach number. The expansion ratio and rotor tip Mach number form rectilinear axis for the turbine data, allowing a lookup table to easily be implemented. Notice at high expansion ratios the mass flow map becomes very flat representing choked flow conditions across the turbine. The data was first fit using techniques in [42] and extrapolated into the low rotor speed, low pressure ratio region, then normalized using equations (54) and (55).

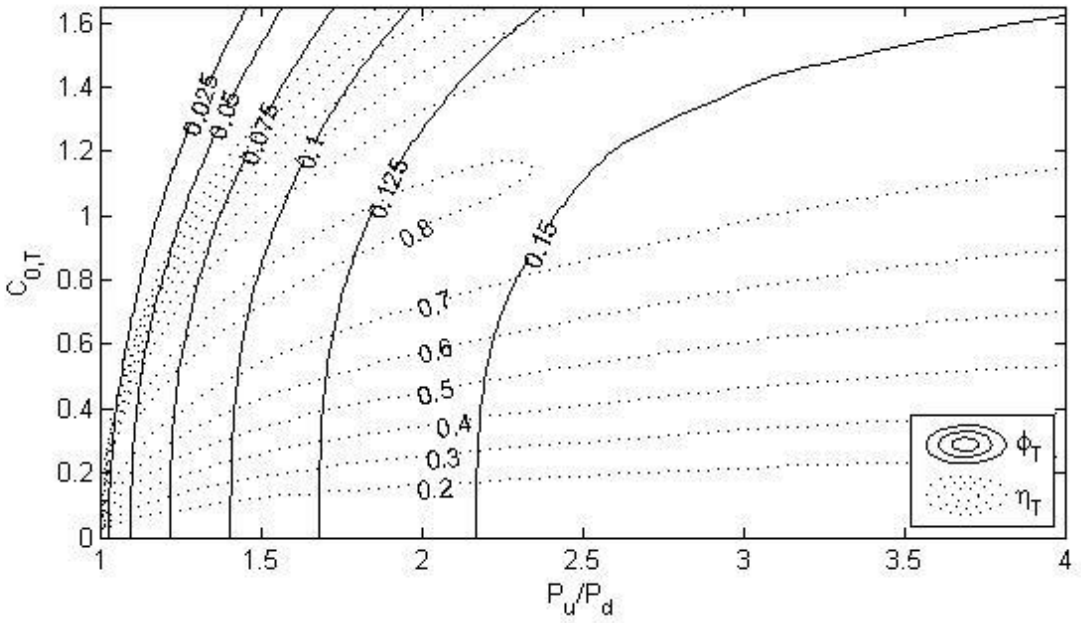

Figure 5-7: Turbine non-dimensional mass flow coefficient and efficiency map.

5.2 Turbocharger Selection using Non-Dimensional Maps

Implementing performance maps in terms of the non-dimensional parameters allows a single set of maps to approximate the turbocharger performance for a range of engine sizes by adjusting the compressor and turbine diameters to match the target brake power and air-fuel ratio of each engine. A single set of non-dimensional maps can be utilized in the series of engine models instead of repeating the process of finding the device-specific compressor and turbine maps, fitting the data to extrapolate into the region of low pressure and low rotor speed, and converting the maps to a tabular data format at a higher resolution than provided by the manufacturer. A process to match the non-dimensional compressor and turbine maps to a given engine is illustrated below.

5.2.1 Selecting Compressor Diameter

The air mass flow rate required to meet a target engine power, $\dot{W}$, and target air-fuel ratio, R_{A-F}, for an given engine can be approximated as:

$$\dot{m}_{air} = \frac{\dot{W} R_{A-F}}{\eta_{\mathrm{Th}} E_{LHV}} \tag{56}$$

where η_{Th} is the approximate thermal efficiency of the engine and E_{LHV} is the lower heating value of the fuel.

The intake manifold pressure, P_m, required to meet this air flow rate in a four stroke engine can then be approximated assuming an ideal gas following the speed-density equation as:

$$P_m = \frac{120 \dot{m}_{air} R T_m}{\eta_{\mathrm{V}} N V_d} \tag{57}$$

where T_m is the intake manifold temperature, η_{V} is the volumetric efficiency of the engine, N is the engine speed, and V_d is the displacement of the engine.

Assuming a small pressure loss across the air filter, P_{loss1}, and across the aftercooler, P_{loss2}, the pressure ratio across the compressor can be determined as:

$$\left(\frac{P_d}{P_u}\right)_{Req} = \frac{P_m + P_{loss2}}{P_{atm} - P_{loss1}} \tag{58}$$

where , $P_{atm}$is the atmospheric pressure.

Referring to the non-dimensional map, the required pressure ratio can be found in the region of high efficiency and the required compressor mass flow coefficient, $\emptyset_{C\,Req}$, can be read as illustrated in Figure 5-8.

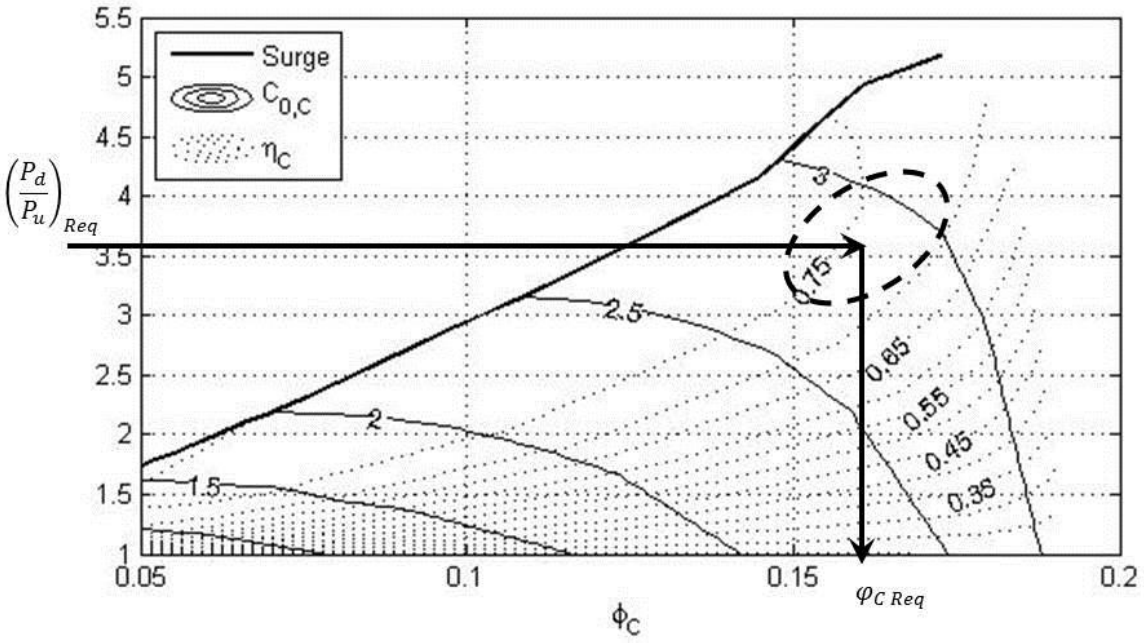

Figure 5-8: Using the required pressure ratio to determine the required mass flow coefficient to be in the high efficiency region of the compressor map leaving a surge margin.

The diameter of the compressor wheel can be calculated by combining equations (49) and (51), substituting T_{atm} for T_u, $(P_{atm} - P_{loss1})$ for P_u, and $\dot{m}_{air}/N_{TC}$ for $\dot{m}_C$, where N_{TC} has been introduced to divide the air flow among parallel turbochargers.

$$D_C = \sqrt{\frac{\dot{m}_{air}\sqrt{RT_{amb}}}{N_{TC}\emptyset_{C\ Req}(P_{atm}-P_{loss1})}} \tag{59}$$

This diameter will match the normalized compressor map to the given engine.

The torque required to drive the compressor, τ_C, will be required to match the turbine in section 5.2.2 and can be calculated from isentropic relations as

$$\tau_C = \frac{\dot{m}_c C_p T_u}{N_{TC}\eta_c\omega_{TC}}\left(\left(\frac{P_d}{P_u}\right)^{\frac{\gamma-1}{\gamma}} - 1\right) \tag{60}$$

5.2.2 Selecting Turbine Diameter

The turbine diameter must be approximated to match the torque produced by the turbine to that required by the compressor during operation, $\tau_T = \tau_C$. The mass flow rate through the turbine can be calculated from the compressor mass flow and the air fuel ratio as $\dot{m}_T = \dot{m}_c \left(1 + \frac{1}{R_{A-F}}\right)$. The isentropic relation for turbine torque is:

$$\tau_T = \frac{\eta_T \dot{m}_T C_p T_u}{N_{TC} \omega_{TC}} \left(1 - \left(\frac{P_d}{P_u}\right)^{\frac{\gamma-1}{\gamma}}\right) \tag{61}$$

The lookup tables provide a relationship between the mass flow coefficient, efficiency, rotor tip Mach number and expansion ratio.

$$\emptyset_T = f\left(\frac{P_u}{P_d}, C_{0,T}\right) \tag{62}$$

$$\eta_T = f\left(\frac{P_u}{P_d}, C_{0,T}\right) \tag{63}$$

The definition of the rotor tip Mach number and the Mass flow coefficient provide two more equations with relation to the diameter.

$$\emptyset_T = \frac{\dot{m}_T \sqrt{R T_u}}{P_u D_T^2} \tag{64}$$

$$c_{0,T} = \frac{\omega_{TC} D_T}{\sqrt{\gamma R T_u}} \tag{65}$$

Assuming the temperature of the exhaust gas up stream of the turbine, T_u, is known and the turbine outlet pressure, P_d, is near ambient, equations (61) – (65) provide a set of 5 equations and 5 unknowns (η_T, P_u, $\emptyset_T$, $c_{0,T}$, D_T) which are solved for the turbine rotor diameter.

5.3 Results – Matching Non-Dimensional Maps to Four Diesel Engines

To illustrate the utility of the non-dimensional approach, compressor and turbine wheel diameters are selected to match the non-dimensional maps presented in Figure 5-6 and Figure 5-7 to several engines of various sizes. Table 5-1 summarizes the power and displacement of each engine, and the compressor and turbine diameters calculated to meet the power requirements.

Table 5-1: Compressor and turbine diameters calculated to match non-dimensional maps to four diesel engines utilized in power generation

Engine	$\dot{W}$ (kW)	V_d (l)	D_C (m)	D_T (m)
1	507	15.0	0.082	0.061
2	1470	50.3	0.149	0.112
3	1975	60.2	0.163	0.120
4	2515	77.6	0.186	0.139

Steady states corresponding to 20%, 40%, 60%, 80%, and 100% load were then simulated using each model. The compressor performance was monitored during simulation and is plotted on the normalized compressor maps in Figure 5-9 and Figure 5-10. At each load, each engine operates in nearly the same location on the normalized map. The turbine performance during simulation is also presented in Figure 5-11. Again at each load, each engine operates in nearly the same location on the normalized turbine map to balance the compressor torque. The clusters of simulated points correspond to increasing loads from left to right in each figure.

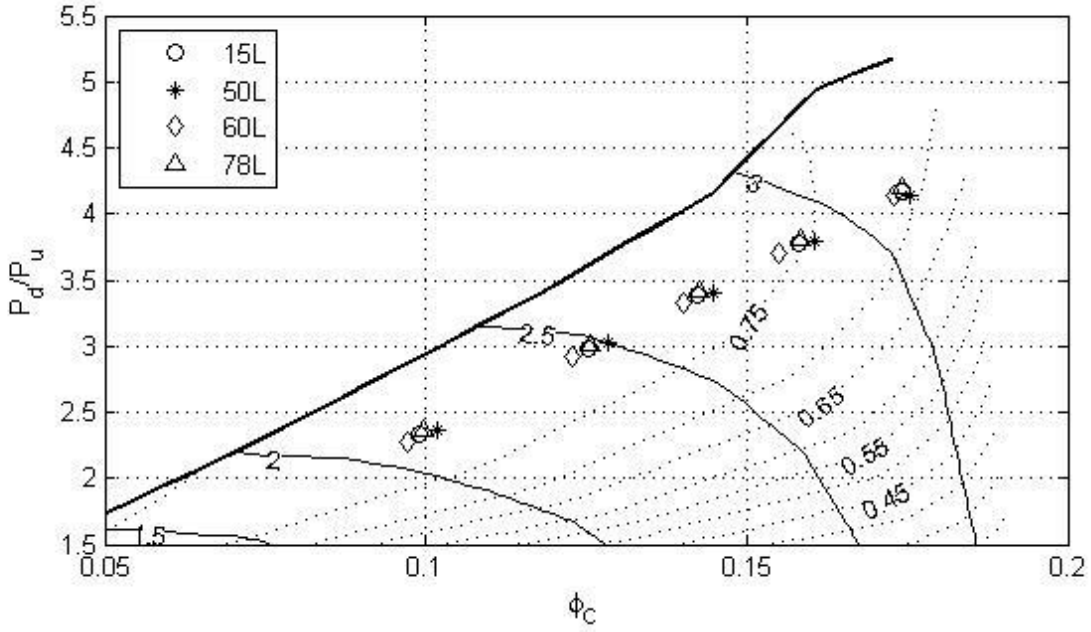

Figure 5-9: Compressor operation during simulation overlaid on no-dimensional compressor map. At each load, each engine operates at nearly the same point on the map. Clusters of points from left to right correspond to 20%, 40%, 60%, 80%, and 100% engine load.

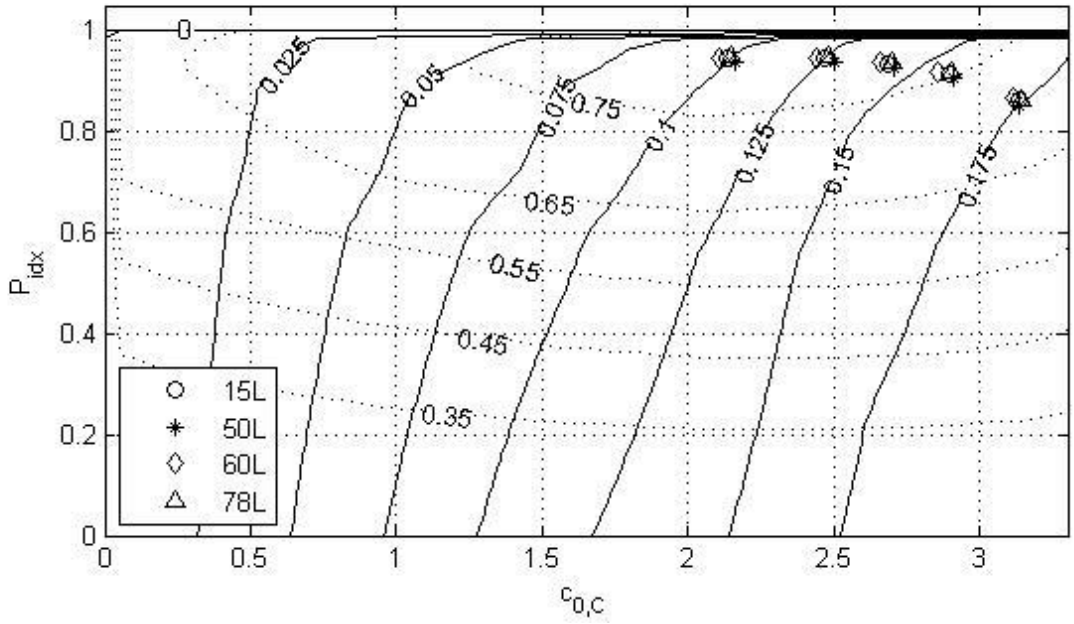

Figure 5-10: Compressor operation during simulation overlaid on surge normalized compressor map. Each engine operates at nearly the same point on the map. Clusters of points from left to right correspond to 20%, 40%, 60%, 80%, and 100% engine load.

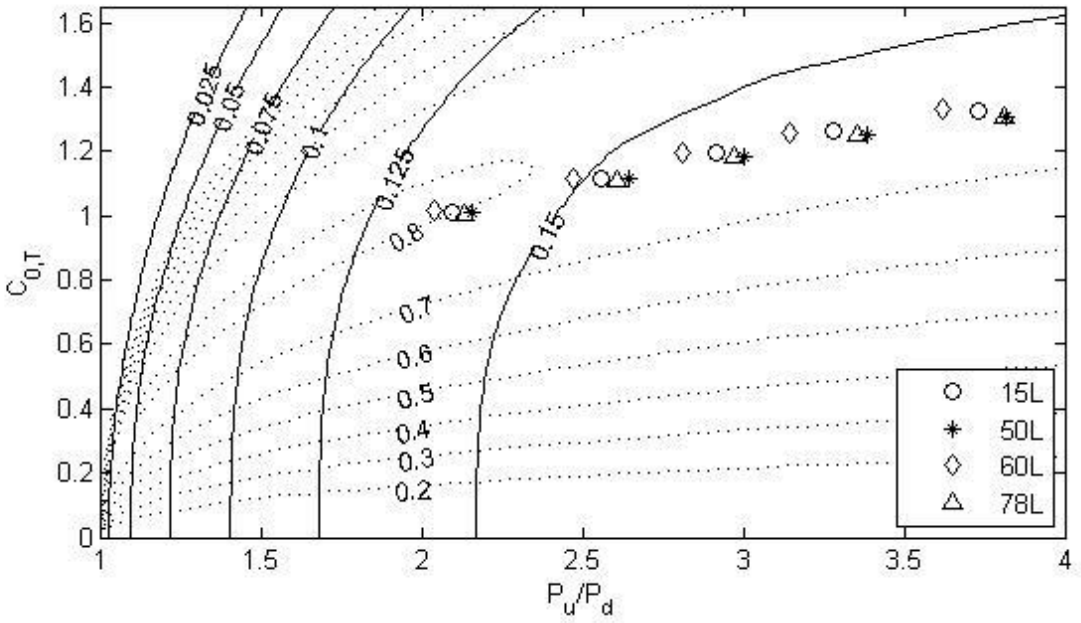

Figure 5-11: Turbine operation during simulation overlaid on normalized turbine map. Clusters of points from left to right correspond to 20%, 40%, 60%, 80%, and 100% engine load.

The results illustrate the non-dimensional maps can be utilized to model the turbocharger compressor and turbine across a range of engine models. Using the methods illustrated in this paper the work flow and effort required to model engine dynamics in control studies where turbocharging plays an important role can be reduced by eliminating the need to fit compressor and turbine data for each engine individually, but rather match the "generic" family maps to the engines through the selection of wheel diameters. In this way, a single map can be utilized across a range of studies involving different engines.

5.4 Conclusions

Due to the complexity of representing turbocharger behavior, the impact of turbocharging is often neglected in system simulations [18]. The method introduced in this paper allows a map produced for one specific turbocharger to be normalized into a "generic" map which represents a family of turbochargers with similar rotor and housing geometry, i.e. that have similar pitch-

chord ratios, s/l, and aspect ratios, h/l, within the family. The "generic" map can then be scaled to match an engine using methods similar to those utilized by turbocharger designers to scale performance data for customized turbocharger sizes. This eliminates the need for data specific to each turbocharger and reduces the time and effort required to model a range of engine sizes. As a result, simulations can include the impact for turbocharging to support more accurate system simulations.

6 Summary

The state-based mean-value turbocharged diesel and lean-burn natural gas engine models developed in this work enable the inclusion of advanced control functions and limitations during simulation of dynamic loading scenarios. Internal engine states such as manifold temperature and pressure or turbocharger rotor speed, as well as measurements such as air mass flow rate are available in the models as additional input for the controller. The capability of operation across a range of speed extends the utility of the engine models beyond microgrid to variable speed applications such as drilling and stimulation of oil and gas wells.

Although state-based models rely heavily on engine-specific empirical relationships, most of the data required by the state-based models presented in Chapter 2 and Chapter 3 can be found on public data sheets published by the equipment manufacturer. Generally, information about the turbocharger model and/or performance is not provided on these forms; however, modeling the turbocharger using a non-dimensional approach as discussed in Chapter 5 allows similar turbochargers to be modeled from a single set of performance data, reducing the effort required to implement models of several different engine sizes.

Models for driveline components utilized in hydraulic fracturing pumps were also developed in Chapter 4. The driveline model was used to simulate direct replacement of a diesel engine with a similar power lean burn natural gas engine. By modeling the full driveline, the dynamics during hydraulic fracturing operations can be investigated including the effects on the engine resulting from the operation of the torque converter and transmission in such an unconventional manner.

6.1 Conclusions

In Chapter 2 a state based diesel model was implemented and compared with a simplified model often used in microgrid studies and transient experimental data. The conclusions drawn are:

- The simplified engine model used in microgrid simulation does not capture the engine response seen in experimental data at all load levels, or when control limits are encountered.
- The state-based diesel model allows these limits to be considered and improves the response when compared to the experimental data.
- Simulations of transient events such as unplanned islanding or black starting a microgrid should not use the simplified model, but rather use state-based models in order to consider control limits which may limit the engine torque production.

In Chapter 3 a state-based model of a lean-burn natural gas engine was developed. The model exploits many of the components developed to model the diesel engine. Although the model was not validated against transient data, the expected behavior is captured.

In Chapter 4 models were developed to simulate the driveline dynamics of a hydraulic fracturing pump operating with a lean burn natural gas engine. The results showed:

- Although it is possible for the gas engine to recover after a shift under certain conditions, it is likely that the engine will not recover during operating pressures typical in well stimulation.
- Direct substitution of a diesel engine with a natural gas engine of similar power is not a viable solution in this application due to the poor capability of gas engines under transient loads.

In Chapter 5 the effort required to implement turbocharger performance maps in simulation models was illustrated, and an approach was developed to use non-dimensional maps which model a family of geometrically similar devices in order to reduce the amount of data and the effort required to implement state-based engine models of different sizes. The chapter illustrated:

- The non-dimensional approach significantly reduces the amount of data required to implement a series of engine models of different size and power by representing a family of similar turbochargers from the performance maps for a single device.
- The methods presented allow the non-dimensional maps to be matched to a given engine design, reducing both the amount of device specific data and effort required to implement a series of models.

6.2 Contributions

Experimental data from transient loading of large stationary engines is difficult to find in literature. This work measures the experimental response of a 50 liter diesel engine under rapid addition of load using a dynamometer. The response of the engine to different ramp rates and at different initial loads is measured while a fixed engine speed is commanded by the controller. The experimental data shows cases where alternate control paths are engaged, which limit the torque production of the engine resulting in larger deviations from the commanded speed.

This work is one of the first to compare the response of a simplified diesel engine model to experimental data collected during a transient. The simplified engine model is frequently used in transient control studies to model engines of vary different power levels, but validation against transient experimental data is never presented except for a 3MW diesel backup generator in the

original article published over 30 years ago. In many studies since, the same time constants are used from the original study to represent very different engines, ranging from 10kW to 2MW. This work has demonstrated that the simplified model does not capture the response of modern engines due to advanced control logic intended to reduce emissions or prevent engine wear.

A state-based diesel engine model is developed with the intention of replacing the simplified model. The stated-based model allows engine control logic which considers internal engine parameter to be included. A governor model is implemented which considers rich air-fuel ratio limits and maximum fueling limits, and is shown to improve agreement with experimental data when compared to the simplified model.

Many state-based models exist for applications in engine design, control development, and hardware-in-the-loop control validation. These models generally require very detailed knowledge of the engine and combustion process. Additionally, many simplified models exist for fuel economy prediction and modeling of steady applications. The state-based model developed in this dissertation serves a gap in engine models. It requires fewer physical parameters than the advanced models used in engine design, yet is capable of capturing dynamics in transient applications. Additionally, the framework for a state-based natural gas engine model is also developed in this dissertation.

A novel approach to modeling turbocharger performance in state-based engine models is developed in this work. The methods allow a family of compressors and turbines to be modeled from the data for a single device. The approach uses dimensional analysis techniques and a set of methods used in turbocharger design to develop tools for engine simulation and modeling.

6.3 Future Work

For microgrid applications, a stationary generator consisting of the engine, electric machine, and exciter should be modeled and validated using electric measurements during transient loading. Since acquiring the data required to model and validate a specific engine or generator can be challenging, developing a suite of validated parameter sets for several specific engines could be valuable in order to permit models to be implemented quickly for new simulations. Additionally, developing scaling relationships for each physical parameter should be performed to develop a "generic" set of parameters which can be scaled based on the desired engine power.

The transient response of the natural gas engine model should be validated against experimental data, and the controller gains should be tuned. The gas model, however, is used "as is" in a case study presented in Chapter 4 to model transients encountered during stimulation of oil and gas wells. The diesel engine model is used as a baseline for comparison. Although the controller gains are not accurately tuned in the study, the results illustrate the limitations of lean-burn natural gas engines in transient applications due to the tight coupling of the fuel and air system. The case study should be re-run with a tuned and validated natural gas model. Conceptual methods to improve the transient response of the lean-burn natural gas engine can be evaluated using the state-based model. Several methods are suggested at the end of Chapter 4.

7 References

[1] Office of Electricity Delivery and Energy Reliability Smart Grid R&D Program, "DOE Microgrid Workshop Report," U.S. Department of Energy, San Diego, California, 2011.

[2] S. B. Van Broekhoven, N. Judson, S. V. Nguyen and W. D. Ross, "Mircogrid Study: Energy Security for DoD Installations," Massachusetts Institute of Technology, Lincoln Laboratory, Lexington, Massachusetts, 2012.

[3] T. Abdallah, R. Ducey, R. S. Balog, C. A. Feickert, W. Weaver, A. Akhil and D. Menicucci, "Control Dynamincs of Adaptive and Scalable Power and Energy Systems for Military Micro Grids," US Army Corps of Engineers, Engineer Research Development Center, Washington, DC, 2006.

[4] T. Green and M. Prodanovic, "Control of inverter-based micro-grids," *Electric Power Systems Research,* vol. 77, pp. 1204-1213, 2007.

[5] R. Sebastian and J. Quesada, "Distributed control system for frequency control in a isolated wind system," *Renewable Energy,* vol. 31, no. 3, March 2006.

[6] R. Sebastian, "Modelling and Simulation of a High Penetration Wind Diesel System with Battery Energy Storage," *Electrical Power and Energy Systems,* vol. 33, no. 3, 2011.

[7] I. Serban, C. Ion, C. Marinescu and M. Georgescu, "Frequency Control and Unbalances Compensation in Autonomous Micro-Grids Supplied by RES," in *Electric Machines & Drives Conference,* 2007.

[8] S. Chowdhury, S. P. Chowdhury and P. Crossley, Microgrids and Active Distribution Networks, London: The Institution of Engineering and Technology, 2009.

[9] S. Rehman, I. M. El-Amin, F. Ahmed, S. Saahid, A. M. Al-Shehri, J. M. Bakhashwain and A. Shash, "Feasibility study of hybrid retrofits to an isolated off-grid diesel power plant," *Renewable and Sustainable Energy Reviews* , vol. 11, no. 4, pp. 635-653, 2007.

[10] P. Wall, F. Gonzalez-Longatt and V. Terzija, "Estimation of Generator Inertia Available During a Disturbance," San Diego, CA, 2012.

[11] B. M. M. Bomani, M. Elbuluk, H. Fain and M. D. Kankam, "The GreenLab Research Facility: A Micro-Grid Integrating Production, Consumption and Storage of Clean Energy," National Aeronautics and Space Administration, Cleveland, Ohio, 2012.

[12] P. Tielens and D. Van Hertem, "Grid Inertia and Frequency Control in Power Systems with High Penetration of Renewables," Delft, 2012.

[13] F. Katiraei, M. Iravani and P. Lehn, "Micro-Grid Autonomous Operation During and Subsequent to Islanding Process," *IEEE Transactions on Power Delivery,* vol. 20, no. 1, 2005.

[14] T. Del Carpio-Huayllas, D. Ramos and R. Vasquez-Arnez, "Microgrid Transition to Islanded Modes: Conceptual Background and Simulation Procedures Aimed at Assessing its Dynamics Performance," in *Transmission and Distribution Conference and Exposition,* Orlando, Fl, 2012.

[15] J. Dilliott, "UCSD Power System," 19 February 2013. [Online]. Available: http://www.districtenergy.org/assets/pdfs/2013CampConference/MicroGrids/Microgrids-and-Reliability/DILLIOTTJOHNUCSDMicrogridViridtyosisoft.pdf. [Accessed 25 October 2013].

[16] W. Liu, S. Gu and D. Qui, "Techno-economic assessment for off-grid hybrid generation systems and the aplication prospects in China," [Online]. Available: http://www.worldenergy.org/wecgeis/publications/.

[17] H. Ibrahim, R. Younes, T. Basbous, A. Ilinca and M. Dimitrova, "Optimization of Diesel Engine Performance for a Hybrid Wind-Diesel System with Compressed Air Energy Storage," *Energy,* vol. 36, no. 5, 2011.

[18] K. E. Yeager and J. R. Willis, "Modeling of Emergency Diesel Generators in an 800 Megawatt Nuclear Power Plant," *IEEE Transactions on Energy Conversion,* vol. 8, no. 3, pp. 433-441, 1993.

[19] L. N. Hannett, F. P. de Mello, G. H. Tylinski and W. H. Becker, "Validation of Nuclear Plant Auxilary Power Supply by Test," *IEEE Transactions on Power Apparatus and Systems,* Vols. PAS-101, no. 9, pp. 3068-3074, 1982.

[20] National Renewable Energy Laboratory, "Private Report for Marine Corps Air Station Miramar Microgrid".

[21] National Renewable Energy Laboratory, "NREL Furthers U.S. Marine Corps Air Station Miramar's Move Toward Net Zero Energy," February 2011. [Online]. Available:

http://www.nrel.gov/docs/fy11osti/48937.pdf. [Accessed 25 October 2013].

[22] D. G. Hill, J. Johnson, J. W. Bell, H. S. Giberson, N. Mayer, R. P. Hessler and W. Matthews, "Natural Gas As A Fuel In Drilling Operations - Analysis, Testing and Implementation," in *SPE/IADC Drilling Conference and Exhibition,* Amsterdam, 2011.

[23] E. Henin, "Dual Fuel progress in reliability and performance for the Oil and Gas Market," in *SPE/IADC Drilling Conference,* Amsterdam, 2013.

[24] R. C. Lee and D. B. Wimmer, "Exhaust emission abatement by fuel variations to produce lean combustion.," *SAE Paper 680769,* 1968.

[25] F. H. Sutley, "Installation and Tesing of a Cummins QSK19 Lean Burn Natural Gas Engine," 2013.

[26] H. . M. Cho and B.-Q. He, "Spark ignition natural gas engines – A review," *Energy Conversion and Management,* vol. 48, pp. 608-618, 2007.

[27] J. Hacohen, M. Belmont, R. Thurley, J. Thomas, E. Morris and D. Buckingham, "Experimental and theoretical analysis of flame development and misfire phenomena in S.I. engines," *SAE Paper 920415,* 1992.

[28] L. Guzzella and C. H. Onder, Introduction to Modeling and Control of Internal Combustion Engine Systems, Springer, 2004.

[29] J.-B. Millet, F. Maroteaux and F. Aubertin, "Air System and Diesel Combustion Modeling for Hardware in the Loop Applications," *Journal of Engineering for Gas Turbines and*

Power, vol. 134, 2012.

[30] M. Kao and J. J. Moskwa, "Turbocharged Diesel Engine Modeling for Nonlinear Engine Control and State Estimation," vol. 117, no. 1, 1995.

[31] D. N. Malkhede, B. Seth and H. C. Dhariwal, "Mean Value Model and Control of a Marine Turbocharged Diesel Engine," in *Powertrain & Fluid Systems Conference and Exhibition*, San Antonio, Tx, 2005.

[32] P. Moraal and I. Kolmanovsky, "Turbocharger Modeling for Automotive Control Applications," in *SAE Technical Paper 1999-01-0908*, 1999.

[33] S. N. Danov and A. K. Gupta, "Modeling the Performance Characterstics of DIesel Engine Based Combined-Cycle Power Plants - Part I: Mathematical Model," *Journal of Engineering for Gas Turbines and Power,* vol. 126, no. 1, pp. 28-34, 2004.

[34] S. M. Yahya, Turbines Compressors and Fans, New Delhi: Tata McGraw-Hill Publishing Company Limited, 1983.

[35] C. R. Ferguson and A. T. Kirkpatrick, Internal Combustion Engines: Applied Thermosciences, 2nd ed., New York: John Wiley & Sons, Inc., 2001.

[36] The MathWorks, "Simscape Documentation Center - Variable Area Pneumatic Orifice," 2013. [Online]. Available: http://www.mathworks.com/help/physmod/simscape/ref/variableareapneumaticorifice.html .

[37] The MathWorks, "SimDriveline Documentation Center - Torque Converter," 2015. [Online]. Available: http://www.mathworks.com/help/physmod/sdl/ref/torqueconverter.html.

[38] The MathWorks, "Simscape Documentation Center - Variable Hydraulic Chamber," 2015. [Online]. Available: http://www.mathworks.com/help/physmod/simscape/ref/variablehydraulicchamber.html.

[39] The MathWorks, "SimHydraulics Documentation Center - Check Valve," 2015. [Online]. Available: http://www.mathworks.com/help/physmod/hydro/ref/checkvalve.html.

[40] The MathWorks, "SimDriveline Documentation Center - Simple Gear," 2015. [Online]. Available: http://www.mathworks.com/help/physmod/sdl/ref/simplegear.html.

[41] T. Katrasnik, V. Medica and F. Trenc, "Analysis of the dynamic response improvement of a turbocharged diesel engine driven alternating current generating set," *Energy Conversion and Management,* vol. 46, 2005.

[42] Gamma Technologies, *GT-SUITE Flow Theory Manual, Version 7.3,* 2012.

[43] J. Heywood, Internal Combustion Engine Fundamentals, McGraw-Hill, 1988.

[44] J. Jensen, A. Kristensen, S. Sorenson, N. Houbak and E. Hendricks, "Mean Value Modeling of a Small Turbocharged Diesel Engine," in *SAE Technical Paper 910070,* 1991.

[45] M. Muller, E. Hendricks and S. Sorenson, "Mean Value Modelling of Turbocharged Spark Ignition Engines," in *SAE Technical Paper, 980784,* 1998.

[46] S. A. Nelson, Z. S. Filipi and D. N. Assanis, "The use of neural nets for matching compressors with diesel engines," *American Society of Mechanical Engineers, Internal Combustion Engine Division (Publication) ICE,* vol. 26, pp. 35-42, 1996.

[47] The MathWorks, "Simscape Documentation Center - Constant Volume Pneumatic Chamber," 2013. [Online]. Available: http://www.mathworks.com/help/physmod/simscape/ref/constantvolumepneumaticchamber.html.

[48] C. D. Rakopoulos, E. G. Giakoumis and D. T. Hountalas, "Experimental and Simulation Analysis of the Transient Operation of a Turbocharged Multi-Cylinder IDI Diesel Engine," *Inernational Journal of Energy Research,* vol. 22, no. 4, pp. 317-331, 1998.

[49] A. Sakhrieh, E. Abu-Nada, I. Al-Hinti, A. Al-Ghandoor and B. Akash, "Computational thermodynamic analysis of compression ignition engine," *International Communications in Heat and Mass Transfer,* vol. 37, 2012.

[50] A. G. Stefanopoulou, I. Kolmanovsky and J. S. Freudenberg, "Control of Variable Geometry Turbocharged Diesel Engines for Reduced Emissions," *IEEE TRANSACTIONS ON CONTROL SYSTEMS TECHNOLOGY,* vol. 8, no. 4, 2000.

[51] L. del Re, F. Allgower, L. Glielmo, C. Guardiola and I. Kolmanovsky, Automotive Model Predictive Control: Models, Methods and Applications, Springer, 2010.

[52] W. W. Pulkrabek, Engineering Fundamentals of the Internal Combustion Engine, 2nd ed., Pearson Prentice-Hall, 2004.

[53] C. Bell, D. Zimmerle, T. Bradley, D. Olsen and P. Young, "Scalable Turbocharger Performance Maps for Dynamic State-Based Engine Models," *International Journal of Engine Research*, 2015 (In-review).

APPENDIX I – Custom Simscape Component Models

8 Custom Component Model Library

The models described in this paper were implemented in MATLAB Simscape. Simscape is a software toolbox developed for the solution of systems of differential and algebraic equations representing physical systems. The software includes many pre-existing component models which are useful in developing models of dynamic systems across multiple physical domains. A custom component library was developed including several component models for use in the diesel and natural gas engine models. A brief discussion of the equation set associated with each of these components is presented in this appendix.

8.1 Infinite Chamber

The infinite chamber component models an infinite volume from which or to which mass can flow without changing the temperature or pressure of the gas in the volume. The component is modeled after the Simscape constant volume pneumatic chamber [47], where the differential equations used to determine the mass and energy of the volume have been replaced with constant temperature and pressure defined through parameters to fix the state of the gas at the pneumatic port A. The component is used to model the ambient environment from which mass is drawn into the intake system and to which mass is transferred from the exhaust.

8.2 Compressor

The turbocharger compressor is modeled using the non-dimensional approach discussed in Part IV. The component has two pneumatic nodes corresponding to the compressor inlet and outlet, and two rotational nodes corresponding to the turbocharger rotor and case. The compressor equations determine algebraic relations between the upstream and downstream states, and the turbocharger rotor.

A 1-D lookup table of pressure ratio at compressor surge $PR_{surge} = \left(\frac{P_{out}}{P_{in}}\right)_{surge}$ as a function of rotor tip Mach number is implemented in the component model as illustrated in Table 8-1. That is, $PR_{surge} = f(c_0)$ where c_0 is the Mach number based on rotor tip speed calculated as $c_0 = \frac{ND}{\sqrt{\gamma RT_{in}}}$ where N is the angular velocity of the rotor, D is the diameter of the compressor blade, γ is the specific heat ratio of the gas, R is the gas constant, and T_{in} is the absolute temperature of the gas at the compressor inlet.

Table 8-1: Compressor model – 1D lookup table of compressor surge vs rotor tip Mach number

	c_0						
	0	0.0473	0.0946	…	2.6956	2.7429	2.7902
PR_{surge}	1	1.0007	1.0029	…	3.8143	8.9181	4.022

A 2D lookup table of mass flow coefficient, θ, as a function of a normalized pressure ratio and Mach number based on rotor tip speed is implemented as shown in Table 8-2. That is,

$$\theta = \frac{\dot{m}}{N_{TC}} \frac{\sqrt{RT_{in}}}{D^2 P_{in}} = f(P_{idx}\ ,\ c_0) \tag{66}$$

where $\dot{m}$ is the mass flow rate through the compressor and P_{in} is the pressure at the compressor inlet. The number of turbochargers in parallel, N_{TC}, has been introduced to split the total intake flow into multiple parallel streams, each flowing through a unique turbocharger. P_{idx} is the pressure ratio normalized by the pressure ratio at compressor surge.

$$P_{idx} = \frac{PR - 1}{PR_{surge}(c_0) - 1} \tag{67}$$

Table 8-2: Compressor model – 2D lookup table of compressor mass flow coefficient

		c_0						
		0	0.0473	0.0946	…	2.6956	2.7429	2.7902
P_{idx}	0	0	0.0057	0.0114		0.2498	0.2500	0.2503
	0.0169	0	0.0057	0.0114		0.2492	0.2495	0.2498
	0.0339	0	0.0056	0.0113		0.2486	0.2489	0.2493
	…							
	0.9661	0	0.0020	0.0041		0.1941	0.1969	0.1998
	0.09831	0	0.0019	0.0037		0.1883	0.1921	0.1959
	1.0000	0	0	0		0	0	0

Figure 8-1 shows an example compressor mass flow map. The bottom subplot shows the map in a format similar to compressor data provided by manufacturers after fitting, extrapolating to low rotor speeds and low pressure ratios, and converting to non-dimensional parameters as discussed in Part IV. The figure shows lines of constant rotor tip Mach number c_0, with mass flow coefficient θ on the x-axis and pressure ratio on the y-axis. The height of the surface (colorbar) represents rotor tip Mach number. The upper edge of the surface is the surge line. The top subplot shows the data translated to a format suitable for simulation with rectilinear axes. It shows contours of mass flow coefficient θ against the rotor tip Mach number c_0 on the x-axis and normalized pressure ratio P_{idx} on the y-axis.

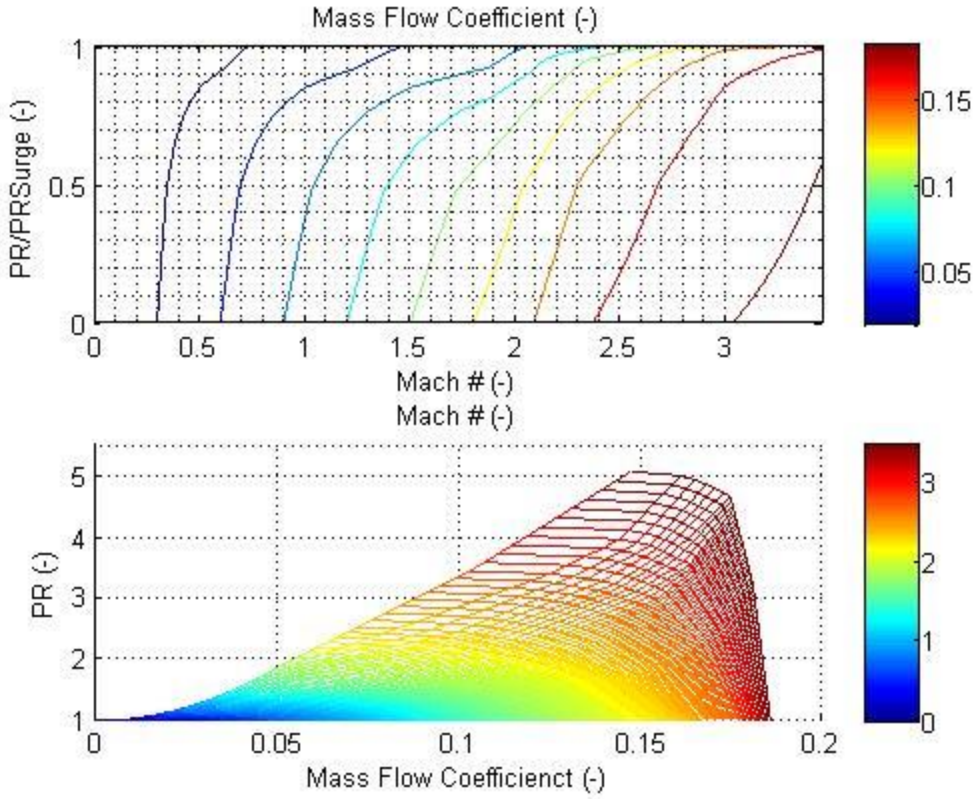

Figure 8-1: Compressor mass flow coefficient map presented in two formats: first as a contour plot formatted on rectilinear axis for implementation in simulation, and second similar to manufacturer data presentation where data has been fit and interpolation and extrapolation used to include additional rotor speeds and pressure ratios not shown in original data.

The compressor efficiency is also implemented as a 2D lookup table as a function of a normalized pressure ratio and Mach number based on rotor tip speed, $\eta = f(P_{idx}\ ,\ c_0)$ as illustrated in Table 8-3. Figure 8-2 shows an example compressor efficiency map. The bottom subplot shows the map in a format similar to compressor data provided by manufacturers after fitting, extrapolating to low rotor speeds and low pressure ratios, and converting to non-dimensional parameters as discussed in Part IV. The figure shows lines of constant rotor tip Mach number c_0, with mass flow coefficient θ on the x-axis and pressure ratio on the y-axis. The height of the surface (colorbar) represents efficiency. Again, the upper edge of the surface is the surge line. The top subplot shows the data translated to a format suitable for simulation using

rectilinear axes. It shows contours of efficiency η against the rotor tip Mach number c_0 on the x-axis and normalized pressure ratio P_{idx} on the y-axis.

Table 8-3: Compressor model – 2D lookup table of compressor efficiency

		c_0						
		0	0.0473	0.0946	…	2.6956	2.7429	2.7902
P_{idx}	0	0.2000	0.2000	0.2000		0.2000	0.2000	0.2000
	0.0169	0.2000	0.2004	0.2007		0.2101	0.2100	0.2099
	0.0339	0.2000	0.2007	0.2014		0.2202	0.2200	0.2199
	…							
	0.9661	0.2000	0.4500	0.4633		0.7208	0.7149	0.7089
	0.09831	0.2000	0.4384	0.4514		0.7220	0.7169	0.7118
	1.0000	0.2000	0.4269	0.4395		0.06974	0.6987	0.7000

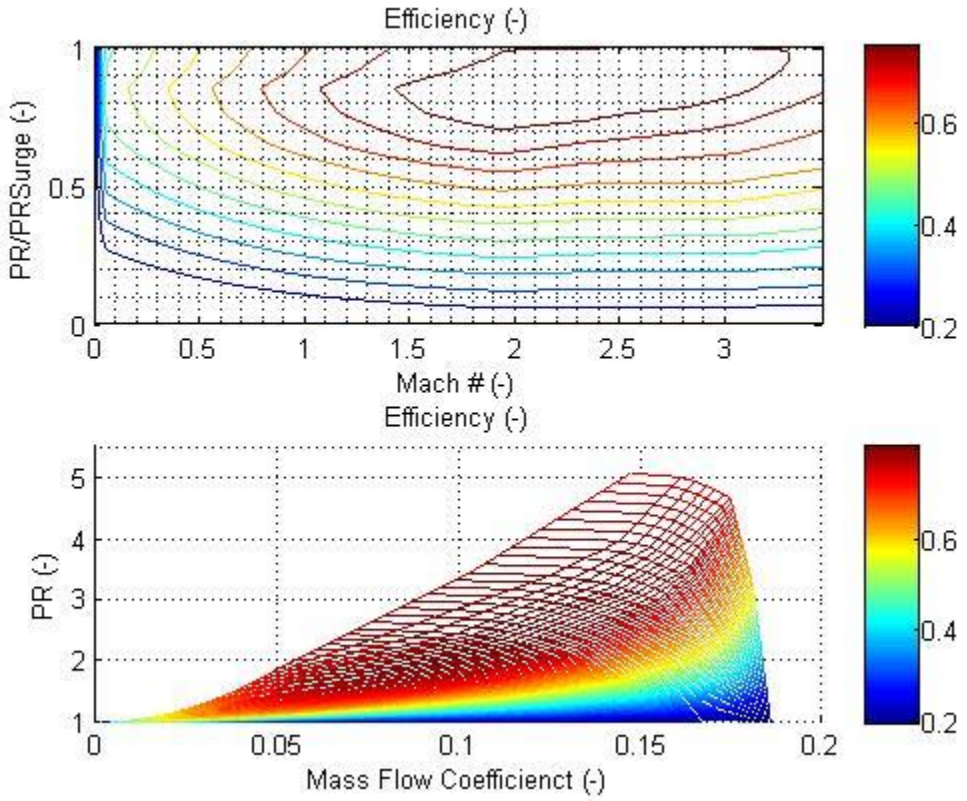

Figure 8-2: Compressor efficiency map presented in two formats: first as a contour plot formatted on rectilinear axis for implementation in simulation, and second similar to manufacturer data presentation where data has been fit and interpolation and extrapolation used to include additional rotor speeds and pressure ratios not shown in original data.

The torque required to compress the gas, τ_C, is calculated from isentropic relations as

$$\tau_C = \frac{\dot{m} C_p T_{in}}{\mathrm{N_{TC}} \eta \omega} \left(\left(\frac{P_{out}}{P_{in}} \right)^{\frac{\gamma-1}{\gamma}} - 1 \right) \tag{68}$$

where C_p is the specific heat at constant pressure of the gas, ω is the rotor speed, γ is the specific heat ratio of the gas, and subscripts $_{\text{in}}$ and $_{\text{out}}$ indicate the inlet and outlet of the compressor respectively.

The energy entering the compressor with the air, Q_{in}, is calculated as $Q_{in} = \dot{m} C_p T_{in}$. The temperature of gas leaving the compressor is calculated from isentropic relations as

$$T_{C,out} = T_u \left\{ 1 + \frac{1}{\eta_C} \left\{ \left(\frac{P_{out}}{P_{in}} \right)^{\frac{\gamma-1}{\gamma}} - 1 \right\} \right\} \tag{69}$$

The energy leaving the compressor is then calculated as $Q_{out} = \dot{m} C_p T_{C,out}$.

8.3 Turbine

The turbocharger turbine is modeled using the non-dimensional approach discussed in Part IV. The component has two pneumatic nodes corresponding to the turbine inlet and outlet, and two rotational nodes corresponding to the turbocharger rotor and case. The turbine equations determine algebraic relations between the upstream and downstream states, and the turbocharger rotor.

The mass flow coefficient is implemented as a 2D lookup table as illustrated in Table 8-4, as a function of the expansion ratio, $\left(\frac{P_{\text{in}}}{P_{\text{out}}}\right)$, and a Mach number based on rotor tip speed.

$$\theta = \frac{\dot{m}}{N_{TC}} \frac{\sqrt{R T_{in}}}{D^2 P_{in}} = f\left(\frac{P_{in}}{P_{out}}, \qquad c_0 \right) \tag{70}$$

Table 8-4: Turbine model – 2D lookup table of turbine mass flow coefficient

		c_0						
		0.0000	0.0302	0.0603	…	1.7190	1.7492	1.7794
$\frac{P_{in}}{P_{out}}$	1	0.0000	0.0000	0.0000		0.0000	0.0000	0.0000
	1.0066	0.0112	0.0113	0.0112		0.0010	0.0010	0.0010
	1.0187	0.0188	0.0189	0.0189		0.0017	0.0017	0.0017
	…							
	3.8488	0.0978	0.0979	0.0979		0.0919	0.0915	0.0911
	3.9240	0.0979	0.0979	0.0979		0.0920	0.0917	0.0913
	4.0000	0.0980	0.0980	0.0980		0.0922	0.0918	0.0915

Figure 8-3 shows an example turbine mass flow map. The bottom subplot shows the map in a format similar to turbine data provided by manufacturers after fitting, extrapolating to low rotor speeds and pressure ratios, and converting to non-dimensional parameters as discussed in Part IV. The figure shows lines of constant rotor tip Mach number c_0, with mass flow coefficient θ on the y-axis and pressure ratio on the x-axis. The height of the surface (colorbar) represents rotor speed. The top subplot shows the data translated to a format suitable for simulation using rectilinear axis. It shows contours of mass flow coefficient against the rotor tip Mach number c_0 on the y-axis and pressure ratio on the x-axis.

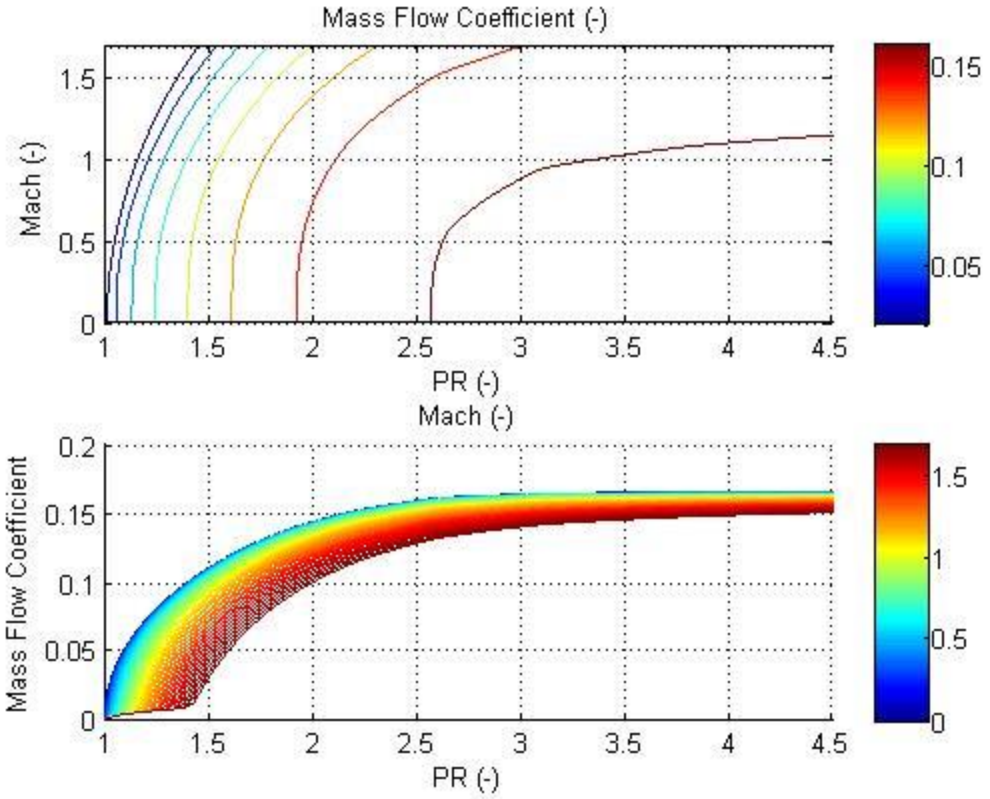

Figure 8-3: Turbine mass flow coefficient map presented in two formats: first as a contour plot formatted on rectilinear axis for implementation in simulation, and second similar to manufacturer data presentation where data has been fit and interpolation and extrapolation used to include additional rotor speeds and pressure ratios not shown in original data.

The turbine efficiency is also implemented as a 2D lookup table as illustrated in Table 8-5, as a function of the expansion ratio, $\left(\frac{P_{\text{in}}}{P_{\text{out}}}\right)$, and a Mach number based on rotor tip speed, $\eta = f\left(\frac{P_{\text{in}}}{P_{\text{out}}},\ c_0\right)$. Figure 8-4 shows an example turbine efficiency map. The bottom subplot shows the map in a format similar to data provided by manufacturers, that is lines of constant rotor tip Mach number c_0, with mass flow coefficient θ on the y-axis and pressure ratio on the x-axis. The height of the surface (colorbar) represents efficiency. The data has been fit and interpolation and extrapolated has been performed to include rotor speeds and pressure ratios not shown in the original data. The top subplot shows the data translated to a format suitable for simulation. It

shows contours of efficiency η against the rotor tip Mach number c_0 on the y-axis and pressure ratio on the x-axis.

Table 8-5: Turbine model – 2D lookup table of turbine efficiency

		c_0						
		0.0000	0.0302	0.0603	…	1.7190	1.7492	1.7794
$\frac{P_{in}}{P_{out}}$	1	0.1000	0.1000	0.1000		0.1000	0.1000	0.1000
	1.0066	0.1000	0.2252	0.4260		0.1000	0.1000	0.1000
	1.0187	0.1000	0.1374	0.2667		0.1000	0.1000	0.1000
	…							
	3.8488	0.1000	0.1000	0.1000		0.7640	0.7701	0.7757
	3.9240	0.1000	0.1000	0.1000		0.7620	0.7683	0.7740
	4.0000	0.1000	0.1000	0.1000		0.7600	0.7665	0.7724

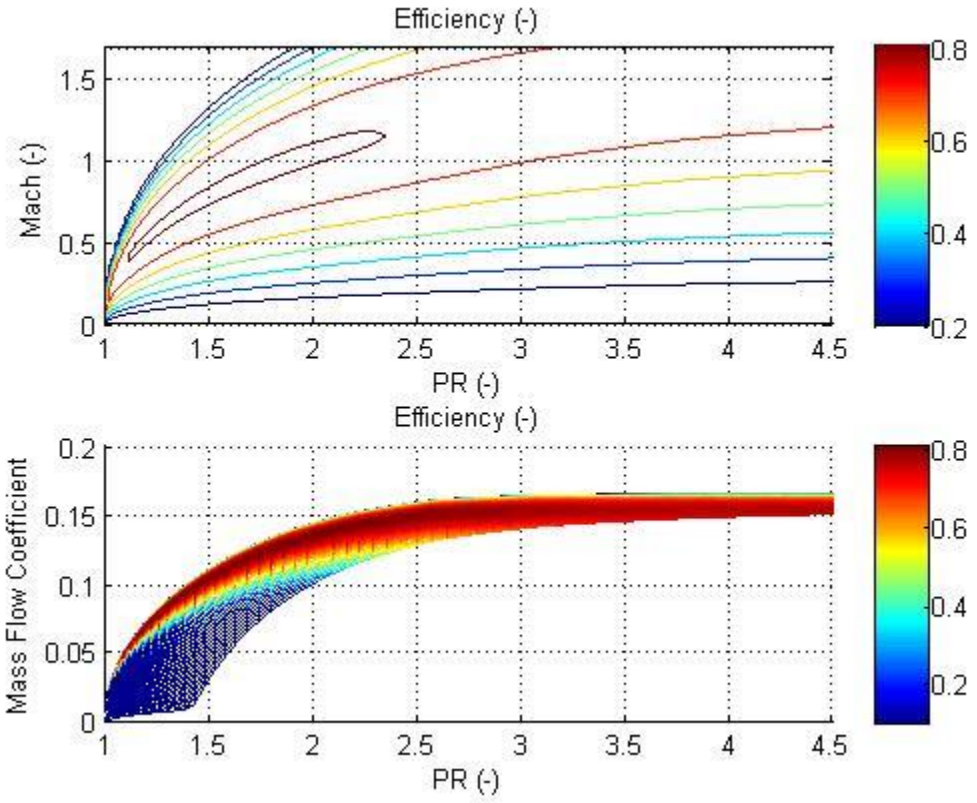

Figure 8-4: Turbine efficiency map presented in two formats: first as a contour plot formatted on rectilinear axis for implementation in simulation, and second similar to manufacturer data presentation where data has been fit and interpolation and extrapolation used to include additional rotor speeds and pressure ratios not shown in original data.

The torque produced by the turbine is calculated from isentropic relations as

$$\tau_T = \frac{\eta \dot{m} C_p T_{in}}{N_{TC} \omega} \left(1 - \left(\frac{P_{out}}{P_{in}} \right)^{\frac{\gamma - 1}{\gamma}} \right) \quad (71)$$

The energy entering the turbine with the exhaust gas is calculated as $Q_{in} = \dot{m} C_p T_{in}$. The temperature of the gas leaving the turbine is calculated using isentropic relations as

$$T_{T,out} = T_u \left(1 + \eta_T \left(\left(\frac{P_{out}}{P_{in}} \right)^{\frac{\gamma - 1}{\gamma}} - 1 \right) \right) \quad (72)$$

The heat leaving the compressor can then be calculated as $Q_{out} = \dot{m} C_p T_{T,out}$

8.4 Combustor Intake

The combustor has been separated into an intake and exhaust component. The two components only pass physical signals, which separates the intake and exhaust pneumatic systems allowing different gas properties to be specified for each. The combustor intake component is used to model the engine pumping and heat accompanying the air flow into the engine cylinders. The volumetric efficiency is a function of engine speed and load and is implemented as a 2D lookup table based on empirical data formatted as shown in Table 8-6. Engine load provided as a physical signal from the combustor exhaust component.

Table 8-6: Combustor intake model – 2D lookup table of volumetric efficiency

		ω (rpm)						
		600	700	800	…	1900	2000	2100
Load	0.1	0.9466	0.9375	0.9486		0.8437	0.8260	0.8099
	0.2	0.9582	0.9495	0.9453		0.8388	0.8229	0.8097
	0.3	0.575	0.9529	0.9422		0.8344	0.8196	0.8083
	…							
	0.8	0.9460	0.9548	0.9508		0.8234	0.8091	0.7986
	0.9	0.9478	0.9590	0.9487		0.8229	0.8083	0.7966
	1	0.9522	0.9734	0.9508		0.8230	0.8088	0.7956

Figure 8-5 shows an example contour plot of volumetric efficiency. The bottom subplot shows contours of volumetric efficiency (height off the x-y plane indicated by the colorbar) plotted against engine speed on the x-axis and engine torque on the y-axis. The maximum torque curve is shown on the figure as a function of speed. Normalizing the torque data by the maximum torque curve results in the contour plot shown in the upper figure formatted on rectilinear axis suitable for implementation as a lookup table during simulation where the y-axis represents percent load.

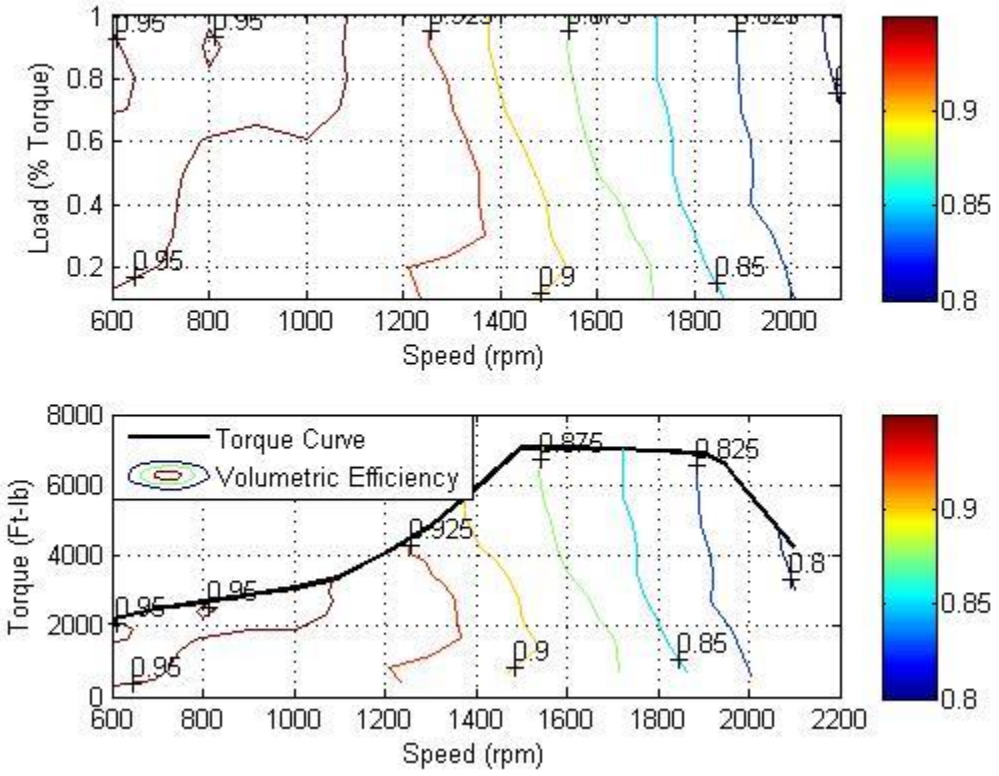

Figure 8-5: Combustor intake – Volumetric efficiency map presented in two formats: first as a contour plot formatted on rectilinear axis for implementation in simulation, and second similar to manufacturer data presentation in engine operational range below maximum torque curve.

The mass flow rate entering the combustor is computed using the speed density equation as

$$\dot{m} = \frac{\eta_v \rho N_c V_d \omega}{n} \quad (73)$$

where $\eta_v$is the volumetric efficiency, ρ is the density of the gas in the intake manifold calculated using the ideal gas equation, N_c is the number of cylinders, V_d is the displacement of a cylinder, ω is the engine rotational speed, and n is the number of revolutions per cycle (2) for a four stroke engine. The energy entering the combustor accompanying the intake air is computed using the mass flow rate, specific heat and upstream temperature as $\dot{Q}_{in} = \dot{m} C_p T_{in}$.

8.5 Combustor Exhaust

The combustor exhaust component determines the mass flow rate and temperature of exhaust gas, as well as the torque applied to the crankshaft. The mass flow rate leaving the combustor through the pneumatic port on the exhaust component is calculated from conservation of intake air and fuel mass flow rates as

$$\dot{m}_{exh} = \dot{m}_{in} + \dot{m}_{fuel} \quad (74)$$

where $\dot{m}_{in}$ is the intake mass flow rate (provided as a physical signal from the intake component) and $\dot{m}_{fuel}$ is the fuel mass flow rate (provided as a physical signal from the governor subsystem).

The rate of energy leaving the combustor with the exhaust, $\dot{Q}_{exh}$, is calculated as

$$\dot{Q}_{exh} = \dot{m}_{exh} C_{p,exh} T_{exh} \quad (75)$$

where $C_{p,exh}$ is the specific heat of the exhaust gas and T_{exh} is the exhaust temperature implemented as a 2D lookup table based on engine speed and load formatted as shown in Table 8-7.

Table 8-7: Combustor exhaust model – 2D lookup table of exhaust temperature

		ω (rpm)						
		600	700	800	…	1900	2000	2100
Load	0.1	388	396	404		599	601	607
	0.2	412	449	446		670	656	638
	0.3	462	487	487		707	698	679
	…							
	0.8	624	675	701		790	765	749
	0.9	649	711	737		819	781	757
	1	675	772	774		850	809	768

Figure 8-6 shows an example contour plot of exhaust temperature. The bottom subplot shows contours of exhaust temperature (height off the x-y plane indicated by the colorbar) plotted against engine speed on the x-axis and engine torque on the y-axis. The maximum torque curve is shown on the figure as a function of speed. Normalizing the torque data by the maximum torque curve results in the contour plot shown in the upper subplot formatted on rectilinear axes suitable for implementation as a lookup table during simulation where the y-axis represents percent load.

The indicated shaft torque, τ_i, is calculated using the thermal efficiency, η_T, as

$$\tau_i = \eta_T \dot{m}_{fuel} E_{LHV} \quad (1)$$

where E_{LHV} is the lower heating value of the fuel, and η_T is implemented as a 2D lookup table based on engine speed and load formatted as shown in Table 8-8. Figure 8-7 shows an example thermal efficiency map similar to the exhaust temperature map in Figure 8-6.

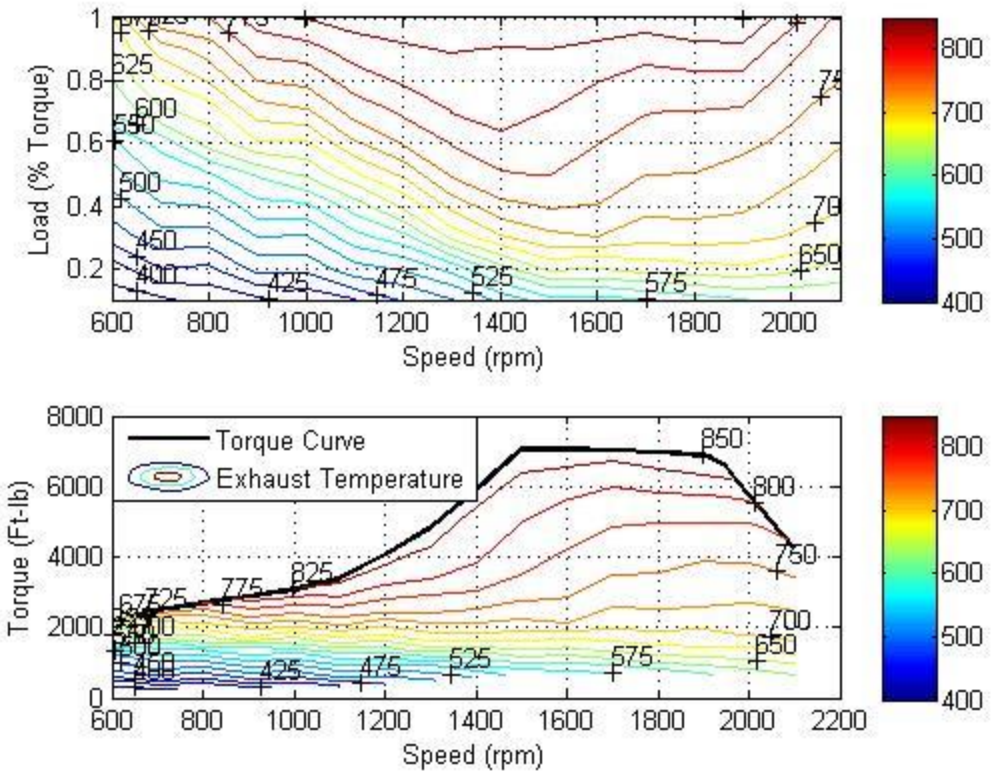

Figure 8-6: Exhaust temperature map presented in two formats: first as a contour plot formatted on rectilinear axis for implementation in simulation, and second similar to manufacturer data presentation in engine operational range below maximum torque curve.

Table 8-8: Combustor exhaust model – 2D lookup table of thermal efficiency

		ω (rpm)						
		600	700	800	…	1900	2000	2100
Load	0.1	0.262	0.268	0.275		0.308	0.288	0.255
	0.2	0.314	0.330	0.338		0.355	0.338	0.303
	0.3	0.354	0.362	0.367		0.373	0.355	0.329
	…							
	0.8	0.381	0.385	0.380		0.419	0.415	0.393
	0.9	0.378	0.383	0.376		0.419	0.421	0.399
	1	0.373	0.380	0.370		0.415	0.417	0.402

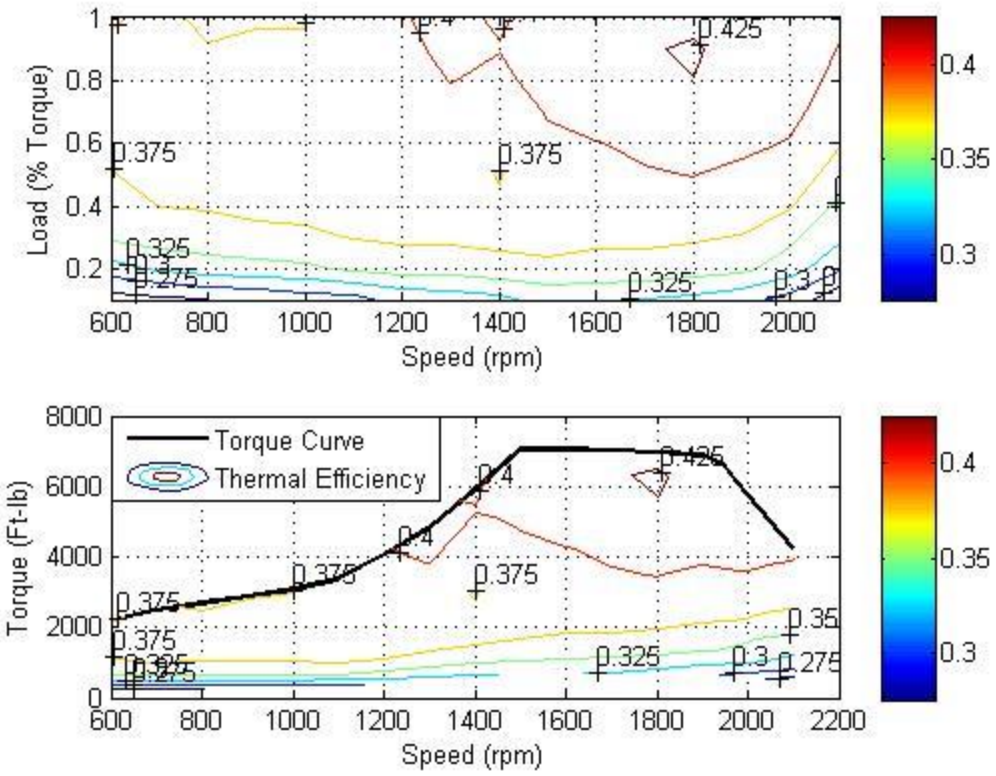

Figure 8-7: Thermal efficiency map presented in two formats: first as a contour plot formatted on rectilinear axis for implementation in simulation, and second similar to manufacturer data presentation in engine operational range below maximum torque curve.

Frictional losses internal to the engine are included in this component. Frictional torque is assumed to increase linearly with engine speed. Frictional power at rated speed and low idle are provided as parameters to establish the slope of the torque vs speed line. Linear interpolation and extrapolation are then used. This assumption follows figure 6-1, pg 136 of Ferguson & Kirkpatrick [35]. The net torque output on the rotational node of the combustor is calculated as the difference of the indicated torque and the friction torque.

$$\tau_{net} = \tau_i - \tau_f \tag{2}$$

Engine load is used as an index for the exhaust temperature and thermal efficiency lookup tables. The engine load is calculated as engine torque divided by maximum engine torque at the current speed.

$$load = \tau_{net}/\tau_{max} \tag{3}$$

The maximum torque curve is implemented as a 1D lookup table against engine speed as illustrated in Table 8-9.

Table 8-9: Combustor exhaust model – 1D lookup table of maximum torque vs engine speed

	ω (rpm)						
	600	700	800	…	1950	2000	2100
τ_{max} (ft-lb)	2225	2500	2700	…	6566	5798	4261

APPENDIX II – Simscape Subsystems and Engine Models

9 Model Subsystem Library

Several subsystems which are comprised of components from the Simscape foundation library and the custom components discussed in Appendix I are presented in this section. The turbocharged diesel and natural gas engine model, discussed in Part II and Part III respectively, are built from these subsystems.

9.1 Turbocharger Subsystem

The turbocharger subsystem illustrated in Figure 9-1 is composed of the compressor and turbine components described in Appendix I, as well as a mechanical rotational inertia and rotational reference from the Simscape foundation library. The compressor and turbine inlet and outlet are pneumatic nodes available to connect to the upstream and downstream volumes. The rotational inertia models the lumped inertia of the rotor assembly (compressor wheel, shaft and turbine wheel). The rotational references represent the turbocharger housing.

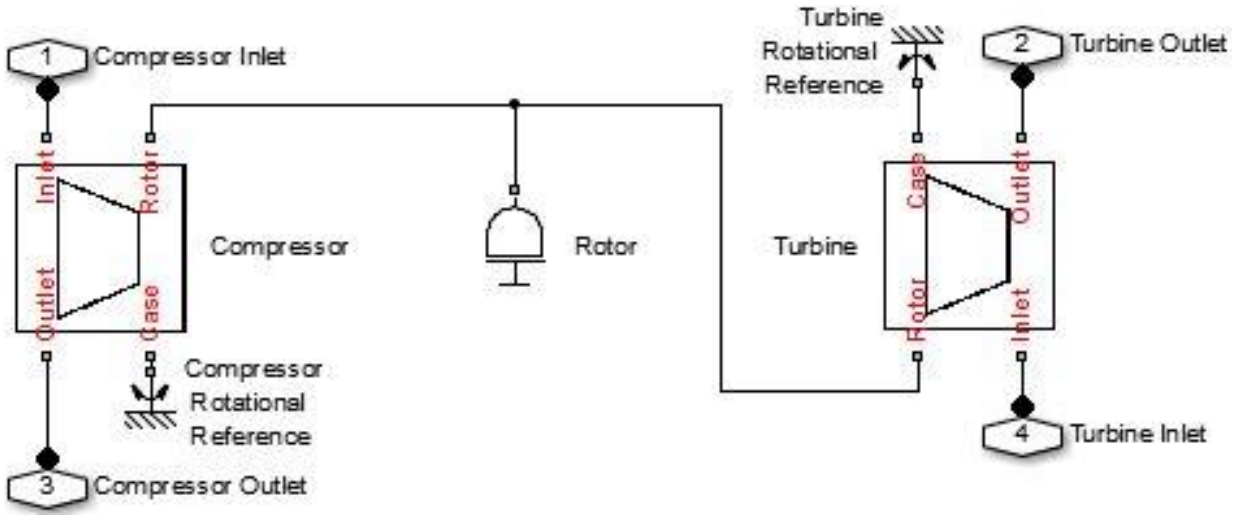

Figure 9-1: Simscape turbocharger subsystem

9.2 Adiabatic Chamber Subsystem

The adiabatic chamber subsystem illustrated in Figure 9-2 is used to represent the turbocharger interstage plenums and the exhaust manifold. It is also used to represent the intake manifold in the natural gas engine model. The subsystem is composed of a constant volume chamber with an adiabatic cup attached to the thermal node. Both components are from the Simscape foundation library. The inlet and outlet are connected to the pneumatic node of the adiabatic chamber.

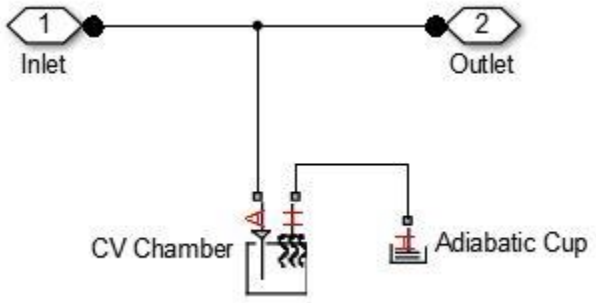

Figure 9-2: Simscape adiabatic chamber subsystem

9.3 Intercooler Subsystem

A constant volume pneumatic chamber with an ideal temperature source connected to the thermal node is used to model the intercooler as shown in Figure 9-3. The ideal temperature source is from the Simscape foundation library and transfers heat to maintain the temperature of the gas in the pneumatic chamber. Although the intercooler on a real engine does not maintain a constant temperature, the fluctuations seen in experimental data during transients were small resulting in < 2% change in density of air in the intake manifold.

For a more accurate model the effectiveness method used by [48] could be implemented. This approach would rely on additional engine-specific empirical data. The constant temperature approach was utilized for simplicity and to minimize the reliance on engine-specific data.

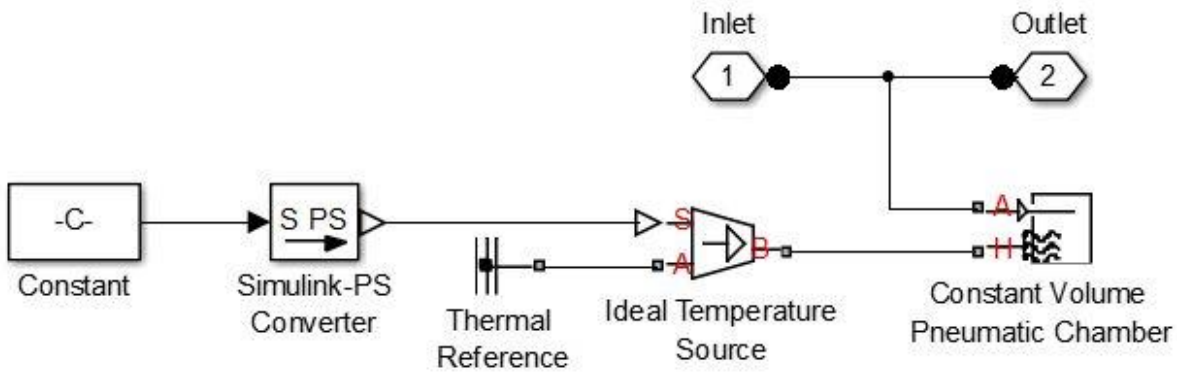

Figure 9-3: Simscape intercooler subsystem

9.4 Combustor Subsystem

The combustor subsystem consists of the intake and exhaust components connected by physical signals to separate the intake and exhaust pneumatic networks as shown in Figure 9-4. Simscape propagates gas properties through a pneumatic network as constants. By dividing the combustor into two halves the pneumatic network is divided which allows different gas properties to be specified for the intake and exhaust gases. The intake (1) and exhaust (2) connections in the figure are pneumatic nodes, and the shaft (3) is a rotational node. The air flow rate (4), engine load (5) and engine speed (6) are physical signal outputs to the governor model, which provides the fuel signal (7) to the combustor.

The intake component serves to model the volumetric pumping of the engine cylinders using the speed density equation as described in section 8.4 of Appendix I. The exhaust component determines the mass flow rate and temperature of gas leaving the combustor, as well as the torque produced on the crankshaft as described in section 8.5 of Appendix I.

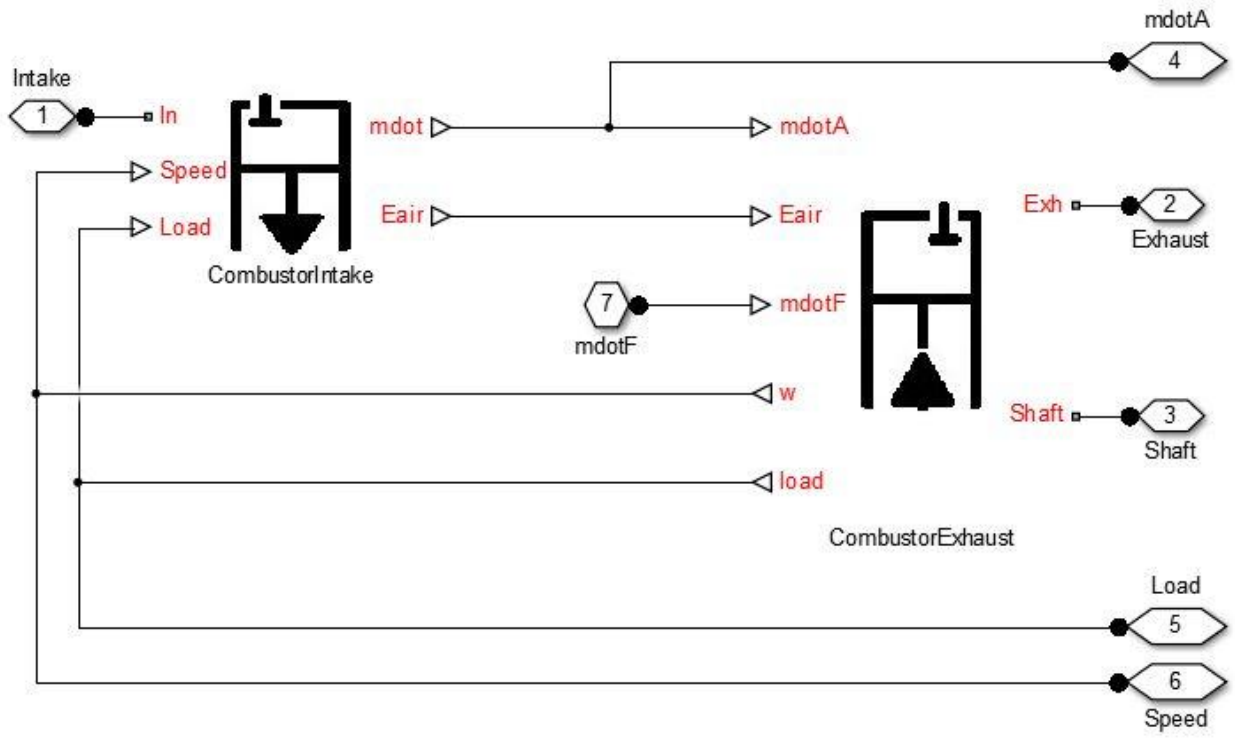

Figure 9-4: Simscape combustor subsystem

9.5 Diesel Governor

The diesel governor is based around the PID controller shown in Figure 9-5 with the clamping anti-windup method enabled, and variable saturation limits and gains provided as input signals. The governor model, Figure 9-6, provides a maximum fueling limit to the PID upper saturation limit. The maximum fueling limit is the minimum of (1) the fueling calculated to not exceed the rich limit, or (2) the fueling from the speed based maximum fueling table. Lookup tables determine the value of proportional and integral gains provided to the PID controller as a function of engine load. The difference between the engine speed and the commanded engine speed are provided as the input to the PID controller. The PID output is the fuel flow rate, which is converted to a physical signal before it is passed to the combustor subsystem.

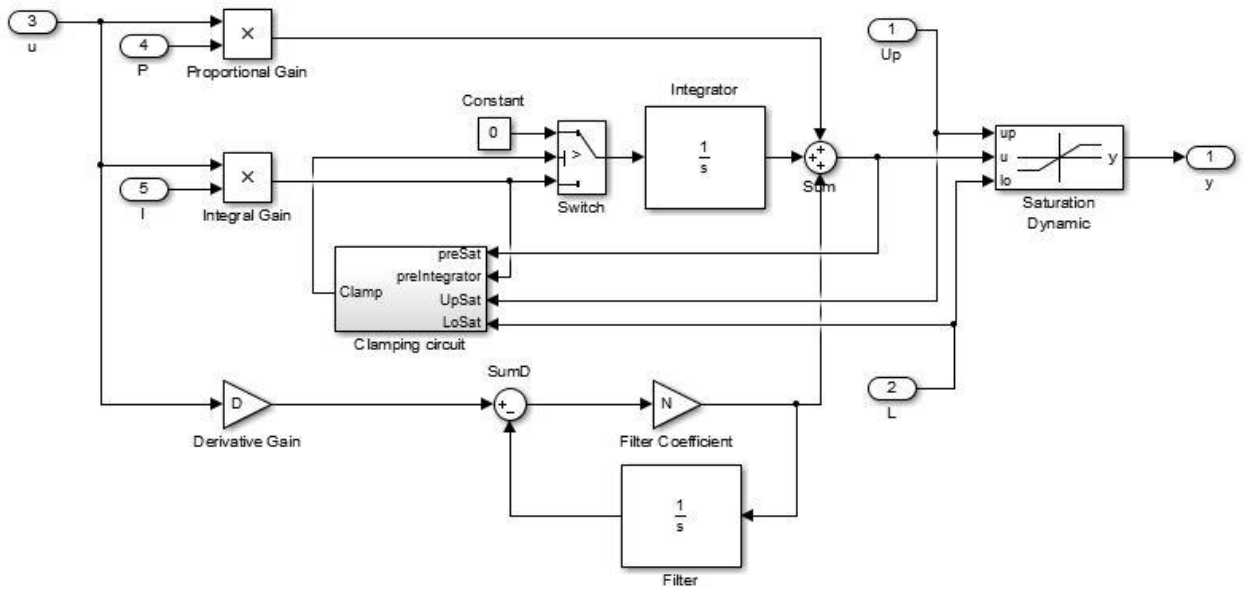

Figure 9-5: Simulink PID with clamping circuit enabled and including variable saturation limits, and variable proportional and integral gains provided as input signals

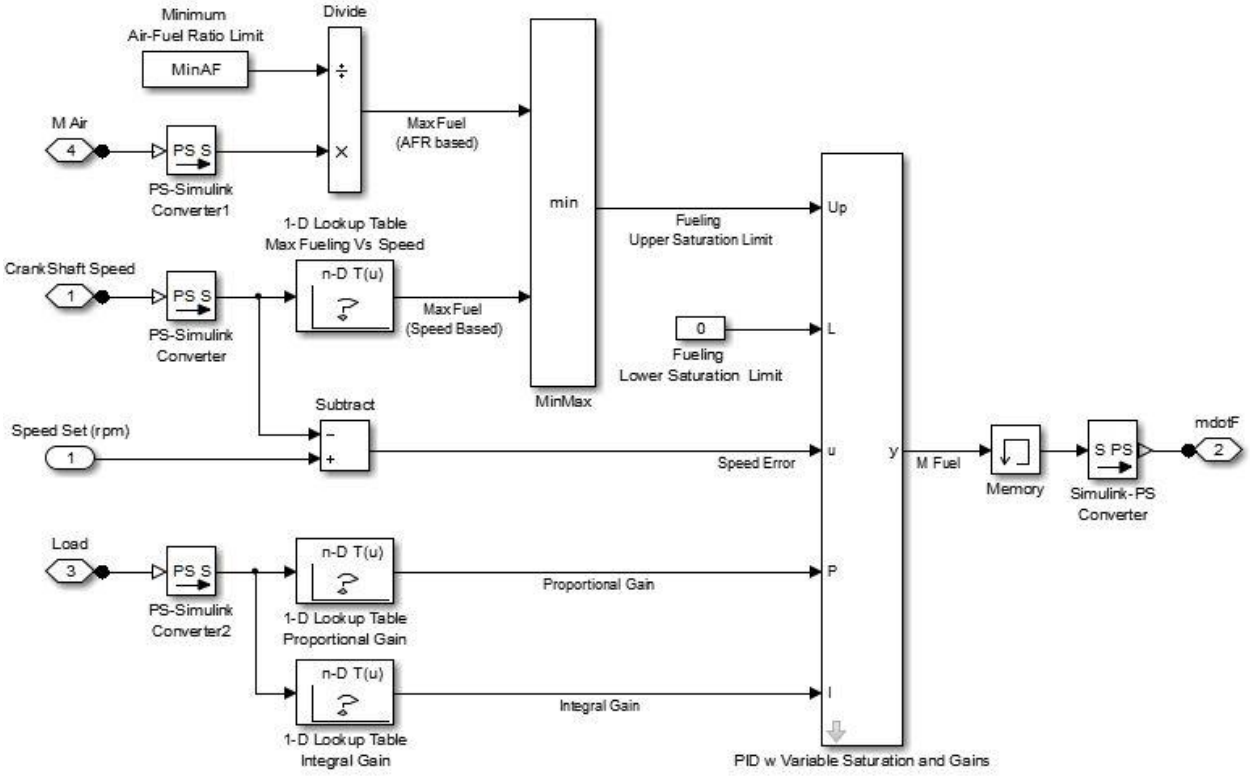

Figure 9-6: Simulink diesel governor subsystem

9.6 Throttle

The throttle model, shown in Figure 9-7, uses the variable area orifice from the Simscape pneumatic foundation library [36]. The area is selected from a lookup table as a function of throttle position. The throttle position is controlled by a PID controller with the output saturated between 0 (fully closed) and 1 (fully open) with the clamping anti windup method enabled. The throttle responds to the difference between the measured engine speed and the commanded engine speed.

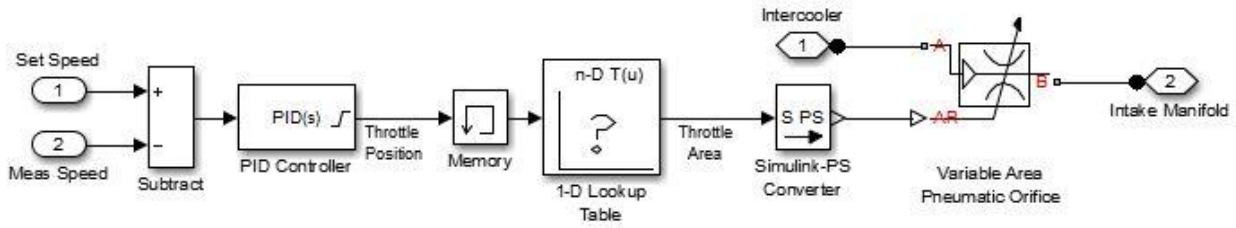

Figure 9-7: Simscape throttle subsystem

9.7 Natural Gas Fuel Valve

The fueling in the natural gas model is controlled to maintain a constant air-fuel ratio. The air flowrate is measured by the combustor subsystem and the signal is provided to the fuel valve subsystem shown in Figure 9-8, which calculates the fuel flow rate using the commanded air-fuel ratio. The output is saturated between zero and a maximum fueling limit.

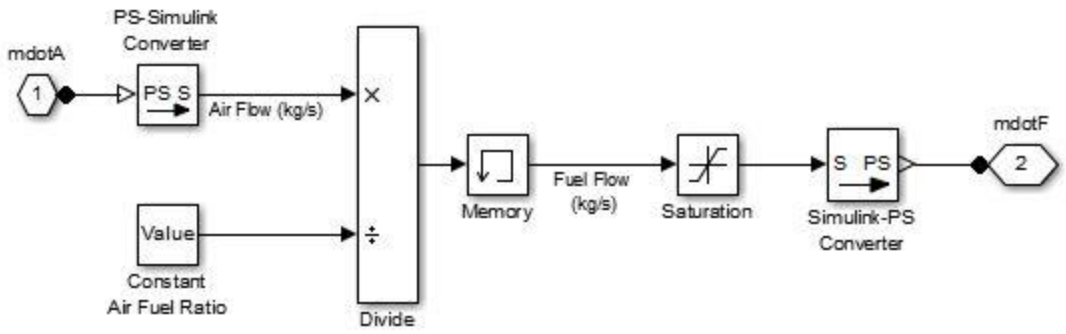

Figure 9-8: Simulink natural gas fuel valve subsystem

10 Assembled Engine Models

Several permutations of the diesel and natural gas models are presented in this chapter as described in Table 10-1. Each is assembled from the subsystems described in the preceding section.

Table 10-1: Engine model permutations implemented in Simscape

	Permutation	Schematic	Simscape Model
1	Diesel - Single stage turbocharging	Figure 10-1, page 134	Figure 10-2, page 134
2	Diesel - Two stage turbocharging	Figure 2-5, page 24	Figure 10-3, page 135
3	Natural Gas- Single stage turbocharging	Figure 3-1, page 38	Figure 10-4, page 136
4	Natural Gas- Two stage turbocharging	Figure 10-5, page 137	Figure 10-6, page 138

10.1 Permutation 1 – Diesel with Single Stage Turbocharger

The schematic for a diesel engine turbocharged with a single stage is illustrated in Figure 10-1. The model includes only two gas states: (1) the intake manifold, and (2) the exhaust manifold. There are two rotational states associated with the turbocharger rotor and the crankshaft. Figure 10-2 shows the model implemented in Simscape using the subsystems described in this appendix.

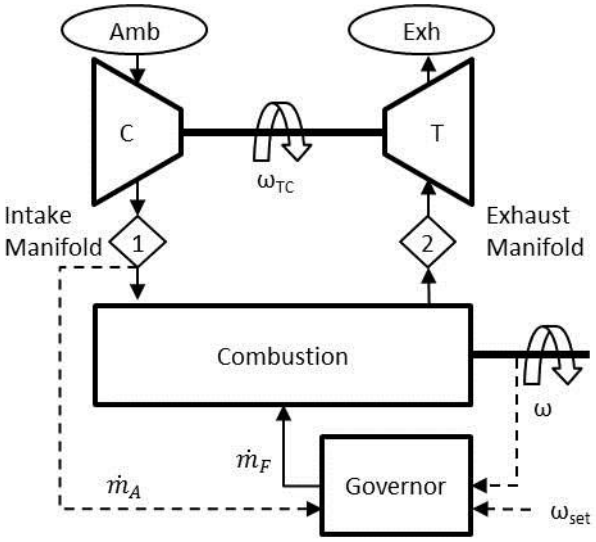

Figure 10-1: Diesel engine schematic with single stage turbocharger

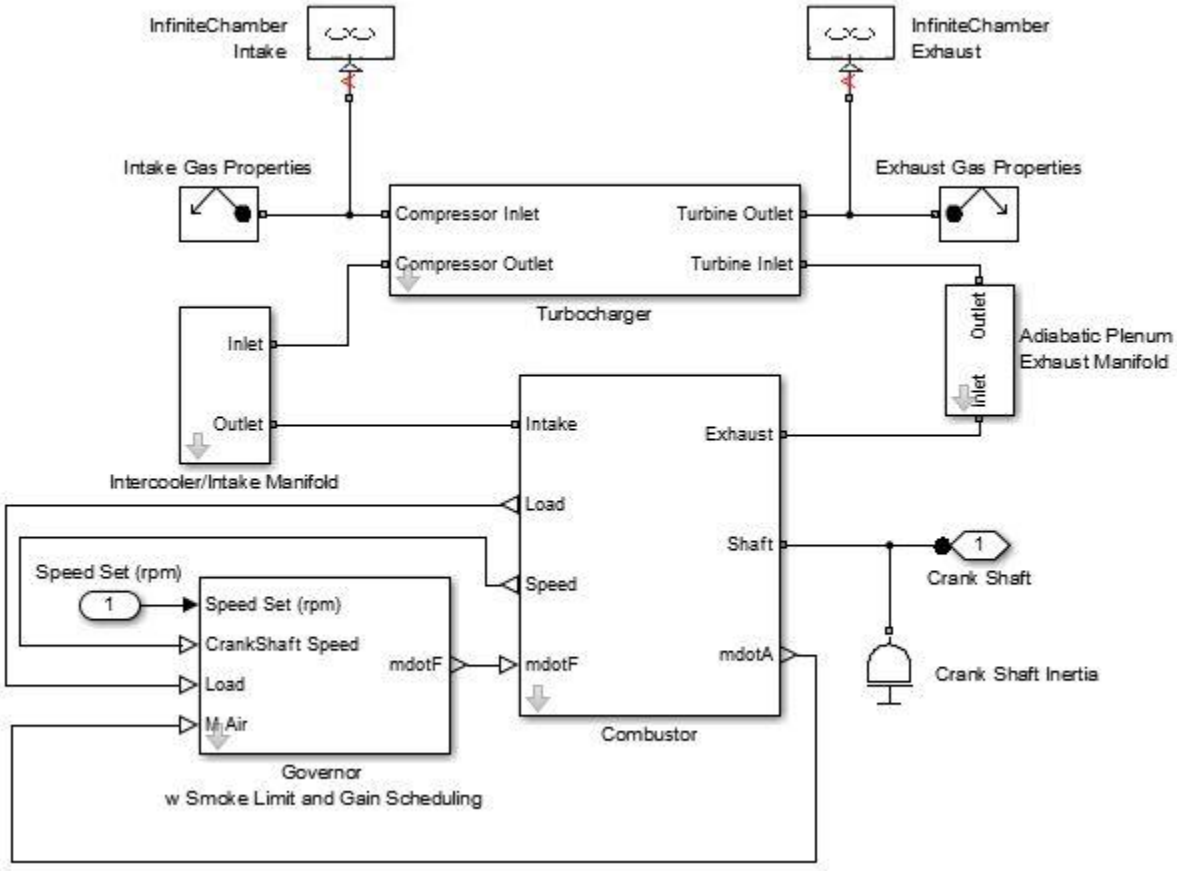

Figure 10-2: Simscape model of diesel engine with single stage turbocharger

10.2 Permutation 2 – Diesel with Two Stage Turbocharger

The schematic for a diesel engine turbocharged with a two stages in series is illustrated in Figure 2-5 in Part II. The model includes four gas states: (1) the compressor mid-stage plenum, (2) the intake manifold, (3) the exhaust manifold, and (4) the turbine mid-stage plenum. There are three rotational states associated with the low pressure turbocharger rotor, the high pressure turbocharger rotor, and the crankshaft. Figure 10-3 shows the model implemented in Simscape using the subsystems described in this appendix.

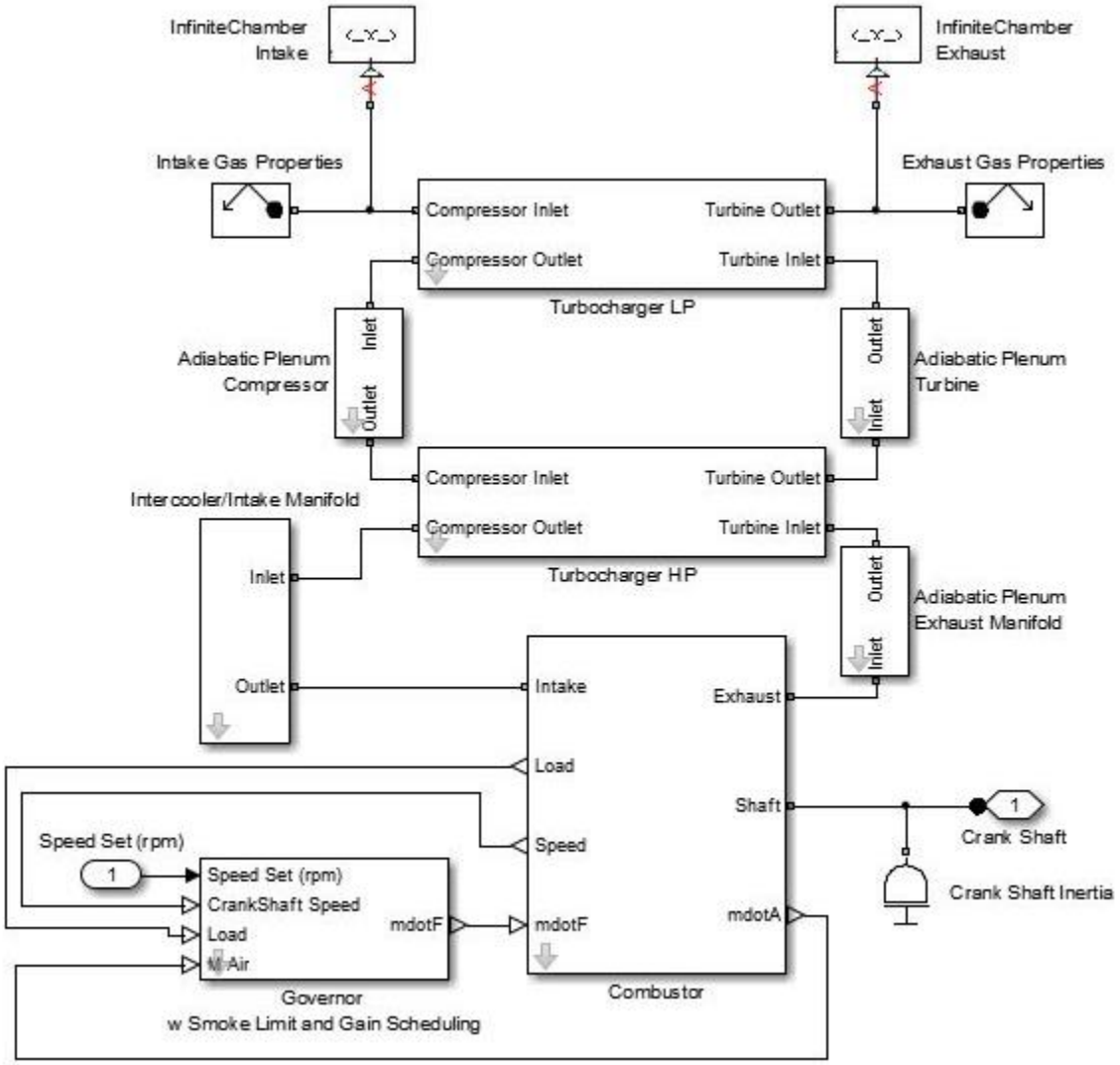

Figure 10-3: Simscape model of diesel engine with two stage turbocharger

10.3 Permutation 3 – Natural Gas with Single Stage Turbocharger

The schematic for a spark-ignited natural gas engine turbocharged with a single stage is illustrated in Figure 3-1 in Part III. The Simscape model is shown in Figure 10-4. The model includes three gas states: (1) the intercooler, (2) the intake manifold, and (3) the exhaust manifold. Two rotational states are associated with the turbocharger rotor and the crankshaft .

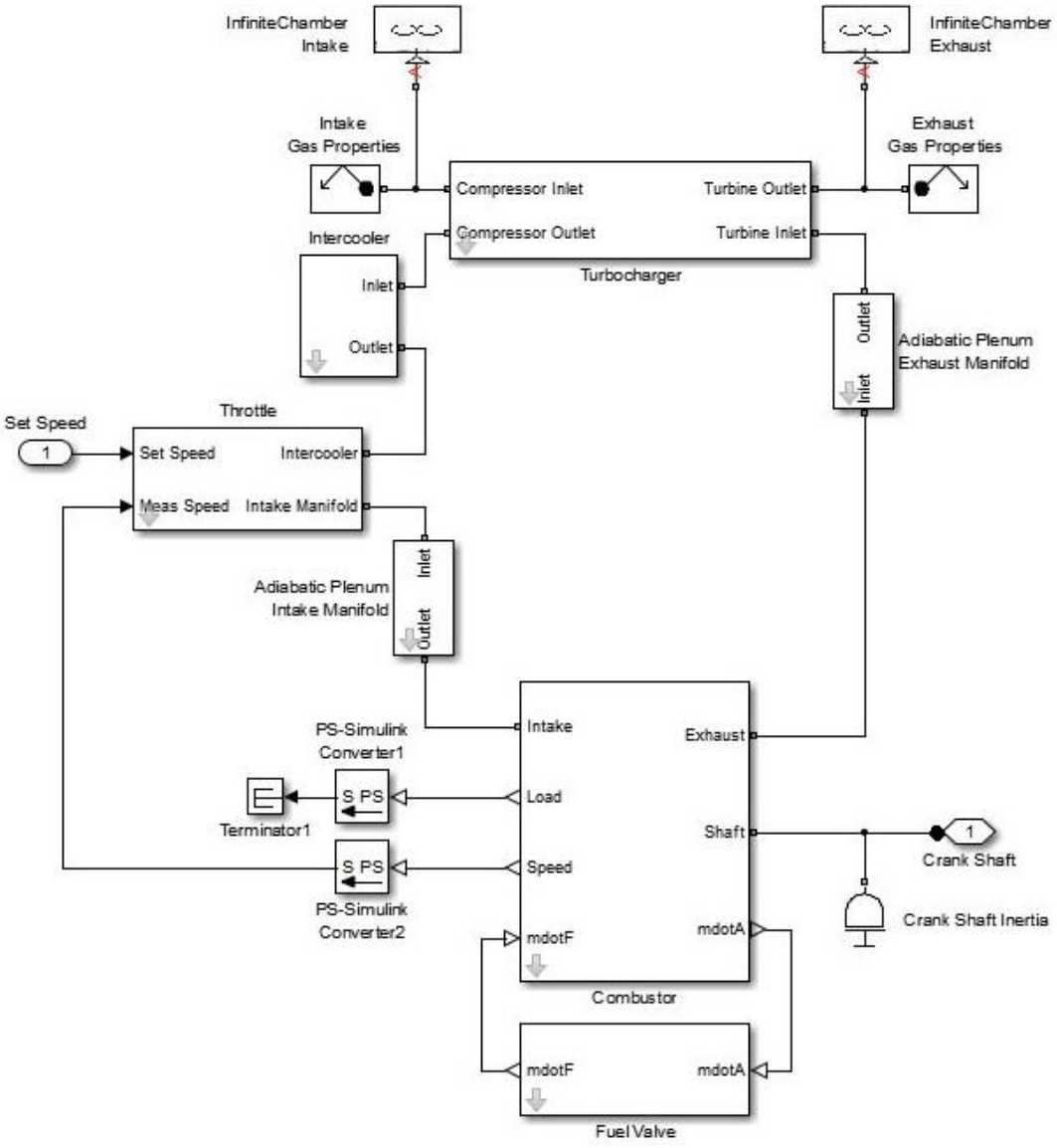

Figure 10-4: Simscape model of natural gas engine with single stage turbocharger

10.4 Permutation 4 – Natural Gas with Two Stage Turbocharger

The schematic for a spark-ignited natural gas engine turbocharged with a two stages in series is illustrated in Figure 10-5. The model includes five gas states: (1) the compressor mid-stage plenum, (2) the intercooler, (3) the intake manifold, (4) the exhaust manifold, and (5) the turbine mid-stage plenum. There are three rotational states associated with the low pressure turbocharger rotor, the high pressure turbocharger rotor, and the crankshaft. Figure 10-6 shows the model implemented in Simscape using the subsystems described in this appendix.

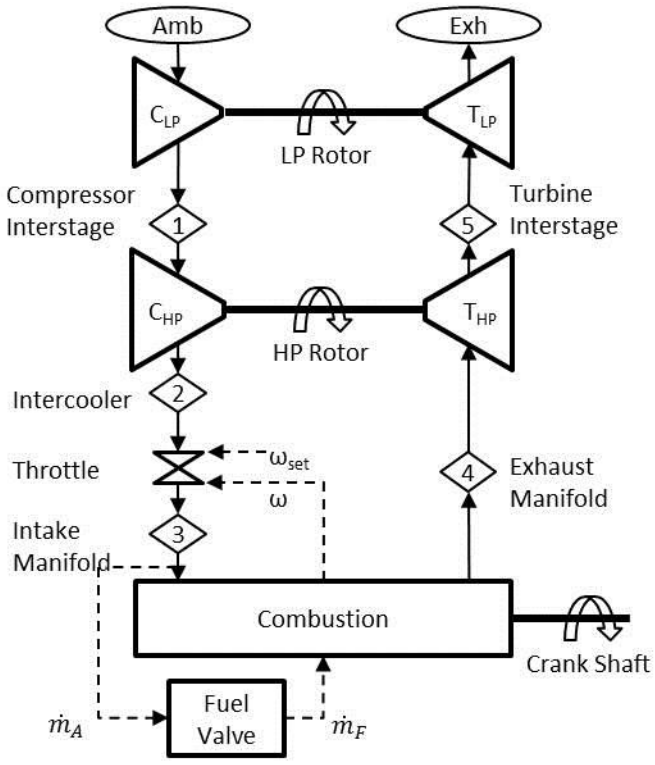

Figure 10-5: Natural gas engine schematic with two stage turbocharger

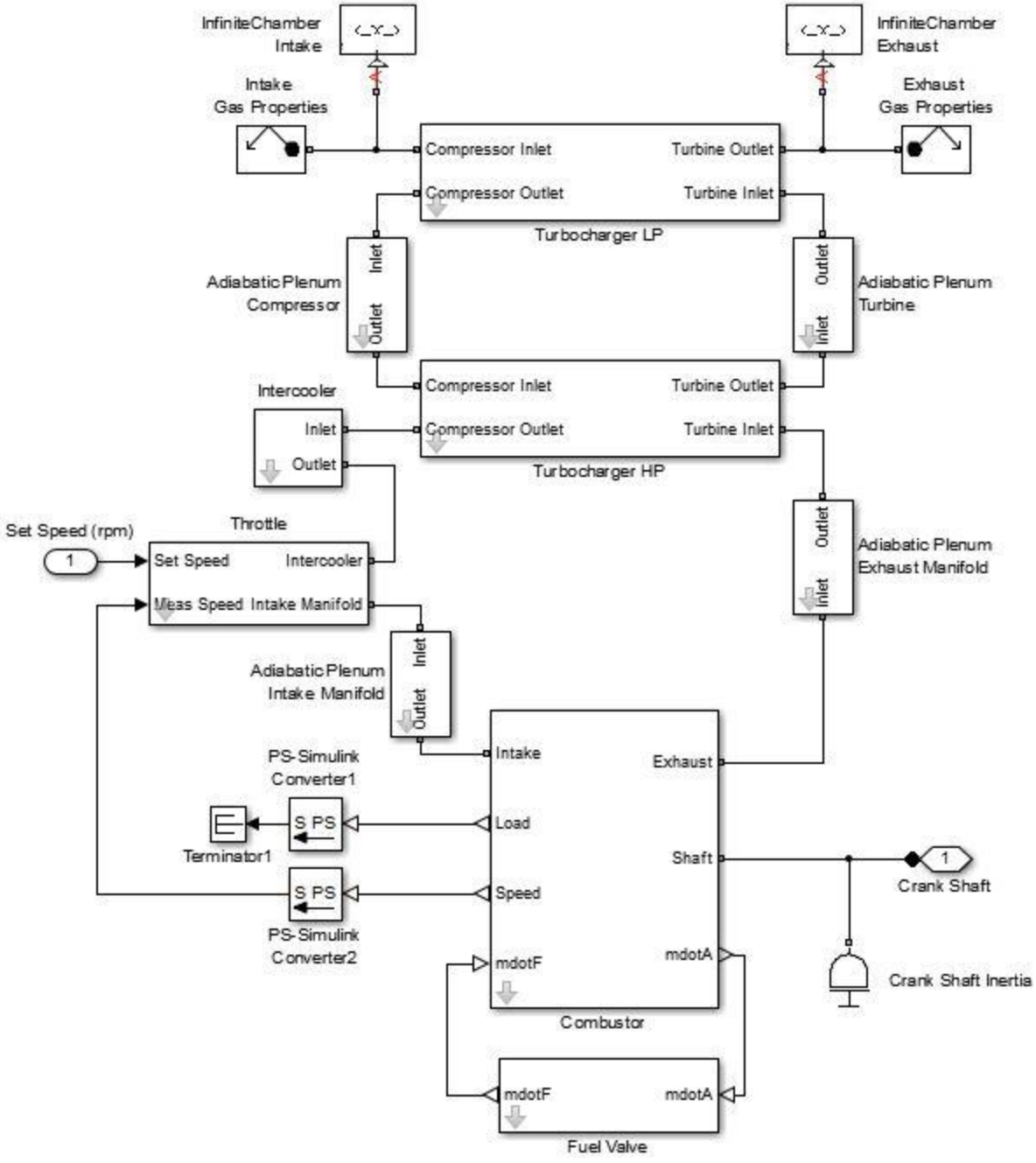

Figure 10-6: Simscape model of natural gas engine with two stage turbocharger